

Kondo-Majorana coupling in Double Quantum Dots.

by

Jesús David Cifuentes Pardo

Advisor: Luis Gregorio Dias da Silva

MASTER OF SCIENCE

in

Instituto de Física

(Condensed Matter Physics)

UNIVERSIDADE DE SÃO PAULO

(R. do Matão, 1371 - Butantã, São Paulo)

February 20, 2019

© Jesús David Cifuentes Pardo 2017

Chapter 1

Abstract

In the last decades the interest in the “search of Majorana fermions” in condensed matter systems [1] has increased due to their potential applications in quantum computing. As recently as 2012, experimental works reporting the detection of such quasiparticles [2, 3]. Later works [4, 5, 6, 7], including a recent paper published by the advisor of this dissertation and collaborators [8], set out to explore the interplay of such Majorana zero-modes with strongly interacting systems such as semiconductor quantum dots, which can be readily integrated in the device. This research project aims to expand this idea using the numerical renormalization group to study the model of a double quantum dot coupled to metallic leads and to a topological superconductor supporting edge Majorana zero modes (MZMs). This simple model allows the manipulation of the MZMs bringing possible applications to braiding procedures . In addition, we will study the interplay of Kondo correlations, exchange interactions and Majorana physics.

Chapter 2

Table of Contents

1 Abstract	2
2 Table of Contents	3
3 Motivation	5
3.1 Structure	7
4 Preliminaries	8
4.1 Transport in Quantum Dots (QDs)	8
4.2 The Anderson Model	10
4.3 The Kondo Effect	12
4.3.1 Kondo Effect in QDs	14
5 Theory and Methods	16
5.1 Ballistic transport	16
5.1.1 Using Graph Theory to Solve Ballistic Transport Equations	18
5.1.2 Graph Algorithm	21
5.1.3 Ballistic transport in a double quantum dot	21
5.2 The Numerical Renormalization Group (NRG)	23
5.2.1 From the Renormalization Group to the Wilson's Chain	23
5.2.2 Iterative Diagonalization	25
5.2.3 Symmetries	26
5.2.4 Iterative diagonalization in a single QD Hamiltonian	27
5.2.5 The Density Matrix Renormalization Group (DM-NRG)	29
5.2.6 Specifications of the NRG Code	32
5.2.7 NRG results in a Double Quantum Dot Coupled to a Metallic Lead	33
6 Motivation: The Pursuit of Majorana Fermions	36
6.1 The Kitaev Chain	37
6.1.1 Topological phase transition	40
6.1.2 Non-abelian statistics	43
6.2 Real implementations of the Kitaev Chain	44
6.3 Coupling Majorana Fermions to QDs	46

6.3.1	Model	47
6.3.2	Non-interacting QD coupled to Majorana chain	48
6.3.3	Kondo-Majorana physics	51
6.3.4	State-of-the-art and prospective applications	53
7	Coupling the Majorana Zero Mode to a Double Quantum Dot	55
7.1	Applying our methods to the DQD-Majorana system	56
7.1.1	Non-interacting Green function:	56
7.1.2	NRG for the interacting system	58
7.2	Manipulation of Majorana zero modes	59
7.2.1	Non-interacting manipulation	60
7.2.2	Interacting manipulation	63
7.3	Additional results	68
7.3.1	Indirect exchange through the Majorana mode	68
7.3.2	Indirect Majorana coupling through the lead	69
7.3.3	Critical behavior in zero-bias DOS	70
8	Conclusions	71
	References	73
	Bibliography	73

Appendices

A	Appendix	80
	A.1 From the logarithmic discretization to the Wilson's chain.	80
B	Three peak appearance in the Double Quantum Dot model.	85
	B.1 Initial DQD-Majorana Hamiltonian.	86

Chapter 3

Motivation

In 2001 Alexei Yu. Kitaev presented a toy model for implementing qubits that could face the problem of high decoherence in quantum computation [1]. Kitaev's idea was centered in using the properties of an exotic quasi-particle that appears at the edges of a quantum superconducting chain. This quasi-particle receives the name of Majorana Fermion, is characterized for being its own anti-particle, thus it has no charge or spin. It also presents non-Abelian statistics, a desired property to implement fault-tolerant quantum computers[9]. These majorana fermions were theoretically predicted since the 1930's by one of the genius of the era, Ettore Majorana [10]. Although no fundamental Majorana-particle has been discovered to the date, Kitaev's model inspired the pursue of majorana fermions as quasi-particles in a novel exotic class of materials known as topological superconductors (TS)[11, 12, 3].

The last five years have been full of excitement, as new experiments have turned some of the theoretical predictions of the 1990s and 2000s into a reality. Very recently the first evidence of Majorana end states in TS has been found in multiple experiments [13, 14, 15] following the prescription by Oreg et al. [16] and Lutchyn et al. [17]. These experiments have been based on tunneling spectroscopy in junctions between TS and non metallic (NM) leads, where resonances have been observed at zero energy, consistent with the presence of Majorana zero-energy modes.

A downside of the tunneling spectroscopy technique in this case, is that it probes not only the end of the Topological Superconductor(TS), but its bulk as well , which completely destroys the qubit information. A less destroying model presented by Liu and Baranger [4] consists consists in attaching a Quantum Dot (QD) to the edges of a majorana chain in the topological phase and executing transport measurements through the QD [4] . The majorana mode at the end of the chain then leaks inside the QD [6] which produces a zero-bias conductance peak of half a quanta $\frac{e^2}{2h}$ through the dot. This is a majorana signature which produces half of the expected peak by a regular fermion.

In fact, this phenomenon is similar to the $\frac{e^2}{h}$ conductance peak caused by the Kondo effect [18]. Since topological superconductors and the Kondo effect could coexist at temperatures of a few mili-kelvins, it should be possible to observe combined Kondo-Majorana physics in this type of devices. This idea motivated an NRG study of a Quantum dot-Majorana hibrid system in the Kondo regime [8].

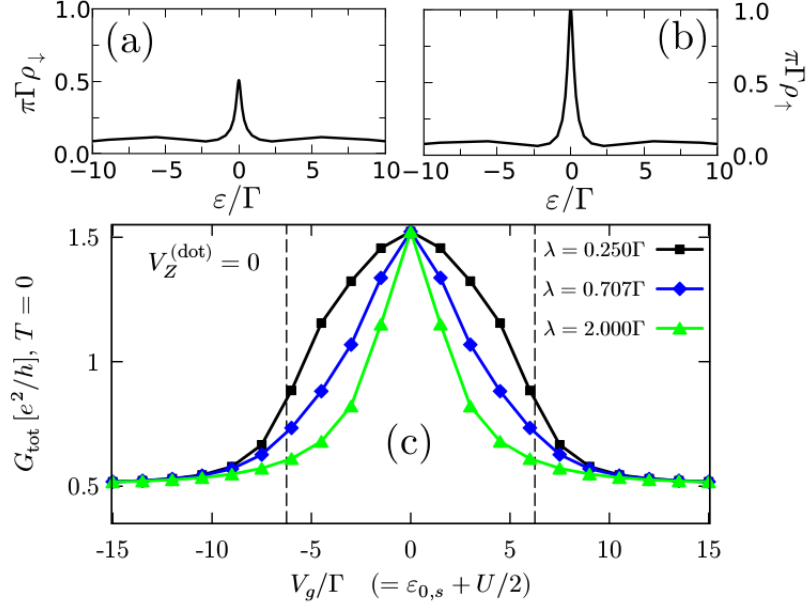


Figure 3.1: (a) QD spin-down density of states. Because this channel couples to the Majorana mode, it displays the characteristic zero-bias signature of amplitude $\frac{e^2}{2h}$. (b) QD spin-up density of states, displaying the zero-bias peak of the Kondo effect, with unit amplitude. (c) Zero-bias conductance of the QD coupled to the Majorana mode, as a function of the QD energy level (λ parameterizes the strength of the Majorana-QD tunnel coupling). The presence of the spin-up Kondo resonance enhances the QD conductance in particle-hole symmetry ($V_g = 0$), but quickly disappears as the QD level is detuned from this point. The spin-down Majorana signature, on the other hand, is robust [7], leaving a residual conductance of $\frac{e^2}{2h}$.

Source: [8].

This study revealed that transport measurements through the quantum dot will show contributions to the enhanced conductance coming from the Kondo effect and the Majorana mode: The Majorana mode at the end of the wire will migrate into one of the quantum dot spin channels, giving rise to a zero-energy peak in the density of states (Figure 3.1a)) contributing a conductance of $\frac{e^2}{2h}$ (Figure 3.1c)). The zero-bias peak from the Kondo effect appears in the other spin channel (Figure 3.1b)), contributing a conductance of $\frac{e^2}{h}$. Then, the Kondo effect can be “turned off” through gate voltages and magnetic fields, leaving only the Majorana contribution. Clear evidence of the destruction of the Kondo peak will appear in the conductance, allowing for a distinction between Majorana and Kondo signatures.

Apart from not destroying the entire qubit-information the QD-method has another insight. This is the possibility of manipulating Majorana fermions in multidot systems by shifting the QD gate voltages and tunnel couplings which brings possible applications in braiding procedures. The simplest system where Majorana manipulation is possible is a Double Quantum Dot (DQD) coupled to a majorana chain. By tuning the QD gate voltages and the majorana coupling we will be able to probe the mobility of the majorana modes through the dots.

In addition, when both dots are coupled to the lead the Double Quantum Dot exhibits an anti-ferromagnetic interaction known as Ruderman-Kittel-Kasuya-Yosida (RKKY) [19, 20, 21]. On the other hand, when only one dot is coupled and the second Dot is indirectly attached through the first dot, the Kondo effect is annihilated due to the destructive interference generated by extra dot [22]. Both cases reveal interesting results for majorana manipulation and hybrid Kondo-Majorana systems.

3.1 Structure

This thesis is integrated by 4-major chapters . In chapter 4, we will take a review to the basis of quantum transport in single electron transistors, the Anderson model and the emergence of the Kondo effect in quantum dots.

In chapter 5 contains a description of the methods that we will use to study the Double Quantum Dot-majorana system. The methods are the Zubarev's ballistic transport[23] for non-interacting systems and Wilson's Numerical Renormalization Group (NRG) technique [24] for interacting systems. We will use the Double Quantum Dot case as major example to explain both methods. Hence the background information about double quantum dots systems will be presented in this chapter.

The chapter 6 changes the subject, leading us to the mean topic of this thesis, Majorana fermions. The discussion will start with the Kitaev chain addressing its main characteristics such as topological characterization and non-abelian statistics . Then we take a look to the real implementations of majorana chains were we will discuss the most recent experimental accomplishments in the area. At the end, we face the the problem of a hybrid Quantum Dot-Majorana system using the methods described in chapter 5.

Using the methods from chapter 5 and the previous acquired experience with the Double Quantum Dot and the Quantum Dot-Majorana , we address in chapter 7 the Double Quantum Dot-Majorana system. We will study several procedures mainly focused in the manipulation of majorana fermions and the combined effects of Kondo-Majorana physics.

Chapter 4

Preliminaries

In this chapter we will give a brief description about transport processes in quantum dots (QDs). This will lead us to talk discuss the Anderson model and the Kondo effect, which are key ingredients in the objective of this project .

4.1 Transport in Quantum Dots (QDs)

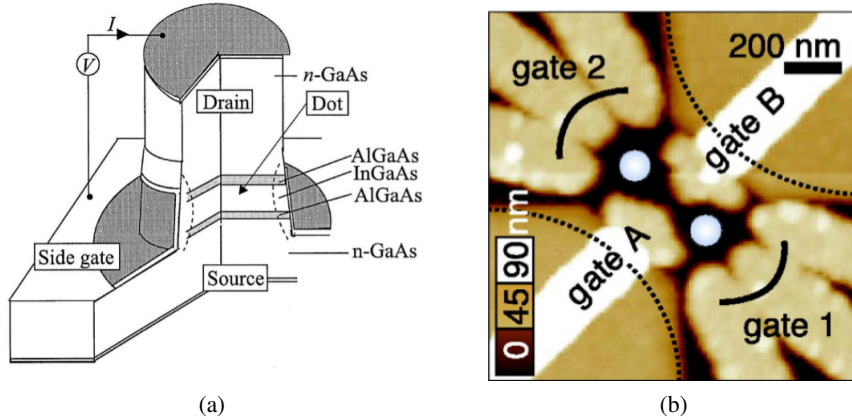


Figure 4.1: a) Vertical quantum dot. b) Atomic force microscopy picture of two coupled lateral QDs (bright central circles). Gates 1 and 2 act as drain and source voltage. A negative voltage is applied at gates A,B to allow the formation of the droplets inside the free space in the 2D electron gas.

Source: [25]

Quantum mechanical effects are visible when the system size is of the order of the de Broglie wavelength [26, (1.1)]

$$\lambda_f = \frac{h}{\sqrt{3m_{\text{eff}}k_B T}}$$

where m_{eff} is the electron effective mass in the crystal. Since m_{eff} can be much smaller than the free electron mass in some semiconducting materials, size quantization effects can be observed at system of sizes $\sim 100\text{nm}$ [27, 2.1]. A 0D quantum system is a device confined in the three

4.1. Transport in Quantum Dots (QDs)

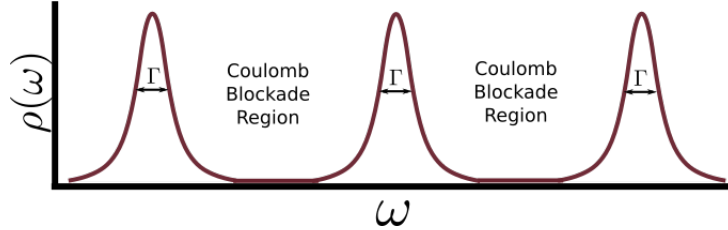


Figure 4.2: Pictorial representation of the Density of States of a QD. The gate potential V_G can be tuned to change the fermi energy of the dot.

Source: By the author

spacial dimensions up to this length-scale. This type of devices receive the name of quantum dots (QD).

Nowadays, QDs can be manufactured with different substracts, geometries and orientations [26]. They can be merged in structures like double quantum dots (4.1a) or can even be built out vertical to the base 2D-electron gas (4.1b). The precise experimental control over these devices allows to design atom-like structures with controllable energy levels. This has important applications on laser physics and in the implementation of single electron transistors.

Usually quantum dots have 3-main gates. Two of them are the Drain V_D and source V_S voltages used to control the electric gradient through the QD. The third one is the gate voltage V_G which allows to control with high precision the number of electrons inside the dot.

Ideally, the energy spectrum of a QD is a discrete set of energy levels resembling the spectrum of an atom. When the QD is connected to metallic leads these energy levels hybridized with respect to a broadening parameter Γ which increases as the square of the source-drain voltage V_{SD}

$$\Gamma \propto \pi \|V_{SD}\|^2 \quad (4.1)$$

in a flat band approximation. This broadening is depicted in Figure 4.2. Ideally, $\Gamma \ll \Delta E$ is smaller enough such that the energy levels do not overlap each other.

It is possible to execute transport measurements through a QD attached to two leads, source and drain (See 4.3a) . Each lead will have a characteristic gate voltage V_S (Left lead) and V_D (Right lead). An electron can pass from the source to the drain if there is an energy level in the middle of the two voltages, just as in 4.3a. If this condition is not satisfied, the dot enters into a coulomb blockade region without electron transport between both leads as can be observed in 4.3b. Inside the coulomb blockade regions described (black diamonds) the number of electrons is constant. When increasing V_G a single electron enters into the dot each time the system makes a transition between blockade regions. Since all of these effects can be controlled precisely with the gate voltage, the system described is indeed a single electron transistor (SET).

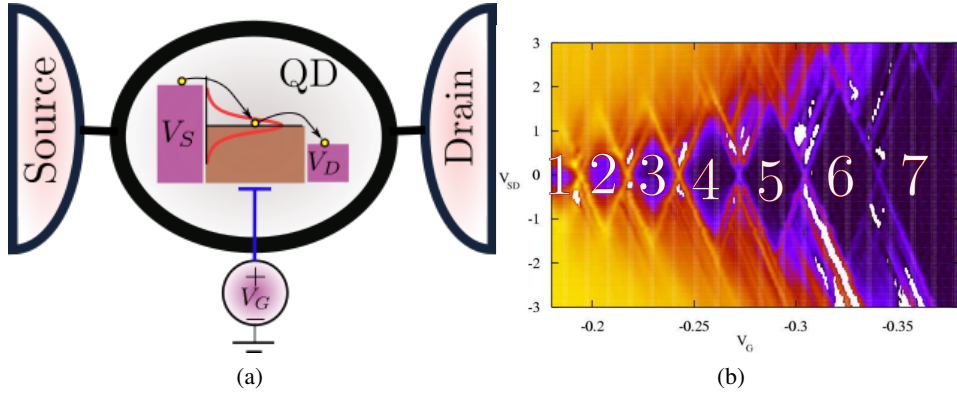


Figure 4.3: a) Representation of transport through QD. The red curve represents the hybridized energy level. The gate voltage tunes this level. In the case represented, the energy level is in the middle of the drain and source voltages allowing transport between the leads. b) Charging diagram of a quantum dot. Differential conductance dependence over the gate voltage V_G and the source-drain voltage ($V_{SD} = V_S - V_D$). Coulomb blockade occurs at the diamond-shaped regions with zero conductance. At these regions the number of electrons is constant and increases 1 by 1 when the gate voltage is scaled up.

Source: a) By the Author , b) Adapted from [27]

4.2 The Anderson Model

The Anderson model is used to describe quantum impurity systems where Coulomb repulsions and strongly correlated phenomena are dominant [28]. A quantum dot attached to a metallic lead is basically an artificial impurity that can be experimentally designed, modified and manipulated. Hence QDs are the perfect type of structure to probe the of the physics behind Anderson's ideas.

Due to the small confinement space inside these dots, the coulomb repulsion is relevant. However, it is usually impossible to provide a complete analytical description of these kind of systems due to the high correlations generated by this factor. Instead, we can obtain an overall description of the transport through the impurity by neglecting this coulomb repulsion. This will allow us to obtain some analytic intuition of the models before adventuring with long-lasting numerical simulations of interacting models. During this thesis, we will consider these two regimes as follows

- **Non-interacting systems:** Coulomb repulsion is not relevant . In this case, spin- \uparrow and spin- \downarrow channels are independent which simplifies many of the procedures. They can be described analytically through the ballistic transport approach.
- **Interacting systems:** The coulomb repulsion is relevant. The repulsion factor will be defined by the factor U which will take a fix value during the entire project. In this case,

4.2. The Anderson Model

spin- \uparrow and spin- \downarrow channels are not independent since the coulomb repulsion limits the number of particles inside each dot. We will use the Numerical Renormalization Group to treat this case. The intuition acquired from non-interacting systems will help us to select the input parameters of the algorithm.

To build the Anderson model first consider that we have a QD (impurity) coupled to the conduction band of a metallic lead. We will define a coulomb repulsion factor U which will be set to 0 if the system is non-interacting. Using the Hunds rules we know that the energy levels inside the dot should be filled from lower to higher energies with two electrons with different spin at each state. Each pair of electrons will interact magnetically and electrically. In addition, there is an energy term associated to each electron and a Zeeman splitting factor in case a \hat{z} -directed magnetic field B is placed. Considering these interactions we can obtain a very general expression in second quantization for the QD Hamiltonian of the form [27, (3.2)]

$$H_d = \sum_{i\sigma} \varepsilon_{di} d_{i\sigma}^\dagger d_{i\sigma} + \sum_i U_i \hat{n}_{i\uparrow} \hat{n}_{i\downarrow} + \sum_{\sigma\sigma', i \neq j} U_{ij} \hat{n}_{i\sigma} \hat{n}_{j\sigma'} - \mu_B g B \sum_i S_i^z + J \sum_{i \neq j} \mathbf{S}_i \cdot \mathbf{S}_j.$$

Where $\sigma \in \{\uparrow, \downarrow\}$, $d_{i\sigma}^\dagger$ ($d_{i\sigma}$) is the dot creation(annihilation) operator, $\hat{n}_{i\sigma} := d_{i\sigma}^\dagger d_{i\sigma}$ is the particle number, \mathbf{S}_i is the spin-vector, ε_{di} is the energy of the i^{th} -level in the dot, U_i is the coulomb repulsion between electrons in the same energy level i , U_{ij} is the coulomb interaction between electrons in different levels (And therefore smaller than U_i), B is an applied magnetic field in the \hat{z} -direction and J is the term representing the Zeeman splitting.

At low temperatures, the quantum interactions occur only with the level closest to the Fermi energy. This allows us to make the single-level approximation, neglecting the other energy levels. This assumption reduces the complexity of the dot Hamiltonian to

$$H_d = \sum_{\sigma} \varepsilon_d d_{\sigma}^\dagger d_{\sigma} + U \hat{n}_{\uparrow} \hat{n}_{\downarrow} - \mu_B g B S^z. \quad (4.2)$$

Besides to the dot Hamiltonian, we need to consider the energy of the electrons in the lead H_{lead} and the dot-lead interaction H_{int} . We can model the conduction band of the lead as a 2D electron gas with the following Bloch Hamiltonian

$$H_{\text{lead}} = \sum_{\mathbf{k}\sigma l} \varepsilon_{\mathbf{k}l} c_{\mathbf{k}\sigma l}^\dagger c_{\mathbf{k}\sigma l}. \quad (4.3)$$

where \mathbf{k} represents the possible crystal momentums in the leads, $l \in \{S, D\}$, $c_{\mathbf{k}\sigma l}^\dagger$ ($c_{\mathbf{k}\sigma l}$) creates(annihilates) an electron with momentum \mathbf{k} and spin σ in the lead l , $\varepsilon_{\mathbf{k}l}$ is the energy of the electron in the leads.

The interaction between the dot and the leads is then given by

$$H_{\text{int}} = \sum_{\mathbf{k}\sigma l} V_{\mathbf{k}} c_{\mathbf{k}\sigma l}^\dagger d_{\sigma} + V_{\mathbf{k}}^* d_{\sigma}^\dagger c_{\mathbf{k}\sigma l}, \quad (4.4)$$

4.3. The Kondo Effect

where $V_{\mathbf{k}l}$ is a hopping exchange term between the leads and the QD.

The sum of all of these three interactions is receives the name of Anderson Model.

$$\begin{aligned} H &= H_d + H_{lead} + H_{int} \\ &= \sum_{\sigma} \varepsilon_d d_{\sigma}^{\dagger} d_{\sigma} + U \hat{n}_{\uparrow} \hat{n}_{\downarrow} - \mu_B g B S^z + \sum_{\mathbf{k}\sigma l} \varepsilon_{\mathbf{k}l} c_{\mathbf{k}\sigma l}^{\dagger} c_{\mathbf{k}\sigma l} + \sum_{\mathbf{k}\sigma l} V_{\mathbf{k}l} c_{\mathbf{k}\sigma l}^{\dagger} d_{\sigma} + V_{\mathbf{k}l}^* d_{\sigma}^{\dagger} c_{\mathbf{k}\sigma l}. \end{aligned} \quad (4.5)$$

For this project, we will make two extra changes to the Anderson model. Using the anti-commutation properties of the fermion operators

$$\{d_{\sigma}^{\dagger}, d_{\sigma'}\} = \delta_{\sigma\sigma'}, \quad \{d_{\sigma}^{\dagger}, d_{\sigma'}^{\dagger}\} = \{d_{\sigma}, d_{\sigma'}\} = 0$$

we get

$$\begin{aligned} (d_{\uparrow}^{\dagger} d_{\uparrow} + d_{\downarrow}^{\dagger} d_{\downarrow} - 1)^2 &= \sum_{\sigma} (d_{\sigma}^{\dagger} d_{\sigma})^2 - 2 \sum_{\sigma} d_{\sigma}^{\dagger} d_{\sigma} + 2 d_{\uparrow}^{\dagger} d_{\uparrow} d_{\downarrow}^{\dagger} d_{\downarrow} - 1 \\ &= 2 d_{\uparrow}^{\dagger} d_{\uparrow} d_{\downarrow}^{\dagger} d_{\downarrow} - \sum_{\sigma} d_{\sigma}^{\dagger} d_{\sigma} - 1. \end{aligned}$$

Replacing this in (Equation 4.2) we obtain a nice spin-symmetric form of the dot hamiltonian

$$\left(\varepsilon_d + \frac{U}{2} \right) d_{\sigma}^{\dagger} d_{\sigma} + \frac{U}{2} (d_{\sigma}^{\dagger} d_{\sigma} - 1)^2 - \mu_B g B S^z. \quad (4.6)$$

In addition, it is possible to do a linear transform to the lead operators

$$\frac{1}{\sqrt{V_S^2 + V_R^2}} \begin{bmatrix} V_S & V_R \\ -V_R & V_S \end{bmatrix} \begin{bmatrix} c_{\mathbf{k}\sigma S} \\ c_{\mathbf{k}\sigma D} \end{bmatrix} = \begin{bmatrix} c_{\mathbf{k}\sigma+} \\ c_{\mathbf{k}\sigma-} \end{bmatrix} \quad (4.7)$$

After the transformation the operator will be decoupled from the dot hamiltonian $c_{\mathbf{k}\sigma-}$. This implies that we can suppose that the **dot is coupled wit just one lead**. During the rest of the thesis we will maintain this convention.

4.3 The Kondo Effect

The Kondo effect is one of the biggest condensed matter problems in the 20th century. There was an uncountable number of experimental and theoretical physicist that contributed to this problem. The most reknown are probably the physicists Jacques Friedel, Jun Kondo and the two nobel prizes Philip Anderson and Kenneth Wilson [18].

The history of the Kondo effect began in the early 1930s. By that time it was known that the resistivity of a metal is regulated by different scattering interactions against lattice phonon

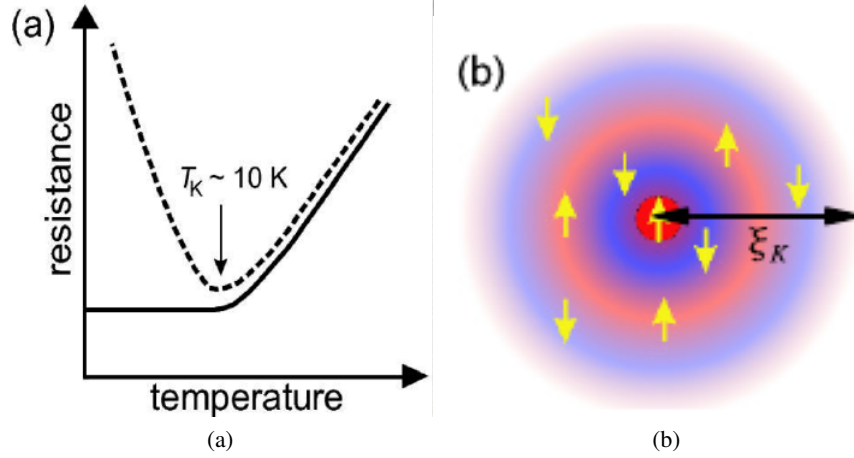


Figure 4.4: a) Resistivity minimum near the Kondo temperature T_K . b) Kondo cloud formed by a singlet grouped around the impurity divided in spin- \uparrow ,spin- \downarrow regions.

Source: a) [29], b) [?]

vibrations $\rho_{phonon} \sim T^5$, other electrons $\sim T^2$ and static impurities, which is temperature independent. The form of these contribution clearly implies that the resistivity should decay uniformly with a decreasing temperature. Nevertheless, some groundbreaking experiments revealed the observation of a resistance minimum in some metals at temperatures lower than 10K [29] (See 4.4a).

This phenomenon intrigued the scientific community for the following decades until the year 1964 when the physicist Jun Kondo gave the first convincing solution to this puzzle. Kondo attributed the phenomenon to the scattering of the electrons due to the spin-interaction with a small concentration of magnetic impurities in the metal. To describe it he proposed the following interaction Hamiltonian

$$H_K = 2J\hat{\mathbf{S}} \cdot \hat{\mathbf{s}} \quad (4.8)$$

$$= J(2S_zs_z + S_+s_- + S_-s_+) \quad (4.9)$$

with $S_{\pm} = S_x \pm iS_y$. The hamiltonian H_K which is better known as the Kondo s-d model describes the spin interaction between the spin of the impurity $\hat{\mathbf{S}}$ and the spin of the particles in the metal $\hat{\mathbf{s}}$.

Kondo took H_K as a perturbation of the electron gas inside metallic lead, with J the perturbation parameter. While the first order led to no important contribution, Kondo was able to obtain on second order perturbation theory a logarithmic correction on the temperature in the resistivity of the form

$$\rho_{imp} \propto \ln \frac{T_K}{T}, \quad (4.10)$$

where T_K received the name of Kondo temperature. Summing up this term to the other resistivity contributions we obtain the full expression

$$\rho_{metal}(T) = \rho_{imp} + a_e T^2 + b_{Phonon} T^5 + c_m \ln \frac{T_K}{T}. \quad (4.11)$$

Note that when $T < T_K$ the term $\ln \frac{T_K}{T}$ increases. Eventually, it compensates the decaying resistivity which finally explained the resistance minimum.

Although Kondo's explanation was initially very successful it also presented a troublesome outcome. The logarithmic term introduced by Kondo diverges when the temperature approximates to 0, hence proving to be inefficient at temperatures well below T_K . Going to the following orders in perturbation theory also led to divergent resistivities which led to explore non-perturbative approaches to solve the Kondo effect.

On the other hand, Anderson had already created his famous impurity model. One of his main contributions was the inclusion of the Hubbard term to represent the Coulomb interaction inside the dot, which proved to be fundamental to understand the Kondo effect. Years later, Kenneth Wilson was able to effectively diagonalize the Anderson model using a numerical method that combines ideas from scalability and the renormalization group.

Wilson's explanation solved the Kondo problem almost completely. It turned out that at very low temperatures, the impurity entangles with the low-energy electrons forming a strongly correlated many-body singlet. This singlet surrounds the impurity in a structure formed by alternating regions of spin- \uparrow and spin- \downarrow particles called the Kondo cloud (See Figure 4.4b). This Kondo cloud is predicted to have an astonishing correlation length between $0.1\mu m$ to $10\mu m$. This is a huge radius if we think that the impurity(or QD) can have a radius below $1nm$. The Kondo effect, is produced when the conduction electrons scatter with the Kondo cloud, which increases the resistivity of the material.

4.3.1 Kondo Effect in QDs

The problem of magnetic impurities in metals can be treated using the Anderson model in a similar form as the transport in quantum dots. Hence, it is not a surprise that the Kondo Effect could also occur in these systems. In 1998 the technological advances allowed the observation of the Kondo effect for the first time in a single electron transistor [31]. When an odd number of electrons is in the QD the last level below the Fermi energy is half-occupied and hence the dot can be considered as a magnetic impurity. The unlocalized electrons in the reservoirs then interact with this localized electron. Spin-exchange can occur as it happened with magnetic impurities in metals. At low temperatures, this magnetic interaction gives rise to strong quantum correlations that favor the formation of a singlet state between the localized electron and the electrons in the leads. As a result, the zero-bias density of states is increased producing a

4.3. The Kondo Effect

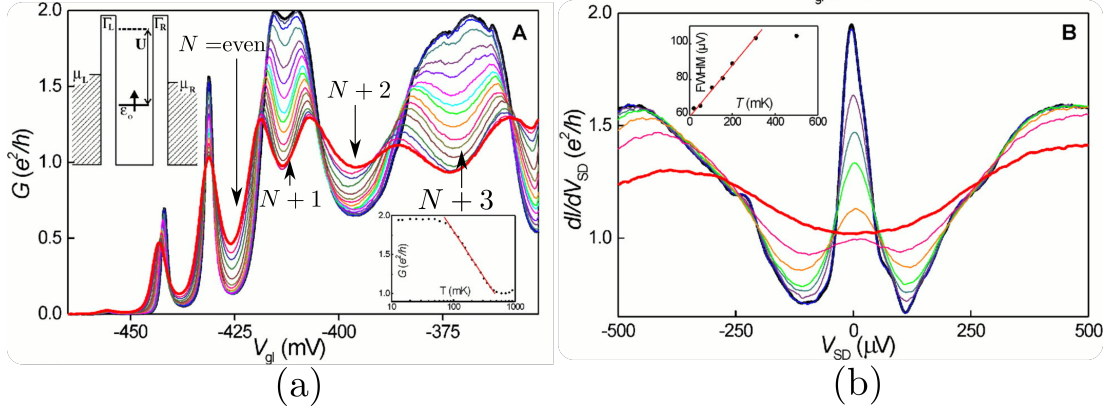


Figure 4.5: Observation of the Kondo effect in a single electron transistor. Color scale temperatures from 15mK (Black) to 800mK(Red) a) Dependence of the zero bias conductance over the gate voltage. A plato in the conductance peak appears in the odd particle regimes. b) Dependence of the conductance over the gate source drain voltage inside an odd electron regime. A zero bias conductance peak (ZBCP) of height $\frac{2e^2}{h}$ is observed. This is the Kondo signature.

Source: [30]

zero-bias conductance peak Figure 4.5(b).

Note that the physical implications of the Kondo effect between the case of magnetic impurities in metals and transport through QD are different. The reason for this are the dimensions of the system. While the scattering at 3D systems against magnetic impurities is an obstacle to conduction electrons, the scattering in 0D systems enhances the conductivity of the QD since there is only one scattering direction.

As we previously discussed, transport in quantum dots can occur only if there is a state in the middle of the drain and source voltage. The Kondo effect creates a zero bias peak that is present whenever the dot has odd electrons . This explains the zero-bias plateaus observed in Figure 4.5(a). We may think that the new singlet state at the Fermi energy is creating a "channel" that allows quantum transport between both sides of the dot.

Chapter 5

Theory and Methods

In this chapter we describe the two methods that we will use to compute the density of states in this project. Using the ballistic transport method, we will obtain an exact analytical expression of this quantity for non-interacting systems (section 5.1). The physics of interacting systems is more complex and does not support an exact approach. Instead, we appeal to the renown numerical renormalization group (NRG) to deal with the strong correlations of these systems section 5.2 . Both models will be tested on the model of a double quantum dot attached to a metallic lead. We will observe that at very low energies, the physics of interacting systems emulates characteristic features of non-interacting models.

5.1 Ballistic transport

The Green function G of a Hamiltonian H is the operator that satisfies the homogeneous equation

$$\left(i\hbar \frac{\partial}{\partial t} - H \right) G(t-t') = \delta(t-t'). \quad (5.1)$$

This type of differential equations are solved taking the Fourier transform

$$G_H(\omega) = \int_{-\infty}^{\infty} G(t-t') e^{i\omega(t-t')/\hbar} \delta(t-t') \quad (5.2)$$

In this new space the solution of the equation is

$$(\omega + is - H)G_\omega(\omega) = I.$$

The term $+is$ in the previous Hamiltonian is part of a mathematical trick quite common in this theory. During the whole procedure, the Green function acts on the complex field. But when we need to obtain a physical interpretation we will take the limit $s \rightarrow 0$ to obtain the result for real energies.

The next step is to decompose $G_H(\omega)$ in the eigenbase of the Hamiltonian $\{|\alpha\rangle\}$ by

$$\langle \alpha | G_H(\omega) | \alpha' \rangle = \frac{\delta_{\alpha\alpha'}}{\omega - is - \varepsilon_\alpha} = \frac{\delta_{\alpha\alpha'}(\omega + is - \varepsilon_\alpha)}{(\omega - \varepsilon_\alpha)^2 + s^2}. \quad (5.3)$$

From the famous formula

$$\lim_{s \rightarrow 0} \frac{s}{(\omega - \varepsilon_\alpha)^2 + s^2} = \pi \delta(\omega - \varepsilon_\alpha) \quad (5.4)$$

we obtain

$$Im[\langle \alpha | G_H(\omega) | \alpha' \rangle] = \pi \delta(\omega - \varepsilon_\alpha) \delta_{\alpha, \alpha'}. \quad (5.5)$$

Note that the sum of $Im[\langle \alpha | G_H(\omega) | \alpha' \rangle]$ over all the eigenstates of H is simply π times the density of states:

$$\rho(\omega) = -\frac{1}{\pi} \sum_{\alpha} Im[\langle \alpha | G_H(\omega) | \alpha' \rangle] = \sum_{\alpha} \delta(\omega - \varepsilon_{\alpha}). \quad (5.6)$$

An extended definition of the Green function can be given in terms of fermion operators in second quantization. The time-green function for two fermion operators A and B is

$$G_{A,B}(t - t') = \mathbb{T}[\{A(t), B(t')\}]. \quad (5.7)$$

In these problems, causality is important, which is the reason why we use the time-order operator \mathbb{T} . In addition, the evolution of this Green function is determined by Schroedinger's differential equation.

$$\frac{d}{dt} G_{A,B}(t - t') = \langle [A(t), B(t')] \rangle \delta_{t-t'} + \langle [A(t), H'] , B(t') \rangle \quad (5.8)$$

Once again, we perform a Fourier transform of $G_{A,B}(t - t')$ to obtain $G_{A,B}(\omega)$. When applying this transform to Equation 5.8 we obtain

$$\omega G_{A,B}(\omega) = \delta_{A^\dagger, B} + G_{[A,H],B}(\omega). \quad (5.9)$$

Applying Equation 5.9 to a set of operators $\{A_1, A_2, \dots\}$ we obtain a whole set of transport equations describing the flow of state transitions of the operators in our model. In this thesis we will identify each set of equations with a flow graph. This will be our leading method to compute the green functions of the system.

Moreover, following equation Equation 5.6 we can define the density of states associated to an operator A as

$$\rho_{A,A^\dagger} = -\frac{1}{\pi} Im[G_{A,A^\dagger}(\omega)]. \quad (5.10)$$

The density of states contains important physical information related to operator A . In our case, operator A^\dagger will be related to the dot's creation operator d^\dagger . Hence computing Equation 5.10 will allow us to observe the hybridization of the dot's discrete states and the creation of other energy levels due to the interaction with the lead and other possible impurities. We will observe examples of these computations in the following sections.

5.1.1 Using Graph Theory to Solve Ballistic Transport Equations

Solving the transport equations involves dealing with a set of linear equations where all the possible variables including ω , and the Hamiltonian parameters are assumed to be constant. This can be done by Gauss-Jordan elimination, noting that after each elimination process we need to carry on the account in terms of the initial variables. The solution will be a polynomial fraction. When the number of operators in the Hamiltonian increases the number of terms in the polynomial grows-up rapidly according to the number of initial parameters. This reveals the importance of exploring new methods that could simplify the solution of this system, and present a readable factorized expression of the final solution.

The method presented here uses graph theory algorithms that provide a shortcut to Gauss-Jordan elimination [32]. To probe this method we solve here the transport equations for a non-interacting ($U = 0$) DQD connected to one lead.

According to the Anderson model the Hamiltonian for this system looks like

$$H = \sum_{i=1}^2 \epsilon_{di} d_i^\dagger d_i + t_{dots} d_1^\dagger d_2 + t_{dots}^* d_2^\dagger d_1 + \sum_k \left(V_i d_i^\dagger c_k + V_i^* c_k^\dagger d_i \right) + \epsilon_k c_k^\dagger c_k. \quad (5.11)$$

Since the system is non-interacting, we ignore the spin-degeneracy of this Hamiltonian. The only new parameter here is the term t_{dots} , which represents the tunneling between both quantum dots. Using equation (Equation 5.9) with $B = d_1^\dagger$ and A shifting among other operators we compute the following transport equations

$$(\omega - \epsilon_1) G_{d_1, d_1^\dagger}(\omega) = 1 + t_{dots} G_{d_2, d_1^\dagger}(\omega) + V_1^* \sum_k G_{c_k, d_1^\dagger}(\omega) \quad (5.12)$$

$$(\omega - \epsilon_k) G_{c_k, d_1^\dagger}(\omega) = V_1 G_{d_1, d_1^\dagger}(\omega) + V_2 G_{d_2, d_1^\dagger}(\omega) \quad (5.13)$$

$$(\omega - \epsilon_2) G_{d_2, d_1^\dagger}(\omega) = t_{dots} G_{d_1, d_1^\dagger}(\omega) + V_2^* \sum_k G_{c_k, d_1^\dagger}(\omega) \quad (5.14)$$

This system is already closed which means that we don't need any other equation to find the solution. The associated matrix form is

$$\begin{bmatrix} \omega - \epsilon_2 & -V_2 & -t_{dots} \\ -V_2^* & \omega - \epsilon_k & -V_1 \\ -t_{dots}^* & -V_1^* & \omega - \epsilon_1 \end{bmatrix} \begin{bmatrix} G_{c_k, d_1^\dagger}(\omega) \\ G_{d_2, d_1^\dagger}(\omega) \\ G_{d_1, d_1^\dagger}(\omega) \end{bmatrix} = \begin{bmatrix} 0 \\ 0 \\ 1 \end{bmatrix} \quad (5.15)$$

By convenience we changed the order of the rows in the matrix and we removed the sum over k (\sum_k) to simplify the algebraic operation. We will insert these terms back in the equations at the end of the procedure.

Although this matrix is not Laplacian, the procedure in [32] can still be applied with the downside of loosing part of the speed-up of the algorithm. We still preserve some of the advantages using graphs, such as the possibility of taking minimal cuttings and the relation between

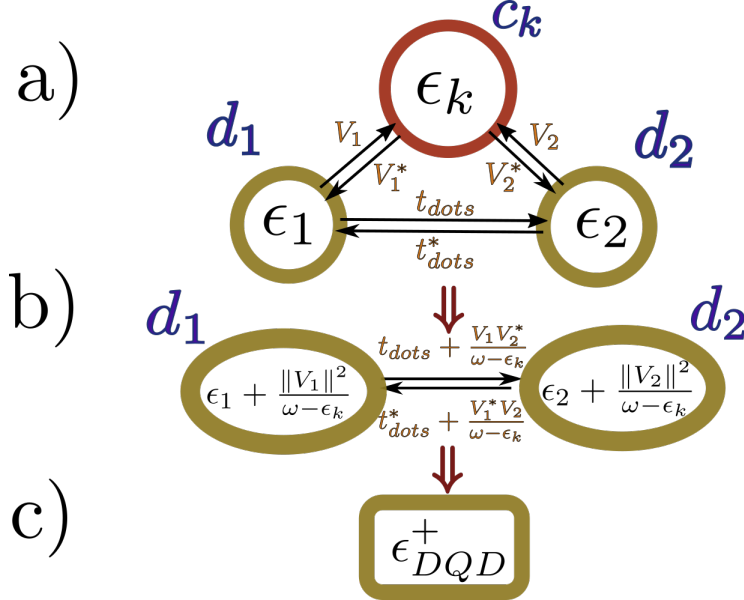


Figure 5.1: Graph representation of Gauss-Jordan elimination a) Graph $\mathcal{G}_{d_1 d_2}$ b) After the elimination of vertex c_k , the energies of dots d_1 and d_2 , and the coupling parameter are changed. c) After Gaussian elimination of dot 2 the energy of the remaining dot ϵ_{DQD}^+ represents the transport information through d_1 of the entire DQD.

Source: By the author.

Gauss-Jordan elimination and random walks [32]. Both advantages simplify the complexity of the solution.

Now, our objective is to compute the green function $G_{d_{1\downarrow}, d_{1\downarrow}^\dagger}(\omega)$. For this we take the graph $\mathcal{G}_{d_1 d_2}$ associated to the matrix (Equation 5.15). See Figure 5.1.a). The vertexes of this graph are the operators in the first site of the of the green functions ($d_{1\downarrow}, d_2, c_k, d_1^\dagger$). d_1^\dagger is not included since it only appears in the second sub-index of the green functions. The edges are given by the non-diagonal sites in the matrix. In addition, an energy parameter is assigned to each vertex, according to the corresponding term in the diagonal. These energies can also be thought as the magnitude of edges connecting each vertex with itself. The plot of the energy parameters in this algorithm is quite important, hence we prefer to keep this name to differentiate them from the other couplings.

The algorithm consists in the following. Each step of Gauss-Jordan elimination leads to a new graph with different energies and couplings. The elimination of a row and column is equivalent to pop the corresponding vertex in the graph. For instance, lets eliminate the first row and column of the matrix in (Equation 5.15). For it we just need to subtract the rank-1

5.1. Ballistic transport

matrix with the same first row and first column

$$\begin{bmatrix} \omega - \varepsilon_k & -V_2 & -V_1 \\ -V_2^* & \omega - \varepsilon_2 & -t_{dots} \\ -V_1^* & -t_{dots}^* & \omega - \varepsilon_1 \end{bmatrix} - \begin{bmatrix} \omega - \varepsilon_k & -V_2 & -V_1 \\ -V_2^* & \frac{V_2^* V_2}{\omega - \varepsilon_k} & \frac{V_2^* V_1}{\omega - \varepsilon_k} \\ -V_1^* & \frac{V_2 V_1^*}{\omega - \varepsilon_k} & \frac{V_1 V_1}{\omega - \varepsilon_k} \end{bmatrix} \quad (5.16)$$

$$= \begin{bmatrix} 0 & 0 & 0 \\ 0 & \omega - \varepsilon_2 - \frac{V_2^* V_2}{\omega - \varepsilon_k} & -t_{dots} - \frac{V_2^* V_1}{\omega - \varepsilon_k} \\ 0 & -t_{dots}^* - \frac{V_2 V_1^*}{\omega - \varepsilon_k} & \omega - \varepsilon_1 - \frac{V_1 V_1}{\omega - \varepsilon_k} \end{bmatrix} \quad (5.17)$$

The graph associated to this matrix can be observed in Figure 5.1.b) where operator c_k has been popped out of the graph. It is possible to associate the correction to the the energies and couplings to the possible walks passing through the vertex c_k . For instance d_1 's energy ε_1 receives an extra-term $\frac{V_1^* V_1}{\omega - \varepsilon_k}$ representing an additional walk from d_1 to d_1 passing through c_k . The same logic can be applied to the other terms coupling terms. The correction to t_{dots} is $\frac{V_1^* V_2}{\omega - \varepsilon_k}$ which corresponds to a path from d_1 to d_2 passing through the popped vertex c_k . Note that this term includes the multiplication both couplings with the vertex divided by the difference of ω with the energy of the vertex. This correspondence between the energy correction and eliminated paths through the graph makes the "popping" process an straightforward task.

We now proceed to pop vertex d_2 which leaves just a single vertex as shown in Figure 5.1.c). The energy of it can be readily computed with the previous path elimination idea which gives

$$\varepsilon_{DQD}^+ = \varepsilon_1 + \sum_{\mathbf{k}} \frac{V_1 V_1^*}{\omega - \varepsilon_{\mathbf{k}}} + \frac{\left\| t_{dots} + \sum_{\mathbf{k}} \frac{V_1 V_2^*}{\omega - \varepsilon_{\mathbf{k}}} \right\|^2}{\omega - \varepsilon_2 - \sum_{\mathbf{k}} \frac{V_2 V_2^*}{\omega - \varepsilon_{\mathbf{k}}}}, \quad (5.18)$$

where we selectively included the $\sum_{\mathbf{k}}$ -terms in the places where k appeared.

As a result of Gauss-Jordan elimination the linear equation in Equation 5.15 has evolved into the trivial form

$$\begin{bmatrix} 0 & 0 & 0 \\ 0 & 0 & 0 \\ 0 & 0 & \omega - \varepsilon_{DQD}^+ \end{bmatrix} \begin{bmatrix} G_{c_{\mathbf{k}}, d_1^\dagger}(\omega) \\ G_{d_2, d_1^\dagger}(\omega) \\ G_{d_1, d_1^\dagger}(\omega) \end{bmatrix} = \begin{bmatrix} 0 \\ 0 \\ 1 \end{bmatrix}. \quad (5.19)$$

The Green function is then

$$G_{d_1, d_1^\dagger}(\omega) = \frac{1}{\omega - \varepsilon_{DQD}^+} = \left[\left(\omega - \varepsilon_1 - \sum_{\mathbf{k}} \frac{V_1 V_1^*}{\omega - \varepsilon_{\mathbf{k}}} \right) - \frac{\left(t_{dots} + \sum_{\mathbf{k}} \frac{V_1 V_2^*}{\omega - \varepsilon_{\mathbf{k}}} \right) \left(t_{dots} + \sum_{\mathbf{k}} \frac{V_1 V_2^*}{\omega - \varepsilon_{\mathbf{k}}} \right)^*}{\omega - \varepsilon_2 - \sum_{\mathbf{k}} \frac{V_2 V_2^*}{\omega - \varepsilon_{\mathbf{k}}}} \right]^{-1}. \quad (5.20)$$

This Green function will be very important in the following chapters where we will compare its behavior with the green function of a Majorana mode.

5.1.2 Graph Algorithm

In this part we summarize the steps of the graph algorithm in order to apply them later to more complicated systems:

1. Computing the transport equations with the second term fixed in the creation operator of d^\dagger .
2. Writing the graph associated to the transport system. The vertexes are the operators in the first site of the of the green functions. Energies and couplings are associated to the vertex and edge numbers of the graphs respectively.
3. Popping the vertexes of the graph. Each vertex popping involves the following steps.
 - (a) Computing the extra-terms in the energies and couplings based on the walks passing through the popped vertex.
 - (b) Eliminating this vertex from the graph.
 - (c) Iterating till there is only the vertex d .
4. The energy in the remaining vertex d is $\varepsilon_d = \frac{1}{\omega - G_{d,d^\dagger}(\omega)}$.

This algorithm will be our main method to find the green function and therefore the density of states of any interacting system.

5.1.3 Ballistic transport in a double quantum dot

In this subsection we describe the remaining steps to extract the density of states of the double quantum dot from the Green function Equation 5.20. We will plot the results and observe the evolution of the DOS while tuning the parameters of the model.

First note that equation (Equation 5.20) depends on the term $\sum_k \frac{V_i^* V_j}{\omega - \varepsilon_k}$ which describes the broadening of the DOS when the QD enters in contact with the lead. This broadening is usually named $\Gamma_i = V_i^* V_i$ (Or Δ depending on the text book). In general V_i is a function of \mathbf{k} . However, in the limit of flat-band we can assume that V_i is constant. Therefore, it is enough to integrate

$$\sum_k \frac{1}{\omega - \varepsilon_k + is} = \int_{-D}^D \frac{d\varepsilon_k}{\omega - \varepsilon_k + is} = -\ln \left(\frac{D - \varepsilon_k + is}{-D - \varepsilon_k + is} \right) \xrightarrow[D \rightarrow \infty]{} -i, \quad (5.21)$$

where we assumed that there is a maximum energy cutoff D going to infinity in the wide-band limit. Hence

$$-i\Gamma_i = \sum_k \frac{V_i^* V_i}{\omega - \varepsilon_k}. \quad (5.22)$$

We can replace this in equation (Equation 5.20) to obtain the real expression for the green function $G_{d_1, d_1^\dagger}(\omega)$. The terms of the form $V_1 V_2^*$ can be replaced for $\sqrt{\Gamma_1 \Gamma_2}$, supposing there is no additional complex phase.

5.1. Ballistic transport

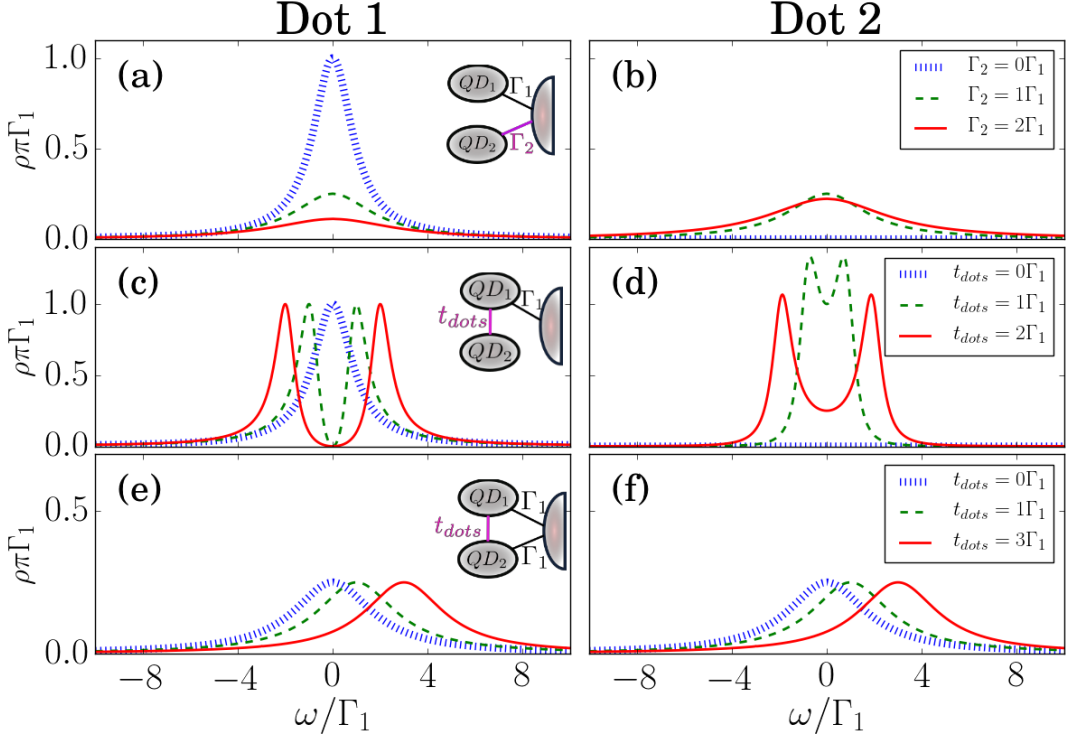


Figure 5.2: Evolution of the density of states at each QD (Left: dot 1, Right: dot 2) at three distinct arrangements of DQD-lead coupling. The inset at the first column depicts the type of coupling. The purple line represents the tuning variable. The energy unit is Γ_1 . $e_1 = e_2 = 0$ in all arrangements. (a),(b) The lead is connected to both QDs. Tuning variable: Γ_2 . (c)(d) Indirect coupling of the second dot through dot one. Tuning variable: t_{dots} . (e)(f) Triangular coupling. Tuning variable: t_{dots} .

Source: By the Author

Now, remember from (Equation 5.10) that the DOS ρ depends on the imaginary factor of the Green Function $G_{d_1,d_1^\dagger}(\omega)$. This term depends in the broadening Γ . If $\Gamma = 0$ the density of states will be 0 as well. At any other case, one of the dots should be attached to the lead. Let Γ_1 be the broadening of this dot. We will take Γ_1 as our natural unit for the rest of this thesis.

In Figure 5.2 we can observe the evolution of the Density of States under certain processes. Each plot includes an inset showing the model applied to the figure. The coupling in purple indicates the tuning variable. We set $e_1 = e_2 = 0$ so that both dots satisfy PHS. The primary results are the

- Coupling QD2. Figure 5.2(a)(b):** At $\Gamma_2 = 0$ the second dot is decoupled, hence the first dot's DOS is the same of a single dot case. The maximum height is achieved at $\rho\pi\Gamma_1 = 1$

and the width of this peak is about Γ_1 , just as in Figure 4.2. When the second dot is attached $\Gamma_2 > 0$ the density of states is divided between both dots. At $\Gamma_1 = \Gamma_2$ the DOS at the Fermi energy is equal to $\frac{1}{4\pi\Gamma}$ for both dots. For higher values of Γ_2 the DOS in the second dot is higher than in the first one.

2. **Indirect Coupling of QD2.** **Figure 5.2(c)(d):** This case is interesting. When the second dot is connected indirectly through the first dot, quantum interference splits the central peak in two new states. We will observe later that in the interacting case this procedure can also destroy the Kondo signature. Note that the higher the coupling t_{dots} is, the greater is the gap between the states. We will usually take $t_{dots} = 2\Gamma_1$ to make these gaps more visible in the NRG simulations.
3. **Breaking Particle Hole Symmetry.** **Figure 5.2(e)(f):** Suppose we have $\Gamma_2 = \Gamma_1$. The "triangular connections" break Particle Hole Symmetry. The central peak is displaced to the positive part of the spectrum. We will avoid this situation during this project, because because PHS-breaking will prevent the Majorana to tunnel inside the DQD. Hence, this model won't lead to any interesting result on Majorana manipulation.

5.2 The Numerical Renormalization Group (NRG)

5.2.1 From the Renormalization Group to the Wilson's Chain

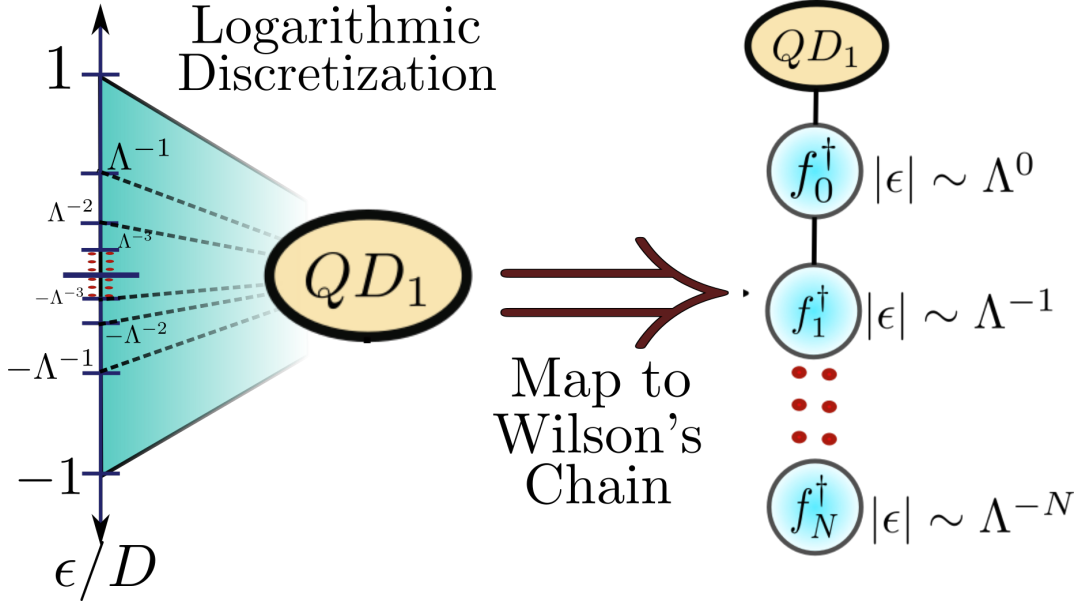
The real meaning of divergent logarithmic term in the resistivity predicted by Kondo is that important contributions at low-energy scales caused by the strong quantum correlations in the system are being neglected by perturbation theory. This problem can be solved by introducing ideas from renormalization group theory. A renormalization approach is more adequate for this type of problem since it assigns an appropriate effective Hamiltonian to each scale of temperature. This provides a more accurate representation of the increasing density of correlated states appearing close to the Fermi energy.

In renormalization group theory, the Hamiltonian transformations are performed by an operator \mathcal{T} that represents an endomorphism in the space of operators. T generates the semigroup $\{1, \mathcal{T}, \mathcal{T}^2, \dots\}$, that defines a complete set of transformations

$$\mathcal{T}[H_0] = H_1, \mathcal{T}[H_1] = H_2, \dots, \mathcal{T}[H_N] = H_{N+1}, \dots$$

If \mathcal{T} is a contracting map¹ then it is known that this set of operations should eventually lead to a fix point $\mathcal{T}^N[H] \xrightarrow{N \rightarrow \infty} H^*$ such that $\mathcal{T}[H^*] = H^*$. In numerical simulations, N will only increase up to a value where H_N is close enough to the fix point H^* so that no new significant contributions to the Hamiltonian are obtained. For the purposes of this project, taking $N = 51$ will be enough for the NRG code to converge.

¹Let \mathcal{O} be a set of operators, then T is a contracting map if $\mathcal{T}[\mathcal{O}'] \subset \mathcal{O}'$ for every $\mathcal{O}' \subset \mathcal{O}$.


 Figure 5.3: . Energy interval discretization. Source: By the Author

In the 1970's G.Wilson used this theory to create the famous Numerical Renormalization Group (NRG) [33, 24, 34]. His main idea was to perform a logarithmic discretization of the conduction band in the lead as shown in Figure 5.3.(a). Taking into account that the leading contributions to the conductance occur at states close to the Fermi energy $\omega = 0$, we can define a cut-off ($|\omega| < D$) so that the rest at higher contributions are not relevant. Then we use D to rescale the energy interval. As you can observe in the figure, the QD is coupled to all these energy states at the same time. The logarithmic discretization gives more relevance to the low energy scales by assigning a different Hamiltonian coupling to each one of them. To complete this idea, the NRG code maps the Hamiltonian of the QD-lead system to the Wilson's chain shown in Figure 5.3(b). A detailed description of this map is included in the Appendix section A.1.

After these steps we obtain a chain Hamiltonian of the form

$$H = H_d + D \sum_{\sigma} \left[\sqrt{\frac{2\Gamma}{\pi D}} (d_{\sigma}^\dagger f_{0\sigma} + f_{0\sigma}^\dagger d_{\sigma}) + \frac{1}{2} (1 + \Lambda^{-1}) \sum_{n=0}^{\infty} \Lambda^{-\frac{n}{2}} \xi_n (f_{n\sigma}^\dagger f_{n+1,\sigma} + f_{n+1,\sigma}^\dagger f_{n\sigma}) \right]. \quad (5.23)$$

In the flat-band approximation the parameters ξ_n can be obtained analytically [33]

$$\xi_n = \frac{1 - \Lambda^{-n-1}}{(1 - \Lambda^{-2n-1})^{\frac{1}{2}} (1 - \Lambda^{-2n-3})^{\frac{1}{2}}}.$$

From equation (Equation A.12) we define the following set of Hamiltonians

$$H_{N+1} = T[H_N] = \Lambda^{-\frac{1}{2}} H_N + \xi_N \left(f_{N+1,\sigma}^\dagger f_{N,\sigma} + f_{N,\sigma}^\dagger f_{N+1,\sigma} \right), \quad (5.24)$$

with

$$H_{-1} := \frac{2H_d}{1 + \Lambda^{-1}}. \quad (5.25)$$

The Renormalization Group transformation \mathcal{T} can be defined as

$$\mathcal{T}^N H_{-1} = \frac{1 + \Lambda^{-1}}{2} \Lambda^{\frac{N-1}{2}} H_N$$

Note that in the limit $\xrightarrow{N \rightarrow \infty}$ we should recover the initial Anderson Hamiltonian. In addition, note that the leading coefficients of the contributions to each Hamiltonian H_N are given by

$$\Lambda^{\frac{-N}{2}} \xi_N \xrightarrow{N \rightarrow \infty} \frac{\Lambda^{\frac{-N}{2}} (1 - \Lambda^{-N})}{1 - \Lambda^{-2N}} \sim \frac{\Lambda^{\frac{-N}{2}}}{1 + \Lambda^{-N}},$$

which decays exponentially with the length of the chain. Therefore, we may think that at some point these new contributions will be so small that the map \mathcal{T} will eventually converge. Formally the theory regarding the NRG convergence is complex for this thesis. However the results show that the operator that truly converges is \mathcal{T}^2 and not \mathcal{T} [34]. This has important consequences, for instance the convergence of the code has to be analyzed on odd and even values of N separately.

To this point the expression (Equation A.12) and the derived limit of H_N to the Anderson Hamiltonian are exact. The first approximations arrive in the following step which include an iterative diagonalization of the Hamiltonian.

5.2.2 Iterative Diagonalization

This diagonalization starts with the impurity/dot Hamiltonian H_{-1} , which must be written in matrix form according to a defined basis. The other steps can be defined by induction. Suppose that the spectrum of H_N is diagonal on a given basis. Then the NRG code performs each of the following steps:

1. Rescaling the spectrum of H_N by $\Lambda^{\frac{1}{2}}$ as defined in Equation A.12. Figure 5.4 (a)→(b).
2. Adding the next step of the chain to form H_{N+1} and diagonalizing the new Hamiltonian such that $H_{N+1} = U_{N+1}^\dagger D_{N+1} U_{N+1}$. After this step, each of the eigenstates of H_N will split into up to 4 new energy states (probably degenerate) determined by the new coupling with the $N+1$ site basis $|0\rangle, |\uparrow\rangle, |\downarrow\rangle, |\uparrow\downarrow\rangle$. Figure 5.4 (b)→(c).
3. Shifting the spectrum by a certain dephase factor such that the 0 of energy is always the ground state. Figure 5.4 (c)→(d).

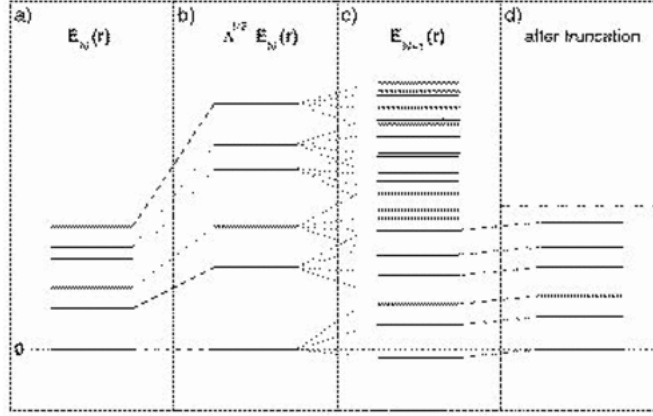


Figure 5.4: Iterative diagonalization process. [\[Source: \[24\]\]](#)

4. Numerical cutting: If the number of states in the system exceeds a definite number (1000 in this thesis) the exceeding higher energy states are neglected.². Figure 5.4 (c)→(d).
5. Rotating operators $f_{N,\sigma}$ by $U_N f_{N,\sigma} U_N^\dagger$ to start the next operation.

The final outcome of this operations will be the complete spectrum of the Anderson model at each energy level. However we still need to talk about an important speed-up to the code obtain when considering the symmetries of the system.

5.2.3 Symmetries

The symmetries of the initial Hamiltonian take a very important role in this iterative diagonalization. Lets suppose that the initial Hamiltonian H_d has certain symmetries classified by the quantum number S . Then H_d can be written can be represented in block Hamiltonians over a basis of the form $|S, i\rangle$. A diagnoziation process of an square matrix with L rows usually has an square order proportionate to the number of entries $\mathcal{O} \sim L^2$. However, if the matrix is organize in blocks of length N_j such that $\sum_j N_j = L$, then the order of diagonalization will be around $\sum_j N_j^2$ which is in general much smaller than $(\sum_j N_j)^2 L^2$. Therefor the block diagonalization provides important numerical advantages to the algorithm.

To keep this speed-up we must preserve this symmetry structure for the rest of the algorithm. For it, we first need to verify that the picked symmetry also commutes with the hopping terms in the chain Hamiltonian. If so, for each step N of the NRG algorithm we will have that the H_N Hamiltonian can be written in a block diagonal form with basis $|S_N, i_N\rangle$. Then it is necessary to

²This step must be performed carefully to preserve the symmetries of the system. If two states are entangled and one of them is eliminated and the other is not, the program could lead to misleading results. Further discussions to solve this problem are presented in the symmetry subsection.

define transition rules from the quantum numbers S_N to S_{N+1} . By doing this, we assure that the block architecture is transmitted through the entire algorithm, hence reducing the computational time significantly at each step of the NRG chain.

In the following subsection we will give examples of this symmetry propagation in the example a quantum dot attached to a metallic lead.

5.2.4 Iterative diagonalization in a single QD Hamiltonian

Now that we have an iterative representation of the Anderson Model Hamiltonian (Equation A.12), lets take a look to how the NRG code would work for a QD. We start with the dot Hamiltonian. (Since the D term is always present as a normalizing factor, we are going to avoid this term in future computations and suppose that we are working with unit-less variables ε_d , U and $\Gamma' := \sqrt{\frac{2\Gamma}{\pi D}}$).

$$H_d = \frac{1}{D} \left(\varepsilon_d + \frac{U}{2} \right) d_\sigma^\dagger d_\sigma + \frac{U}{2D} (d_\sigma^\dagger d_\sigma - 1)^2. \quad (5.26)$$

Now observe that hamiltonian Equation 5.26 already has a diagonal form in the base $\{| \uparrow\downarrow \rangle, | \uparrow \rangle, | \downarrow \rangle, | 0 \rangle\}$

$$H_d = \frac{1}{D} \begin{bmatrix} 2\varepsilon_d + \frac{3U}{2} & 0 & 0 & 0 \\ 0 & \varepsilon_d + \frac{U}{2} & 0 & 0 \\ 0 & 0 & \varepsilon_d + \frac{U}{2} & 0 \\ 0 & 0 & 0 & \frac{U}{2} \end{bmatrix}.$$

Lets define $H_{-1} = \Lambda^{\frac{-1}{2}} H_d$. Adding the first chain interaction to H_d we obtain a new Hamiltonian of the form

$$H_0 = \Lambda^{\frac{1}{2}} H_{-1} + \Gamma' \left(d_\sigma^\dagger f_{0\sigma} + f_{0\sigma}^\dagger d_\sigma \right). \quad (5.27)$$

The Hilbert space for this Hamiltonian has to be extended to include the 4 degrees of freedom of the $f_{0\sigma}^\dagger$ particles which are also given by $\{| \uparrow\downarrow \rangle, | \uparrow \rangle, | \downarrow \rangle, | 0 \rangle\}$. Therefore the total Hilbert space for H_0 is given by a base of the form

$$| s_1 \rangle | s_2 \rangle := | s_1 \rangle \otimes | s_2 \rangle \text{ with } | s_i \rangle \in \{| \uparrow\downarrow \rangle, | \uparrow \rangle, | \downarrow \rangle, | 0 \rangle\}.$$

We obtain an space of dimension $4 \times 4 = 16$. Now, before adventuring to write the Hamiltonian for H_0 as a 16×16 -matrix note that H_{-1} preserves particle number \mathcal{N} and the total spin S . We can associate each state to one of these symmetries as

$$|\uparrow\downarrow\rangle \longrightarrow |\mathcal{N} = 2, S = 0\rangle, |0\rangle \longrightarrow |\mathcal{N} = 0, S = 0\rangle \quad (5.28)$$

$$|\uparrow\rangle \longrightarrow |\mathcal{N} = 1, S = \frac{1}{2}\rangle, |0\rangle \longrightarrow |\mathcal{N} = 1, S = -\frac{1}{2}\rangle. \quad (5.29)$$

5.2. The Numerical Renormalization Group (NRG)

The propagation rule for the symmetry is defined with the following identity

$$|\mathcal{N}_1, S_1\rangle \otimes |\mathcal{N}_2, S_2\rangle \subset |\mathcal{N} + \mathcal{N}_2, S_1 + S_2\rangle \quad (5.30)$$

Then we can use \mathcal{N} and S as quantum numbers and generate the Hamiltonian H_0 in blocks. We will observe that the terms in the diagonal will correspond to the eigenvalues of H_{-1} for the first space. The non-diagonal terms are the result of the hopping interactions with the first site.

$$H_{\mathcal{N}=0, S=0} :$$

$$|0\rangle |0\rangle \rightarrow \left[\frac{U}{2} \right]$$

$$H_{\mathcal{N}=4, S=0} :$$

$$|\uparrow\downarrow\rangle |\uparrow\downarrow\rangle \rightarrow \left[2\epsilon_d + \frac{3U}{2} \right]$$

$$H_{\mathcal{N}=1, S=\frac{1}{2}} :$$

$$\begin{aligned} |\uparrow\rangle |0\rangle &\rightarrow \left[\begin{array}{cc} \epsilon_d + \frac{U}{2} & \Gamma' \\ \Gamma' & \frac{U}{2} \end{array} \right] \\ |0\rangle |\uparrow\rangle &\rightarrow \left[\begin{array}{cc} \epsilon_d + \frac{U}{2} & \Gamma' \\ \Gamma' & \frac{U}{2} \end{array} \right] \end{aligned}$$

$$H_{\mathcal{N}=1, S=-\frac{1}{2}} :$$

$$\begin{aligned} |\uparrow\rangle |0\rangle &\rightarrow \left[\begin{array}{cc} \epsilon_d + \frac{U}{2} & \Gamma' \\ \Gamma' & \frac{U}{2} \end{array} \right] \\ |0\rangle |\uparrow\rangle &\rightarrow \left[\begin{array}{cc} \epsilon_d + \frac{U}{2} & \Gamma' \\ \Gamma' & \frac{U}{2} \end{array} \right] \end{aligned}$$

$$H_{\mathcal{N}=2, S=-1} :$$

$$|\downarrow\rangle |\downarrow\rangle \rightarrow \left[\epsilon_d + \frac{U}{2} \right]$$

$$H_{\mathcal{N}=2, S=1} :$$

$$|\uparrow\rangle |\uparrow\rangle \rightarrow \left[\epsilon_d + \frac{U}{2} \right]$$

$$H_{\mathcal{N}=2, S=0} :$$

$$\begin{aligned} |\uparrow\downarrow\rangle |0\rangle &\rightarrow \left[\begin{array}{cccc} 2\epsilon_d + \frac{3U}{2} & \Gamma & -\Gamma & 0 \\ \Gamma & \epsilon_d + \frac{U}{2} & 0 & \Gamma \\ -\Gamma & 0 & \epsilon_d + \frac{U}{2} & -\Gamma \\ 0 & \Gamma & -\Gamma & \frac{U}{2} \end{array} \right] \\ |\uparrow\rangle |\downarrow\rangle &\rightarrow \left[\begin{array}{cccc} 2\epsilon_d + \frac{3U}{2} & \Gamma & -\Gamma & 0 \\ \Gamma & \epsilon_d + \frac{U}{2} & 0 & \Gamma \\ -\Gamma & 0 & \epsilon_d + \frac{U}{2} & -\Gamma \\ 0 & \Gamma & -\Gamma & \frac{U}{2} \end{array} \right] \\ |\downarrow\rangle |\uparrow\rangle &\rightarrow \left[\begin{array}{cccc} 2\epsilon_d + \frac{3U}{2} & \Gamma & -\Gamma & 0 \\ \Gamma & \epsilon_d + \frac{U}{2} & 0 & \Gamma \\ -\Gamma & 0 & \epsilon_d + \frac{U}{2} & -\Gamma \\ 0 & \Gamma & -\Gamma & \frac{U}{2} \end{array} \right] \\ |0\rangle |\uparrow\downarrow\rangle &\rightarrow \left[\begin{array}{cccc} 2\epsilon_d + \frac{3U}{2} & \Gamma & -\Gamma & 0 \\ \Gamma & \epsilon_d + \frac{U}{2} & 0 & \Gamma \\ -\Gamma & 0 & \epsilon_d + \frac{U}{2} & -\Gamma \\ 0 & \Gamma & -\Gamma & \frac{U}{2} \end{array} \right] \end{aligned}$$

$$H_{\mathcal{N}=3, S=\frac{1}{2}} :$$

$$\begin{aligned} |\uparrow\downarrow\rangle |\uparrow\rangle &\rightarrow \left[\begin{array}{cc} \epsilon_d + \frac{U}{2} & -\Gamma' \\ -\Gamma' & \frac{U}{2} \end{array} \right] \\ |\uparrow\rangle |\uparrow\downarrow\rangle &\rightarrow \left[\begin{array}{cc} \epsilon_d + \frac{U}{2} & -\Gamma' \\ -\Gamma' & \frac{U}{2} \end{array} \right] \end{aligned}$$

$$H_{\mathcal{N}=3, S=-\frac{1}{2}} :$$

$$\begin{aligned} |\uparrow\downarrow\rangle |\downarrow\rangle &\rightarrow \left[\begin{array}{cc} \epsilon_d + \frac{U}{2} & -\Gamma' \\ -\Gamma' & \frac{U}{2} \end{array} \right] \\ |\downarrow\rangle |\uparrow\downarrow\rangle &\rightarrow \left[\begin{array}{cc} \epsilon_d + \frac{U}{2} & -\Gamma' \\ -\Gamma' & \frac{U}{2} \end{array} \right] \end{aligned}$$

The next step would be to diagonalize H_0 by blocks $H_{\mathcal{N}, S}$ and then including the next place in the chain. The following Hamiltonians are generated in the same way from equation Equation 5.24. The symmetries of the new states can be obtained from the propagation rule Equation 5.30. When the number of states surpasses the 1000 states, the code will automatically cutoff the higher energy states. However it is important that a Block is not divided in this cutting, since it could break the preserved symmetry.

Finally, the spectrum for $\Lambda = 2.5$ takes the 'spaghetti' form in Figure 5.5. Before $N = 30$ low-energy contributions generate significant changes in the energy levels. The stable strum after the step $N = 30$ shows that the code has converged at this stage. As we previously declared, it is not \mathcal{T} but \mathcal{T}^2 the transformation that has fixed points, which explains why it was necessary to plot the even and the odd spectrum separately.

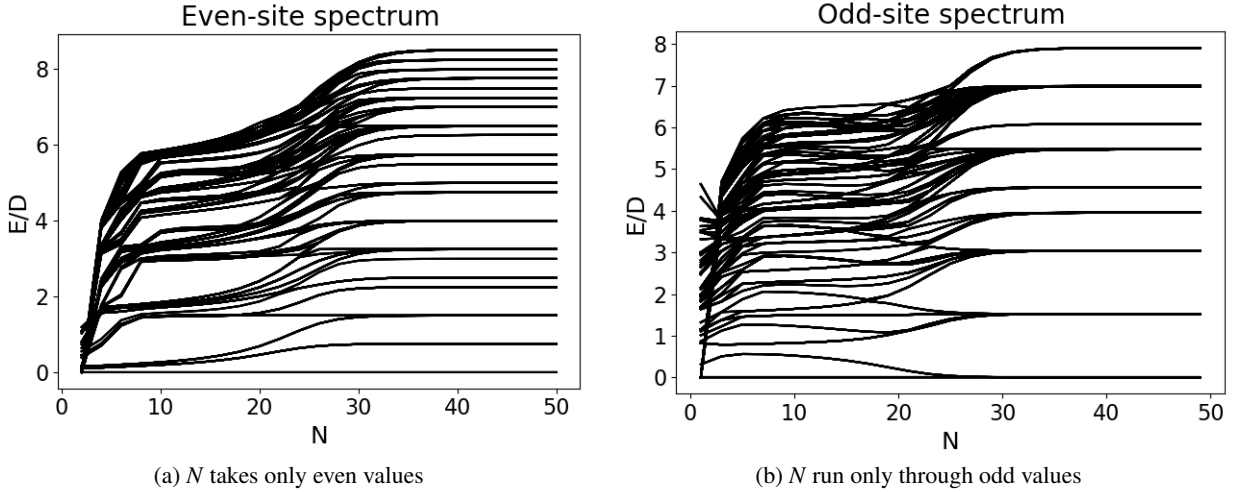


Figure 5.5: Evolution of the QD-spectrum vs number of iterations of the code for $U = 0.5$, $e_d = -0.25$, $\Gamma = 2.82 \times 10^{-2}$.

At the end of the NRG code, we obtain a complete list of the spectrum ($E_{i,N}$) and the eigenstates ($|i,N\rangle$) of the Hamiltonian at each step N of the chain (See Figure 5.5). It is important to keep all of these states since each one of them represents different thermodynamic regimes of the system. While the site $N = 1$ represents the physics of the system relevant at temperatures around $K_B D \Delta^{-1}$, the site $N = 30$ shows the low energy contributions at $T \sim K_B D \Delta^{-30}$ where the ground state is strongly correlated. Furthermore, the states at low temperatures are entangled with the higher energy states. We need to take this into account to extract dynamical quantities of the system, which is the objective of the following section.

5.2.5 The Density Matrix Renormalization Group (DM-NRG)

The NRG codes allows us to compute several thermodynamic quantities such as the entropy S , the free energy and the partition function $Z(\beta)$. In addition, we can compute the spin magnetization or dynamical quantities such the density of states, the magnetic susceptibility and the conductivity. To perform this we can use the spectrum obtained in the NRG code to define the Boltzman distribution of the system. Then we apply the usual methods of statistical mechanics.

In this thesis we will focus in computing the density of states at the impurity (QD). For this, let $|j\rangle$ and $|q\rangle$ label a base of eigenstates of the Hamiltonian H . Now recall the definition of the time-ordered green function Equation 5.7

$$G_{d,d^\dagger}(t) = \langle \mathbb{T} [d(t)d^\dagger(0)] \rangle \quad (5.31)$$

$$= \theta(t) \left\langle \left[e^{\frac{i}{\hbar} H t} d e^{-\frac{i}{\hbar} H t} d^\dagger \right] \right\rangle + \theta(-t) \left\langle \left[d^\dagger e^{\frac{i}{\hbar} H t} d e^{-\frac{i}{\hbar} H t} \right] \right\rangle \quad (5.32)$$

$$= \theta(t) \sum_{|j\rangle, |q\rangle} p_j \langle j | e^{\frac{i}{\hbar} H t} d | q \rangle \langle q | e^{-\frac{i}{\hbar} H t} d^\dagger | j \rangle + \theta(-t) \sum_{|j\rangle, |q\rangle} p_q \langle q | d^\dagger e^{\frac{i}{\hbar} H t} | j \rangle \langle j | d e^{-\frac{i}{\hbar} H t} | q \rangle \quad (5.33)$$

$$= \theta(t) \sum_{|j\rangle, |q\rangle} p_j e^{\frac{-i}{\hbar} t (E_j - E_q)} \| \langle j | d | q \rangle \|^2 + \theta(-t) \sum_{|j\rangle, |q\rangle} p_q e^{\frac{i}{\hbar} t (E_j - E_q)} \| \langle j | d | q \rangle \|^2 \quad (5.34)$$

Where $p_j := \frac{e^{-\beta E_j}}{Z(\beta)}$ defines the Boltzmann probability of the eigenstate $|j\rangle$ according to Hamiltonian H .

It is known that the Fourier transform of an expression of the form $e^{-ax}\theta(x)$ is $\frac{1}{\omega+is-a}$. Then the Green function in the frequency space is

$$G_{d,d^\dagger}(\omega) = \frac{1}{Z(\beta)} \sum_{|j\rangle, |q\rangle} \frac{e^{-\beta E_j} + e^{-\beta E_q}}{\omega + is - E_j + E_q} \| \langle j | d | q \rangle \|^2. \quad (5.35)$$

From the imaginary part of Equation 5.35 we obtain a formula for the spectral density in terms of the eigenstates and energies of the Hamiltonian

$$\rho_d = \frac{1}{Z(\beta)} \sum_{|j\rangle, |q\rangle} \left(e^{-\beta E_j} + e^{-\beta E_q} \right) \delta(\omega - E_j + E_q) \| \langle j | d | q \rangle \|^2. \quad (5.36)$$

This new expression for the DOS can be integrated to NRG code in different ways . A first method created by Costi *et al.* consisted in computing (Equation 5.36) with the eigenstates of each shell Hamiltonian H_N [35]. It is necessary to take into account that the operator $\langle j | d | q \rangle$ is constantly rotating after each diagonalization procedure generating different representation. Then, an important part of Costi's algorithm is to obtain these new representations of $\langle j | d | q \rangle_N$ recursively starting from an input representation $\langle j | d | q \rangle_{N=0}$.

Although Costi's method predicts accurately the DOS at low-energies, it fails to fit the high energy levels. The method that corrects this problem receives the name of Density Matrix Numerical Renormalization Group (DMNRG) [36]. The main idea of DMNRG is to include the entanglement corrections with the lower energy-states using the density matrix formalism. For this, Hofstetter defines the density matrix at the last shell Hamiltonian N_{max} $\hat{\rho}$ as the thermal mixed state

$$\hat{\rho}_{N_{max}} = \sum_j e^{-\beta E_j} |j\rangle_{N_{max}} \langle j|, \quad (5.37)$$

where the subindex N_{max} pinpoints that $|j\rangle_{N_{max}} \langle j|$ is an eigenstate of the last shell Hamiltonian $H_{N_{max}}$.

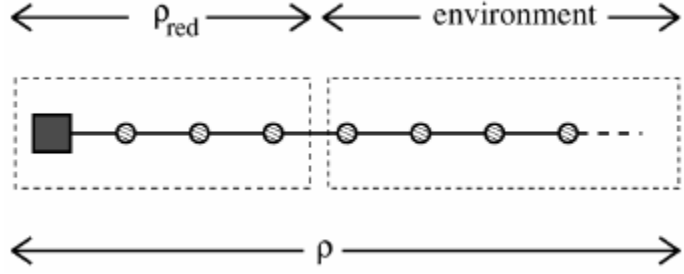


Figure 5.6: Wilson's chain depicted as an open quantum system.

With this new density matrix we could rewrite Equation 5.32 as

$$G_{d,d^\dagger}^{N_{max}}(t) = \text{Tr}(\hat{\rho}_{N_{max}} \mathbb{T}[\{d^\dagger, d\}]). \quad (5.38)$$

From the Green function $G_{d,d^\dagger}^{N_{max}}(t)$ we can obtain the density of states associated to the temperature $T_{N_{max}}$. Nevertheless, these results are not relevant at higher temperatures.

To solve this problem we may think Wilson's chain as an open quantum system where the reservoir are the low-energy sites of the chain and the system contains the high energy site including the impurity/QD as observed in Figure 5.6. Using this analogy it is possible we can readily obtain the density matrix ρ_s by taking the partial trace over the reservoir

$$\rho_s = \text{Tr}_R[\rho_{N_{max}}]. \quad (5.39)$$

The DM-NRG code applies recursively this idea to obtain the density matrix corresponding to each scale of temperature T_N . It starts from $\rho_{N_{max}}$ defined at (Equation 5.37) and obtains $\rho_{N_{max}-1}$ by taking the partial trace over the vector space corresponding to the last site of the chain

$$\rho_{N_{max}-1} = \text{Tr}_{N_{max}}[\rho_{N_{max}}]. \quad (5.40)$$

The other density matrices are computed by induction as

$$\rho_{N-1} = \text{Tr}_N[\rho_N], \quad (5.41)$$

and the density of states at each temperature regime can be computed at each stage from the green function

$$G_{d,d^\dagger}^N(t) = \text{Tr}(\hat{\rho}_N \mathbb{T}[\{d^\dagger, d\}]). \quad (5.42)$$

The DM-NRG algorithm produces significantly better results at high energies than Costi's initial idea. Indeed, DM-NRG is still one of the best methods to compute dynamic quantities of an impurity system. In the following subsection we will some details of how DM-NRG is integrated with the NRG code.

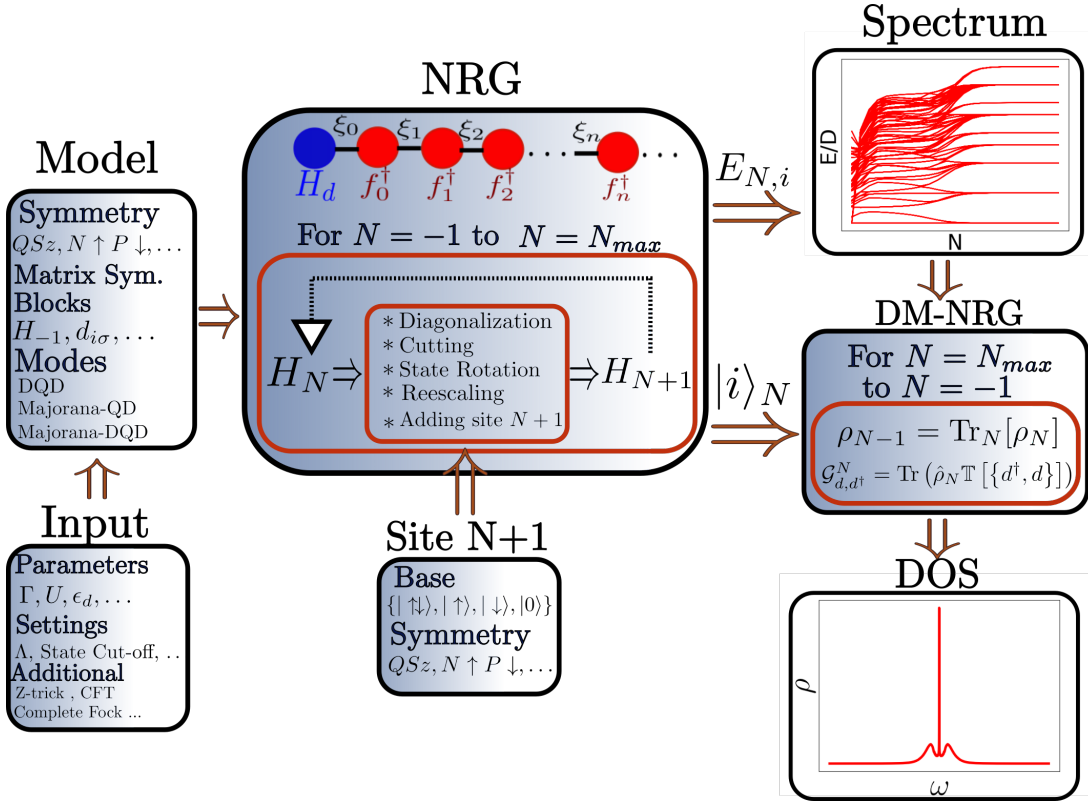


Figure 5.7: Diagram of the NRG code

5.2.6 Specifications of the NRG Code

The NRG code used in this thesis was implemented by my thesis advisor Luis Gregorio Dias during his posdoc at the University of Ohio. The general scheme is shown in Figure 5.7. It incorporates different stages in order to complete the procedure described in this classes. Here we give a brief description of each step:

- **Model:** The model defines the type of impurity that we are going to study. It could be a single QD or more complex structures such as a DQD or a Majorana-QD system. My main contribution to this code was at this stage by designing the mode DQD-Majorana, which describes a DQD coupled to a Majorana zero mode. These models preserve different symmetries. In the single dot Hamiltonian presented in subsection 5.2.4 we used the symmetry $\mathcal{N}S_z$, which is equivalent to charge-spin QS_z . However we will find that Majorana systems require another symmetry-type that we call as $N \uparrow P \downarrow$. The model is defined by initial Hamiltonian H_{-1} and the annihilation operators $d_{i\sigma}$ which must be submitted in the code written in the block symmetry representation described in subsection 5.2.3.

- **Input:** The input is a .dat file that attributes a numerical value to each parameter of the model. In addition, it allows to set different code specifications as the number of iterations N_{max} , the scaling parameter Λ and the maximum number of states before the cut-off. It is also possible to include additional implementations to improve the results of the NRG code such as the Z-trick [37] and the Complete Fock State. In this project, we only used the Z-trick, which significantly improves the spectral resolution at high energies.
- **NRG-Main:** This part of the code mainly integrates the ideas of subsection 5.2.1 and implements the iterative diagonalization described in subsection 5.2.2. Each shell Hamiltonian H_n is diagonalized. The high-energy eigenstates are cut-off if they exceed the limit. Then the states are rotated and the eigenvalues are rescaled to include the next step of the Wilson's chain. The symmetry block structure is preserved during the entire loop. NRG produces as output a detailed evolution of the spectrum which produces the spaghetti form. In addition, it can print the states and operators that are necessary to start other instances of the code like DM-NRG.
- **Site $N + 1$:** This is a small class that creates another site of the chain in the base $\{|\uparrow\downarrow\rangle, |\uparrow\rangle, |\downarrow\rangle, |0\rangle\}$. This base must be rewritten according to the symmetry quantum number to couple it with the matrices at the NRG code.
- **DM-NRG:** As described in subsection 5.2.5, this code generates iteratively the density matrix associated to each energy scale. Then it computes the green function and the density of states. The DOS of the single QD model is an example of its outputs. The plot shows the characteristic Kondo peak at the Fermi energy in the middle of the Coulomb peaks describing the energy states.

This NRG code was previously implemented in C++. It can be cloned from the Github link <https://git.io/fh9cM>. To optimize the performance of NRG, the code uses the packages Boost, LAPACK and Gnu Scientific Library (GSL), which provide a rapid interface for numerical matrix diagonalization.

5.2.7 NRG results in a Double Quantum Dot Coupled to a Metallic Lead

We now intend to observe the results of this code applied to the model double quantum dot attached to a metallic lead. The Hamiltonian for this system is the Anderson model with the impurity given by the interacting version of Hamiltonian Equation 5.11

$$H_{DQD} = \sum_{i=1}^2 \sum_{\sigma} \left(\epsilon_i + \frac{U_i}{2} \right) d_{i\sigma}^\dagger d_{i\sigma} + \left(\sum_{i\sigma} d_{i\sigma}^\dagger d_{i\sigma} - 1 \right)^2 + \sum_{\sigma} t_{dots} d_{1\sigma}^\dagger d_{2\sigma} + t_{dots}^* d_{2\sigma}^\dagger d_{1\sigma} \quad (5.43)$$

The Hilbert space of this system has 16-dimensions and the symmetries in this Hamiltonian are exactly the same than the ones in the single QD case \mathcal{NS} . Nevertheless, we decided to use

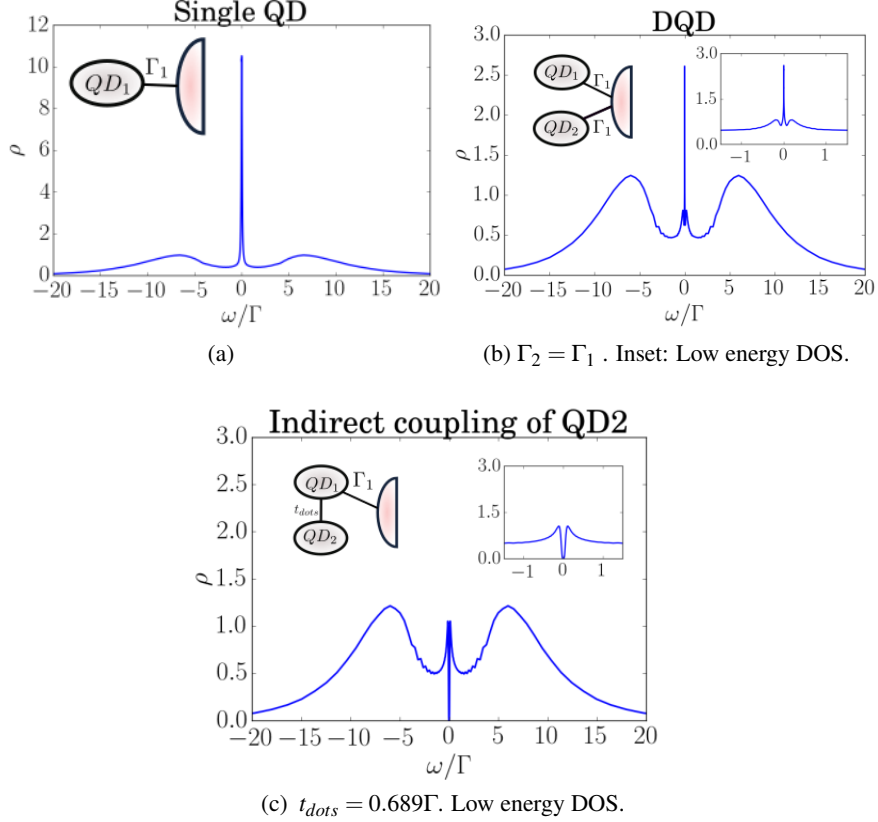


Figure 5.8: Density of states in QD1 predicted by NRG at each case. The insets show the. Note that figure a) is in a different scale due to a major central peak ..

Source: *By the Author*

the DQD-Majorana mode to simulate this system. By setting the Majorana couplings to $t_1 = t_2 = 0$ we can decouple the Majorana mode, hence obtaining the DQD model (See chapter 7). The results we obtained are in agreement with previous previous works [22], which was an important test to confirm the veracity of this new mode.

For the entire thesis we will fix the value of the coulomb repulsion parameters to

$$U_1 = U_2 = 17.7305\Gamma_1. \quad (5.44)$$

We picked these parameters considerably higher than the broadening unit Γ_1 to guarantee the appearance of Kondo physics which is caused by these strong correlations.

NRG-code We used the same configurations from Figure 5.2.

The single QD attached to a metallic lead is a particular case of the double quantum dot model, where the second dot is not attached $\Gamma_2 = t_{dots} = 0$. Figure 5.8 shows the NRG results

for this case. The three plots show the external Coulomb peaks at $e_1 = \frac{U}{2} \sim 8.62\Gamma_1$, which represent the DOS of the energy levels. In addition Figure 5.8a shows a central peak at the Fermi energy. **This is the Kondo Peak.**

In Figure 5.8b we observe the DOS when the two QDs are symmetrically attached. At low energies, the inset shows the appearance of two satellite peaks representing the Ruderman-Kittel-Kasuya-Yosida (RKKY) interaction. This is an anti-ferromagnetic coupling that appears in the interacting case due to the strong correlations between both dots. A detailed explanation of the appearance of these new states is included in section Appendix B.

The most interesting case is in Figure 5.8c. As we already observed in the non-interacting case, the interference with the second dot completely destroys the Kondo peak. This effect is observed at low energies closed to $t_{dots} = 0.689\Gamma$. The paper describing this result was a central part of one of my advisor's project. This result encouraged me to formulate the following question. What happens if we attached a Majorana mode to one of these dots?. Would it be destroyed by interference or it will survive to it. Answering this question is one of the main objectives of chapter chapter 7.

Chapter 6

Motivation: The Pursuit of Majorana Fermions

"It started out with a toy model demonstration, and then I realized it was very good model. You don't understand the full implications until other people start thinking it is true and they observe the big picture [...] Now, that toy model is like Hydrogen atom for topological materials- it turned out to be the first example of topological quantum matter."

– F. Duncan M. Haldane

The Majorana Fermions, so called in the name of the Italian physicist Ettore Majorana, were first proposed as the real solution of the Dirac equation. The real field that solves this equation describes a fermion which is its own antiparticle, thus it has no electric charge nor mass. Till these days, no fundamental particle with these characteristics has been observed. However, the last decade has been full of excitement as new Majorana quasi-particles have been observed at the edges of topological superconductors.

The topological superconductors, belong to an emergent group of materials that experience phase transitions without passing through a symmetry breaking, hence they cannot be characterized by Landau theory. Instead, these phases of matter are described by a new type of order determined by the topology of the Brilloin zone. In mathematics, topology is used to describe non-local features of surfaces (or manifolds) that are preserved under smooth deformations. The cliché, but always educative, joke to explain this concept says that "Topologist cannot tell the difference between a donut and a coffee cup, since one of them can always be continuously de-



Figure 6.1: Coffe-donut: adiabatic evolution

formed into the other through a sequence of smooth, small alterations" (Figure 6.1).³ However it wouldn't be possible to deform soccer ball into a donut since no there is no way of making 'softly' a hole into the ball.

The insight of topology into the field of condensed matter physics is that those materials that are attributed a topological characterization are endowed with a characteristic stability under smooth deformations (adiabatic evolutions) . The most famous example of this behavior is the integer quantum hall effect (IQHE) whose robust conductivity platoes representing different topological phases allowed to define with high precision a resistivity standard unit $R_K = \frac{h}{e^2} = 25812.807557(18)\Omega$, hence having major impact in science and technology.

In the last two decades, a new type promising topological material has captivated the attention of many physicists. This is the Majorana wire, inspired in a famous Kitaev's toy model representing a spinless p-wave superconducting chain [1]. Under certain conditions, the Majorana wires experience topological phase transition characterized by the emergence of zero-modes localized at edges of the wire. Kitaev associated these modes with Majorana quasi-particles appearing at the boundary of the topological superconducting wires . Just like the IQHE, topology protects these Majorana's from quantum decoherence. In addition, Kitaev proposed that Majorana's non-abelian statistics provided a suitable method to encode quantum information [9]. These two characteristics gave the origin of an entire field called topological quantum computation [38].

The promise of using Majorana quasi-particles to implement quantum architectures motivated the pursuit of Majorana fermions during the following years. This motived a huge bunch of theoretical projects devoted to propose real implementations of the Kitaev model [2, 3, 39, 40? , 41]. The first experiment confirming the observation of Majorana zero modes (MZM) in topological superconductors was performed in 2012 by Mourik et al.. Since that moment, many other groups have created Majorana chains [14, 15, 42, 7, 43] These good experimental results inspired other ways to detect Majorana signatures. One of the most famous is the idea of coupling Majorana wires with QD's [4], which opened new lights to the design of quantum architectures with Majorana chains [44, 45].

In this chapter we will present a review of the main ideas behind the Kitaev chain (section section 6.1) and how that model inspired real implementations of Majorana wires section 6.2. In subsection 6.3.2 we will take a look to the idea of coupling QDs to a Majorana chain. This will be our last step before going into the main objective of this thesis: The manipulation of Majorana zero modes inside a double quantum dot.

6.1 The Kitaev Chain

Kitaev's tight binding toy model represents a finite *p*-wave superconducting wire with the following Hamiltonian

³For decades, this has been the mean reason for the absence of donuts at topology workshops.

6.1. The Kitaev Chain

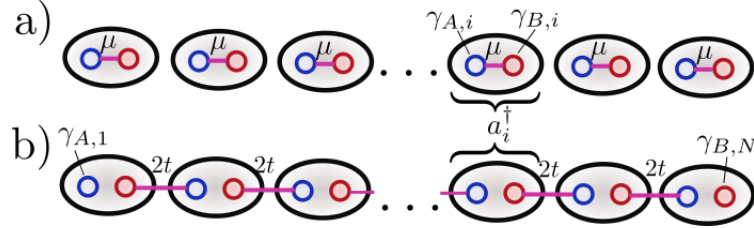


Figure 6.2: Illustration of the Kitaev chain for open boundary conditions in the Majorana representation. a)Represents the trivial case where the hopping and the superconducting term approaches to 0. b) The non-trivial topological phase. The coupling is produced between Majoranas in different Dirac fermions

Source: By the author

$$H = \sum_{i=1}^N \left[-t(a_i^\dagger a_{i+1} + a_{i+1}^\dagger a_i) - \mu a_i^\dagger a_i + \Delta a_i a_{i+1} + \Delta^* a_{i+1}^\dagger a_i^\dagger \right]. \quad (6.1)$$

Where μ is the chemical potential, so that $\mu a_i^\dagger a_i$ is the energy associated to each step in the chain. $t(a_i^\dagger a_{i+1} + a_{i+1}^\dagger a_i)$ represents the interaction between neighboring sites which is determined by the hopping term t . The remaining terms describe the superconducting properties of the system as is established by the BCS theory of superconductivity. Δ is a complex superconducting parameter with the form $\Delta = e^{i\theta} |\Delta|$. The associated terms represent the Cooper pairs which can be created or annihilated at neighboring sites of the system hence breaking particle number. However, the system still preserves parity, a property that will be very important during the rest of the project.

The form of Hamiltonian (Equation 6.1) favors the possibility of introducing new operators $\gamma_{A,j}$ and $\gamma_{B,j}$ such that

$$\gamma_{A,j} = e^{i\theta/2} a_j + e^{-i\theta/2} a_j^\dagger, \quad \gamma_{B,j} = -i(e^{i\theta/2} a_j - e^{-i\theta/2} a_j^\dagger). \quad (6.2)$$

It is simple check that these operators are self-adjoint ($\gamma_{A,j}^\dagger = \gamma_{A,j}$, $\gamma_{B,j}^\dagger = \gamma_{B,j}$). This is a required constraint for the Majorana particles. In addition they satisfy the fermionic anti-commutation relations

$$\begin{aligned} \{\gamma_{A,i}, \gamma_{A,j}\} &= \{\gamma_{B,i}, \gamma_{B,j}\} = 2\delta_{ij}, \\ \{\gamma_{A,i}, \gamma_{B,j}\} &= 0. \end{aligned} \quad (6.3)$$

This allows us to understand the operators $\gamma_{A,i}, \gamma_{B,i}$ as Majorana fermions. If we also take the inverse of Equation 6.2 we obtain that each (Dirac) fermion in Hamiltonian (Equation 6.1) is composed by two Majorana fermions such that

$$a_j = \frac{e^{-i\theta/2}}{2} (\gamma_{A,j} + i\gamma_{B,j})$$

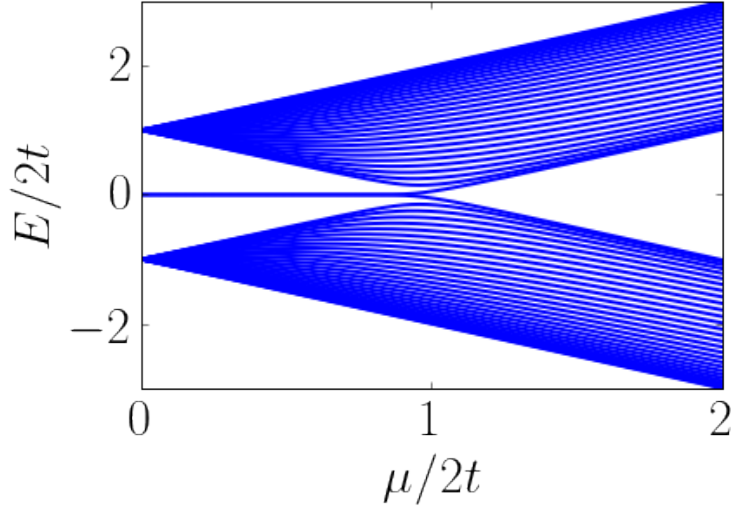


Figure 6.3: Spectrum of Hamiltonian Equation 6.4 with 30 sites and $t = |\Delta|$ s. Method: Numerical diagonalization.

Source: By the author

We could even adventure to say that these Majorana operators are actually dividing the Dirac fermions into real(γ_A) and imaginary (γ_B) part ,the same way as complex numbers are a composite of two real numbers.

The new Kitaev Hamiltonian in the Majorana representation looks like

$$H = \frac{i}{2} \sum_{j=1}^N [-\mu \gamma_{A,j} \gamma_{B,j} + (t + |\Delta|) \gamma_{B,j} \gamma_{A,j+1} + (t - |\Delta|) \gamma_{A,j} \gamma_{B,j+1}] + \text{Const}, \quad (6.4)$$

Depending on the values of parameters μ, t and $|\Delta|$ we can identify two regimes represented by the following situations:

1. If $|\Delta| = t = 0$ and $\mu < 0$, Hamiltonian (Equation 6.4) becomes $\frac{-i\mu}{2} \sum_j \gamma_{A,j} \gamma_{B,j}$ which represents the coupling of the Majoranas in the same Dirac fermion. (See Figure 6.2 (a))
2. If $|\Delta| = t > 0$ and $\mu = 0$, the situation is much more interesting. The Hamiltonian (Equation 6.4) takes the form $H = 2ti \sum_j \gamma_{B,j} \gamma_{A,j+1}$. This implies that the coupling is performed between Majoranas of different Dirac fermions leaving the edge Majorana operators ($\gamma_{A,1}$ and $\gamma_{B,N}$) uncoupled (See Figure 6.2b)). Note that these uncoupled Majorana fermions can be at any state without any repercussion in the energy of the system. This explains the emergence of a ground state localized at edges of the chain.

These two situations are representatives of two different phases. The trivial phase occurs

6.1. The Kitaev Chain

for $\frac{\mu}{2t} > 1$ and the non-trivial phase appears when $\frac{\mu}{2t} < 1$ (See Figure 6.3). The mean characteristic of the non-trivial phase is the creation of an stable zero-mode generated by the uncoupled Majorana fermions at the edges of the Kitaev chain. Note that if

$$H = 2ti \sum_j \gamma_{B,j} \gamma_{A,j+1}, \quad (6.5)$$

it is possible to define new Dirac fermion operators as

$$c_j = \frac{1}{\sqrt{2}} (\gamma_{B,j} + i\gamma_{A,j+1}), \quad c_j^\dagger = \frac{1}{\sqrt{2}} (\gamma_{B,j} - i\gamma_{A,j+1}).$$

Then (Equation 6.6) becomes

$$H = ti \sum_{j=1}^{N-1} (2c_j^\dagger c_j - 1). \quad (6.6)$$

Then a ground state $|\Omega\rangle$ of this Hamiltonian is an state vacuum at all sites j from 1 to $N-1$ ($c_j|\Omega\rangle = 0$). This condition allows some degeneracy since the sites at the boundary are not coupled to the Hamiltonian $\gamma_{A,1}$ and $\gamma_{B,N}$. The Dirac operators formed by these Majoranas

$$c_N = \frac{1}{\sqrt{2}} (\gamma_{B,N} + i\gamma_{A,1}), \quad c_N^\dagger = \frac{1}{\sqrt{2}} (\gamma_{B,N} - i\gamma_{A,1}),$$

can be either occupied ($c_N^\dagger c_N |\Omega\rangle = 1$) or empty ($c_N^\dagger c_N |\Omega\rangle = 0$). Each of these results will have a different parity that is a preserved symmetry of our Hamiltonian. Indeed we can define a global parity operator as

$$\mathcal{P} = \prod_{i=1}^N (c_i^\dagger c_i - 1) = \prod_{i=1}^N -i\gamma_{B,i} \gamma_{A,i+1} = \pm 1. \quad (6.7)$$

In the ground state $|\Omega\rangle$, this parity will be defined by the result of $\gamma_{B,N} \gamma_{A,1}$ since the other states are fix. This is a very important point, since this symmetry protection is actually correlating the two opposite sites of the Kitaev chain i.e. Any attempt to disturb one site of the chain would have to change something on the other site, since the parity of the system must be preserved. This is a great deal, actually, it means that the coherence of Majorana fermions is actually very high. Why?. Then answer is topology and will be the objective of the next subsection.

6.1.1 Topological phase transition

The two regimes described previously can be characterized with a topological parameter. One of the methods for this is following the idea used by Alicea[3]. The first part is to suppose that we have an infinite chain ($N = \infty$) in Hamiltonian (Equation 6.4). The new system is translation

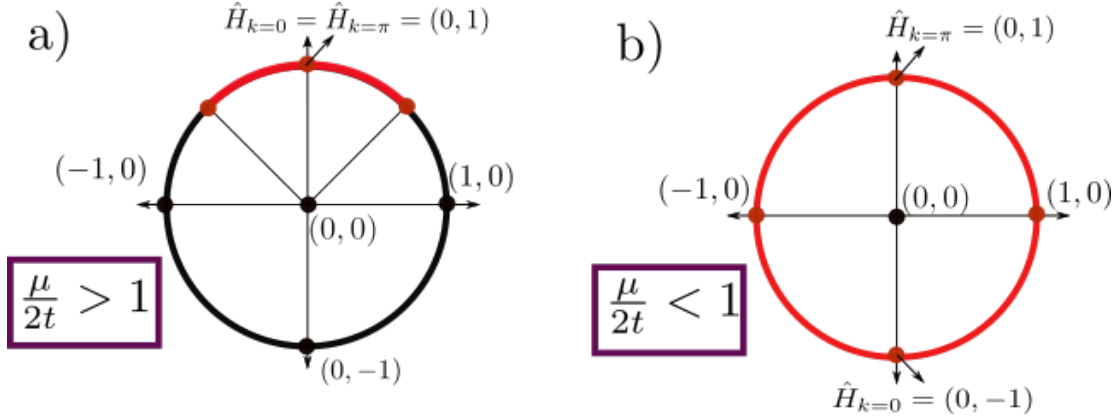


Figure 6.4: The following represents the path of \hat{H}_k for the interval $[-\pi, \pi]$. a) Corresponds to the trivial phase. The resulting path can be homotopically deformed to a point. b) The non-trivial phase corresponds to a non-contractible loop around the unitary circle.

Source: By the author

invariant, hence we can make a transformation to the momentum space. Then we may rewrite Hamiltonian (Equation 6.4) as

$$H = \sum_{k \in BZ} (b'_k \ c'_k) H_k \begin{pmatrix} b'_{-k} \\ c'_{-k} \end{pmatrix}, \quad (6.8)$$

with the Bloch Hamiltonian equal to

$$H_k = \begin{pmatrix} 0 & \frac{-i\mu}{2} + it \cos k + |\Delta| \sin k \\ \frac{i\mu}{2} - it \cos k + |\Delta| \sin k & 0 \end{pmatrix} = (|\Delta| \sin k) \sigma_x + \left(\frac{\mu}{2} - t \cos k \right) \sigma_y. \quad (6.9)$$

Here, σ_x and σ_y are the corresponding Pauli matrices. The Brillouin zone (BZ) is the periodic space $[-\pi, \pi]$ which can be mapped to the unitary circle. Equation (Equation 6.9) determines the coordinates of the Bloch Hamiltonian in the base $\{\sigma_x, \sigma_y\}$.

We can map these coordinates to the unitary circle by taking the norm of this vector giving

$$\hat{H}_k = \frac{1}{\sqrt{|\Delta|^2 \sin^2 k + (\frac{\mu}{2} - t \cos k)^2}} \begin{pmatrix} |\Delta| \sin k \\ \frac{\mu}{2} - t \cos k \end{pmatrix}. \quad (6.10)$$

Note that $|\Delta|^2 \sin^2 k + (\frac{\mu}{2} - t \cos k)^2 \neq 0$ for all the values of k as long as $\frac{\mu}{2t} \neq 1$. When $\frac{\mu}{2t} = 1$ the $H_{k=0} = 0$, so it cannot be normalized. **This is the same point were the phase transition**

occurs!. At any other value of $\frac{\mu}{2t}$ it is possible to normalize H_k for all values of $k \in BZ$. The result of mapping \hat{H}_k for all k is a path around the unitary circle.

This path can take two forms as we can observe in Figure subsection 6.1.1. If $\frac{\mu}{2t} > 1$ the path reduced to a line in the upward part of the circle. In the non-trivial phase $\frac{\mu}{2t} < 1$ the path completes the round to the entire circle. Note that this method states a topological difference between the two phases. While the path described by the trivial phase can be contracted to a single dot, the path described by the non-trivial one is a circle that cannot be contracted.

Note that to determine whether path of a given phase is of type a) or type b) we only need to check if $\hat{H}_{k=0}$ and $\hat{H}_{k=\pi}$ are the same point or opposite points. This transforms into a simple equation

$$\hat{H}_{k=0,y}\hat{H}_{k=\pi,y} = \begin{cases} 1 & \text{trivial phase} \\ -1 & \text{non-trivial phase} \end{cases} \quad (6.11)$$

where $\hat{H}_{k=0,y}$ is the y -th component of \hat{H}_k . The term $\hat{H}_{k,y}$ is a particular case of the Pfaffian $\mathcal{P}(k)$, which widely used as topological order in phase transitions involving Majorana fermions.

The mean idea behind this topological characterization relies in the adiabatic theorem. In simple words, the adiabatic theorem says that a slow evolution of a gaped Hamiltonian will produce a smooth evolution of its ordered eigenstates. i.g The order of the eigenstates remains unchanged.

A keyword in the previous definition is "gaped". As we can observe in Figure 6.3 the phase transition occurs at $\frac{\mu}{2t} = 1$. This point is where the gap of the Hamiltonian closes. In periodic boundary conditions no Majorana zero modes will emerge since there are no edges in the system. Therefore, the states with zero energy for $\frac{\mu}{2t} < 1$ will not appear at this situation. We obtain that the gapless point $\frac{\mu}{2t} = 1$ divides two gapped regions. If we are to follow the adiabatic theorem, these two regions must be separated, hence meaning that no adiabatic evolution could lead from one region to the other since that would involve crossing through a gapless region where state exchange is allowed.

To summarize, gapless points are forbidden points of our Hamiltonians in the middle of an adiabatic evolution. This forbidden points can be thought as "holes" in the space of Hamiltonians, which generates spaces with non-trivial topologies. Since adiabatic evolutions can be understood as smooth evolutions of the Hamiltonian, the relation with topology is clear. Then characterizing the phase transitions in the Kitaev chain, as in similar robust materials, is mainly a topological problem. Therefore, phase transitions can be characterized by topological quantities such as Pfaffians, Chern numbers or Winding numbers, which are always integer values.

This brings an interesting question. If we have two connected topological materials, one characterized by the number 0 and the other by the number 1, then what should happen at the surface?. Indeed something very exciting happens at these boundaries and those are the edge states, Majorana fermions, and all interesting topological phenomena in condensed matter.

Finally, note that in a system that preserve symmetries, the space of Hamiltonians has more forbidden sites. Therefore, these systems have a different topological characterization and more

importantly, topology protects these symmetries. This is the case of the Kitaev chain where the topological phase protects the parity of the symmetry under perturbations involving the two opposed Majoranas at the edges. This endowed topological stability combined with Majorana's non-abelian statistics (next subsection) makes the Kitaev chain a promising platform for quantum computation.

6.1.2 Non-abelian statistics

Imagine that we want to exchange two Majorana fermions γ_1 and γ_2 ⁴. This procedure can be performed with an adiabatic evolution of the Hamiltonian $H(t)$ that exchanges both operators while leaving the system invariant. Therefore, after a period T we require that

$$\begin{aligned}\gamma_1(T) &= \gamma_2(0) \\ \gamma_2(T) &= \gamma_1(0)\end{aligned}\tag{6.12}$$

while $(H(0) = H(T))$.

The adiabatic evolution is then represented by a unitary operator $U(t) = e^{-\frac{i}{\hbar} \int H(t)}$ and is applied according to Heisenberg's picture as

$$\gamma_i(T) = U^\dagger(t) \gamma_i(0) U(t).$$

Since Majoranas preserve fermion parity, H must commute with the parity operator $P = -i\gamma_1\gamma_2$. In a Clifford algebra generated by the operators γ_1 and γ_2 (See algebraic relations (Equation 6.3)), $[H, \gamma_1\gamma_2] = 0$ implies that $H(t) \propto \gamma_1\gamma_2$ or $H(t)$ is a constant. Taking the non-trivial answer we obtain that the evolution operator has the form $U(t) = e^{\alpha(t)\gamma_1\gamma_2}$, where $\alpha(t)$ is a complex function over t . We can simplify this exponential noting that $(\gamma_1\gamma_2)^2 = -1$ which after Taylor expansion reduces to

$$U(t) = \cos(\alpha(t)) - \gamma_1\gamma_2 \sin(\alpha(t)).\tag{6.13}$$

Replacing this solution in (Equation 6.12) we obtain

$$\begin{aligned}\gamma_1(T) &= \gamma_1 \cos(2\alpha(T)) - \gamma_2 \sin(2\alpha(T)) = \gamma_2 \\ \gamma_2(T) &= \gamma_2 \cos(2\alpha(T)) + \gamma_1 \sin(2\alpha(T)) = \gamma_1,\end{aligned}\tag{6.14}$$

which can only happen if $\alpha(T) = \pm\frac{\pi}{4}$. Hence we conclude that the exchange operator between both Majoranas is

$$U_{12} = e^{\pm\frac{\pi}{4}\gamma_1\gamma_2} = \frac{1}{\sqrt{2}}(1 \pm \gamma_1\gamma_2).\tag{6.15}$$

Note that this exchange does not depend on the evolution, nor the period of time.

Now imagine that we have three Majoranas γ_1, γ_2 and γ_3 and we want to perform the following processes. On the first one, we exchange Majoranas 1 and 2 and then the Majorana in

⁴This section is inspired on the page topocondmat https://topocondmat.org/w2_majorana/braiding.html, which contains an amazing tutorial about Majorana fermions and topological insulators.

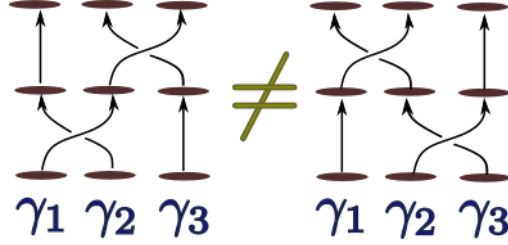


Figure 6.5: Representation of non-abelian braiding .

2 (which was initially at 1) is exchanged with Majorana 3 (Figure 6.5[Left]). On the second process, we invert the order, hence exchanging first exchange Majoranas 2 and 3 and then Majoranas 1 and 2 (Figure 6.5[Right]). These two cases are represented by the following operators respectively

$$\begin{aligned} U_{23}U_{12} &= \frac{1}{2}(1 + \gamma_2\gamma_3)(1 + \gamma_1\gamma_2) = \frac{1}{2}(1 + \gamma_2\gamma_3 + \gamma_1\gamma_2 + \gamma_3\gamma_1) \\ U_{12}U_{23} &= \frac{1}{2}(1 + \gamma_1\gamma_2)(1 + \gamma_2\gamma_3) = \frac{1}{2}(1 + \gamma_1\gamma_2 + \gamma_2\gamma_3 + \gamma_1\gamma_3). \end{aligned} \quad (6.16)$$

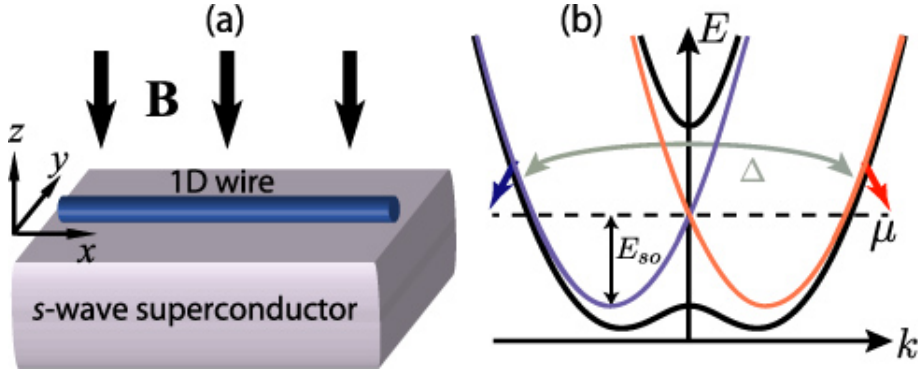
Since $\gamma_3\gamma_1 = -\gamma_1\gamma_3$, the outcome of both processes is essentially different, which means that it actually matters the order in which the Majoranas are exchanged .

The particles that satisfy this strange property receive the name of non-abelian anyons. While the word "anyon" usually integrates several types of particles including bosons and fermions, the word non-abelian emphasis on the non-commutative exchange statistics.

Non-abelian statistics is what make anyons a fantastic candidate to implement quantum algorithms. The idea of exchanging anyons can be thought as a braiding like in Figure 6.5. Since the order of braiding matters, different braiding orders can be associated to distinct algorithms. This generates another form of codifying information which has been extendedly studied in knot theory [46]. And if these anyons where topological, they will be protected from quantum decoherence [47]. To the date, the closest candidates to satisfy both properties (non-abelian statistics, topological characterization) are the Majorana fermions. Notwithstanding, the basic braiding protocol that would unleash the keys to topological quantum computation [38] has not been measured yet. Many theoretical proposals have been set up in this direction, but there is still a long experimental road.

6.2 Real implementations of the Kitaev Chain

One of the main problems to implement real devices capable to exhibit Majorana quasi-particles at the boundaries, was that Majorana's are spin-less. Since all materials have fermion doubling, it was necessary to endow the system with a physical property that could separate the spin energy bands. To bypass this problem, Lutchyn et al. proposed using a material with strong


 Figure 6.6: Source: [3]

spin-orbit Rashba interaction [48], which would split the energy band by spin, hence destroying fermion doubling.

This idea allowed scientist to designed the first Majorana wires. The recipe consists ingrowing a semi-conducting wire with high spin-orbit coupling, over an s'wave superconductor and inducing a Zeeman magnetic field (Figure 6.6(a)). Such model is described by the following Hamiltonian [3](65)

$$H = \int dx \psi^\dagger \left(\frac{-1}{2m} \partial_x^2 - \mu - i\alpha \sigma_y \partial_x + h \sigma_x \right) \psi + \Delta \psi_\downarrow \psi_\uparrow + \Delta^* \psi_\downarrow \psi_\uparrow, \quad (6.17)$$

where μ is the chemical potential, h is the Zeeman splitting energy, Δ is the superconducting gap and $\alpha > 0$ is the Rashba spin-coupling parameter, favoring spin-align. If $\Delta = 0$, the band structure would split and divide in two bands [3](67)

$$\epsilon_\pm(k) = \frac{k^2}{2m} - \mu \pm \sqrt{(\alpha k)^2 + h^2} \quad (6.18)$$

with opposed spins as observed in the blue and red lines of Figure 6.6(b).

The superconducting proximity effect opens a gap Δ that projects the upper and lower bands forming as observe in the black bands of Figure 6.6(b) . The separation of both energy channels allow us to think the conduction band as an spin-less system where Majorana modes can emerge. As pointed out by Alicea, the system is in the topological phase if the the following criterion is satisfied

$$h > \sqrt{\Delta^2 + \mu^2}. \quad (6.19)$$

This theoretical proposal led in 2012 to the first observation of Majorana signatures in InSb nanowires ⁵, by Mourik et al. from the Kavli Institute at Delft. This was a huge boost to the field which immediately attracted abundant experimental and theoretical work.

⁵A material with strong spin-orbit coupling and large g factor.

6.3. Coupling Majorana Fermions to QDs

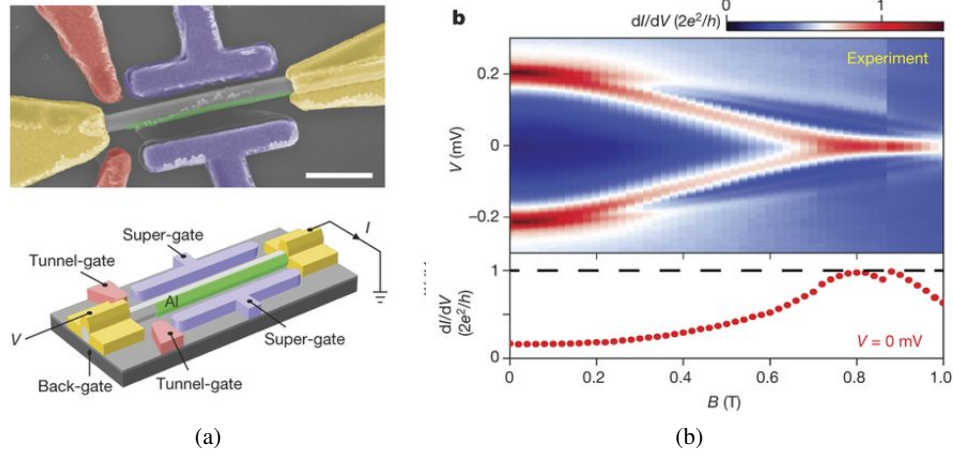


Figure 6.7: (a) Experimental setup (b) Observed magnetic field dependence of the zero bias peak.

| Source: [43]

In just 6 years, more than 5 groups have documented the observation of Majorana signatures [14, 15, 42, 7, 43]. This signature is characterized by the emergence of a robust zero bias conductance peak ZBCP of height $\frac{2e^2}{h}$ produced by the Majorana zero mode MZM localized at the edges of the wire. Though the first experiments didn't observe such a stable signature, the last year Zhang et al. published a paper documenting the observation of this robust peak with the expected theoretical magnitude in an InSb wire Figure 6.7. As can be observed in Figure 6.7(b) the ZBCP increases up to $\frac{2e^2}{h}$ for a strong magnetic field, where the system enters the topological phase according to equation (Equation 6.19).

Despite the successful experimental results, there is still certain skepticism about the existence of Majorana fermions, mainly because Majorana zero-modes (MZM) have been found in superposition with similar types of phenomena that produce zero-modes. Some examples of these are the Andreev bound states or even the Kondo peak [49]. New experimental proposals focus on distinguishing MZMs from these effects and implementing braiding protocols [41, 40?]. One promising idea that could lead to important results in both research lines is coupling Majorana wires with QDs. This will be the objective of the following section.

6.3 Coupling Majorana Fermions to QDs

Liu and Baranger were the first to propose in 2011 the possibility of using QDs in the pursuit of Majorana fermions . When a QD is attached to the end of a Majorana chain in the topological phase, the Majorana Zero Mode at the end of the chain leaks inside the QD [6] producing a zero-bias conductance peak of half a quanta $\frac{e^2}{2h}$ through the dot. This method of detecting Majorana

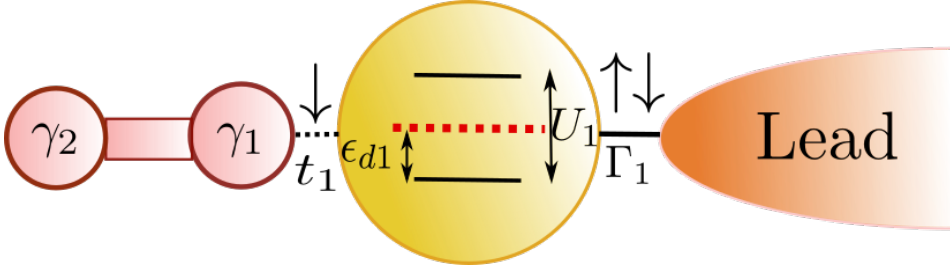


Figure 6.8: Model for the QD-Majorana system. Solid lines: Hopping interactions: V_1 couplings of QD1 . Dashed lines: Majorana spin- \downarrow effective couplings (Equation 6.21) t_1 . The atomic energy levels appear inside each QD ϵ_1 are tuned by the gate voltages. The coulomb interaction is represented by U_1 separates two energy levels. The red dashed horizontal lines represent the Fermi level.

signatures presents the following advantages:

1. The qubit information is not completely destroyed, in contrast to other detection methods such as tunneling spectroscopy.
2. If performed under the Kondo temperature T_k it allows the possibility of observing the MZM co-existing with the Kondo peak, [5, 8, 50] .
3. Today's precise experimental control over the QD parameters allows the manipulation of MZMs inside multi-dot systems, which offers new possibilities to design of quantum architectures with Majorana chains.[44, 45]

In this project we will exploit the second and the third properties to manipulate MZMs in double quantum dot systems in the Kondo regime. But before going through that model, it is necessary to understand the single dot-Majorana coupling.

6.3.1 Model

In this section we will recreate the results of Liu and Baranger using the methods developed in chapter 5 . This will also allow us to probe our methods in a system with Majorana zero modes.

The Hamiltonian for Majorana-QD-lead hybrid system (See Figure 6.8) is given by

$$H = H_{QD-Lead} + H_{M-QD} + H_M. \quad (6.20)$$

Where $H_{QD-Lead}$ is the Hamiltonian for the non-interacting Anderson model (Equation 4.5), H_M is the Hamiltonian of the Majorana chain and H_{M-QD} represents the coupling between the QD and the Majorana Fermion at the boundary.

6.3. Coupling Majorana Fermions to QDs

Now, the real question is how to define the coupling between the QD and the Majorana fermion. In fact, there are many ways to represent this interaction. One alternative is to replace in H_M with the entire Kitaev chain hamiltonian (Equation 6.1) (or even with the Majorana chain (Equation 6.17)) and then pick H_{M-QD} as a simple coupling between the QD and the first site of the chain [6]. A simpler approach is to define an effective coupling with the Majorana operator at the edge of the Majorana chain. Since the Kitaev chain is spin-less, we choose to couple the Majorana to the spin- \downarrow channel of the QD ⁶. Therefore, the Majorana fermion should be the superposition of the creation and annihilation operators of a spin \downarrow particle f_\downarrow :

$$\gamma_1 := \frac{1}{\sqrt{2}} (f_\downarrow^\dagger + f_\downarrow), \gamma_2 := \frac{1}{\sqrt{2}} (f_\downarrow^\dagger - f_\downarrow).$$

This makes possible to define an effective coupling between the Majorana Mode and the dot by attaching γ_1 with the spin- \downarrow channel in the QD

$$H_{M-QD} = t_1 (d_\downarrow^\dagger \gamma_1 + \gamma_1 d_\downarrow) \quad (6.21)$$

Then the coupling with the chain is given by

$$\begin{aligned} H_M &= \varepsilon_m f_\downarrow^\dagger f_\downarrow \\ H_{M-QD} &= \frac{t_1}{\sqrt{2}} d_{1\downarrow}^\dagger f_\downarrow + \frac{t_1^*}{\sqrt{2}} f_\downarrow^\dagger d_{1\downarrow} + \frac{t_1}{\sqrt{2}} d_{1\downarrow}^\dagger f_\downarrow^\dagger + \frac{t_1^*}{\sqrt{2}} f_\downarrow d_{1\downarrow} \end{aligned}$$

Finally we obtain the following hamiltonian

$$H = \sum_{k,\sigma} \left(\varepsilon_k + \frac{U_1}{2} \right) d_{1\sigma}^\dagger d_{1\sigma} + \frac{U}{2} (d_{1\sigma}^\dagger d_{1\sigma} - 1)^2 + t_1 (d_{1\downarrow}^\dagger \gamma_1 + \gamma_1 d_{1\downarrow}) + V d_{1\sigma}^\dagger c_{k\sigma} + V^* c_{k\sigma}^\dagger d_{1\sigma} + \varepsilon_m f_\downarrow^\dagger f_\downarrow. \quad (6.22)$$

The fidelity of this effective model has been discussed by Ruiz-Tijerina et al. [8] concluding that this model reproduces the same results than coupling a Kitaev chain model in the topological phase to a QD. (This statement is true even for more realistic models of the TS including Rashba spin-orbit interactions and a Zeeman field [8]).

6.3.2 Non-interacting QD coupled to Majorana chain

In the non-interacting case we can use the ballistic transport equations from section 5.1. The green functions are then determined by the following set of linear equations.

⁶An appropriate justification of this fact can be found in [8]

$$(\omega - \varepsilon_M) G_{f_{\downarrow}, d_{1\downarrow}^{\dagger}}(\omega) = (\omega + \varepsilon_M) G_{f_{\downarrow}^{\dagger}, d_{1\downarrow}^{\dagger}}(\omega) = \frac{t_1^*}{\sqrt{2}} \left(G_{d_{1\downarrow}, d_{1\downarrow}^{\dagger}}(\omega) - G_{d_{1\downarrow}^{\dagger}, d_{1\downarrow}^{\dagger}}(\omega) \right) \quad (6.23)$$

$$(\omega - \varepsilon_1) G_{d_{1\downarrow}, d_{1\downarrow}^{\dagger}}(\omega) = 1 + \frac{t_1}{\sqrt{2}} t_1 G_{f_{\downarrow}, d_{1\downarrow}^{\dagger}}(\omega) + \frac{t_1}{\sqrt{2}} t_1 G_{f_{\downarrow}^{\dagger}, d_{1\downarrow}^{\dagger}}(\omega) + V_1 \sum_{\mathbf{k}} G_{c_{\mathbf{k}\downarrow}, d_{1\downarrow}^{\dagger}}(\omega) \quad (6.24)$$

$$(\omega - \varepsilon_{\mathbf{k}}) G_{c_{\mathbf{k}}, d_{1\downarrow}^{\dagger}}(\omega) = V_1^* G_{d_{1\downarrow}, d_{1\downarrow}^{\dagger}}(\omega) \quad (6.25)$$

$$(\omega + \varepsilon_1) G_{d_{1\downarrow}^{\dagger}, d_{1\downarrow}^{\dagger}}(\omega) = -\frac{t_1}{\sqrt{2}} G_{f_{\downarrow}, d_{1\downarrow}^{\dagger}}(\omega) - \frac{t_1}{\sqrt{2}} G_{f_{\downarrow}^{\dagger}, d_{1\downarrow}^{\dagger}}(\omega) - V_1^* \sum_{\mathbf{k}} G_{c_{\mathbf{k}\downarrow}^{\dagger}, d_{1\downarrow}^{\dagger}}(\omega) \quad (6.26)$$

$$(\omega + \varepsilon_{\mathbf{k}}) G_{c_{\mathbf{k}}^{\dagger}, d_{1\downarrow}^{\dagger}}(\omega) = -V_1^* G_{d_{1\downarrow}, d_{1\downarrow}^{\dagger}}(\omega) \quad (6.27)$$

The graph representing these green functions is represented in Figure 6.9 a) (Look subsection 5.1.1 for details). However using that $(\omega - \varepsilon_M) G_{f_{\downarrow}, d_{1\downarrow}^{\dagger}}(\omega) = (\omega + \varepsilon_M) G_{f_{\downarrow}^{\dagger}, d_{1\downarrow}^{\dagger}}(\omega)$ we can take $G_{f_{\downarrow}, d_{1\downarrow}^{\dagger}}(\omega)$ out of the equations. After eliminating this term Equation 6.24 becomes

$$(\omega - \varepsilon_1) G_{d_{1\downarrow}, d_{1\downarrow}^{\dagger}}(\omega) = 1 + \frac{t_1}{\sqrt{2}} \left(1 + \frac{\omega - \varepsilon_M}{\omega + \varepsilon_M} \right) G_{f_{\downarrow}, d_{1\downarrow}^{\dagger}}(\omega) + V_1 \sum_{\mathbf{k}} G_{c_{\mathbf{k}\downarrow}, d_{1\downarrow}^{\dagger}}(\omega) \quad (6.28)$$

$$= 1 + \frac{\sqrt{2}t_1}{\omega + \varepsilon_M} G_{f_{\downarrow}, d_{1\downarrow}^{\dagger}}(\omega) + V_1 \sum_{\mathbf{k}} G_{c_{\mathbf{k}\downarrow}, d_{1\downarrow}^{\dagger}}(\omega) \quad (6.29)$$

Similarly,

$$(\omega + \varepsilon_1) G_{d_{1\downarrow}^{\dagger}, d_{1\downarrow}^{\dagger}}(\omega) = -\frac{\sqrt{2}t_1}{\omega + \varepsilon_M} G_{f_{\downarrow}, d_{1\downarrow}^{\dagger}}(\omega) - V_1^* \sum_{\mathbf{k}} G_{c_{\mathbf{k}\downarrow}^{\dagger}, d_{1\downarrow}^{\dagger}}(\omega) \quad (6.30)$$

With these new equations we obtain new associated graph is in Figure 6.9 b) . Using the graph algorithm from subsection 5.1.2 we proceed to pop out vertexes c_k , c_k^{\dagger} and d_1^{\dagger} in that order. The result is the graph in figure Figure 6.9.c) with

$$\varepsilon_{M, d_1^{\dagger}, c^{\dagger}} = \varepsilon_M + \frac{\omega}{\omega + \varepsilon_M} \frac{\|t\|^2}{\omega + \varepsilon_1 + \sum_{\mathbf{k}} \frac{V_1 V_1^*}{\omega + \varepsilon_{\mathbf{k}}}}. \quad (6.31)$$

We finally pop out f_{\downarrow} to obtain

$$G_{d_{1\downarrow}, d_{1\downarrow}^{\dagger}}(\omega) = \left[\omega - \varepsilon_1 - \sum_{\mathbf{k}} \frac{V_1 V_1^*}{\omega - \varepsilon_1} - \frac{\omega}{\omega + \varepsilon_M} \frac{\|t\|^2}{\omega - \varepsilon_{M, d_1^{\dagger}, c^{\dagger}}} \right]^{-1}. \quad (6.32)$$

This is the Green function we have been looking for. After a few algebraic operations it is possible to show that this result is equivalent to the first computation done by Liu and Baranger in the paper [4].

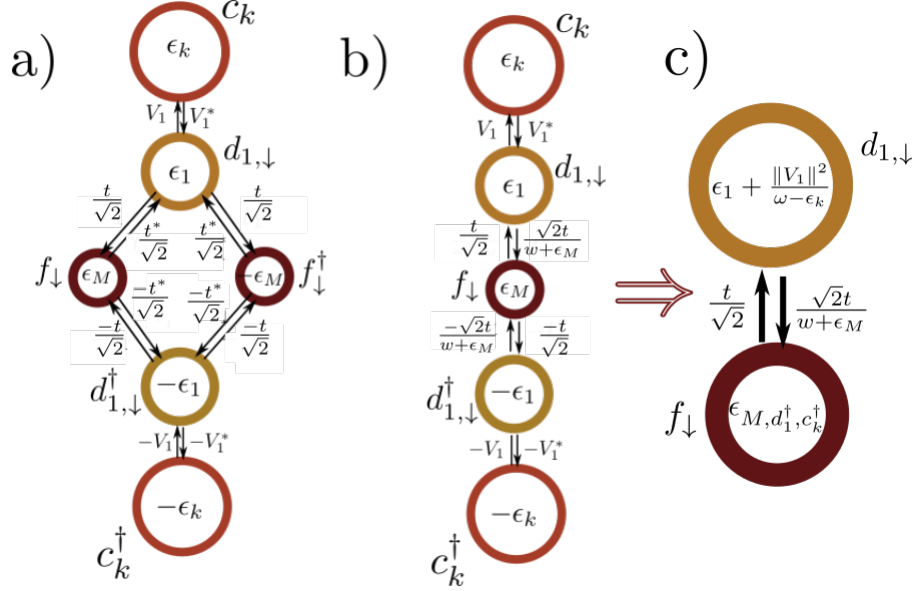


Figure 6.9: Graph \mathcal{G}_M representing the transport equations. Source: By the author

To compute the DOS we need to replace $\sum \frac{V_1 V_1^*}{\omega - \epsilon_k} = -i\Gamma_1$ as we already did in subsection 5.1.1. Note that these computations are only for the spin- \downarrow channel. The spin- \uparrow channel is even simpler since this channel is not coupled to the Majorana mode by convention. Hence it corresponds to the case of a single quantum dot coupled to a Lead. The results for the DOS can be observed in Figure 6.10. Each figure has an inset showing the model in the Majorana representation. The small blue and red balls are Majorana fermions just as the ones in figure Figure 6.2. The Majorana at the edge of the chain is represented by the isolated red ball connected to the QD (Figure 6.10a). The other isolated blue ball in Figure 6.10c represents the Majorana at the other edge which is connected to the sphere by the parameter ϵ .

- **Figure 6.10.(a),(b):** The spin- \uparrow DOS shows the result of coupling the QD with the lead and without Majorana fermions. When the parameter t is increased, the Majorana fermion is couple to the spin- \downarrow which causes the dispersion of the DOS. The most relevant signature is the robust height of 0.5 in the DOS that is observed in the central peak for all $t > 0$. This mid-height DOS is responsible for the decay of half a quanta in the conductivity of the QD.
- **Figure 6.10.(c),(d):** This time a gate voltage is induced in the dot which breaks PHS. However the robust 0.5-height Majorana signature prevails in the dot even at very high gate voltages where the dot is expected to be empty.
- **Figure 6.10.(e),(f):** The term ϵ_M couples both Majoranas at the edges of the chain. The

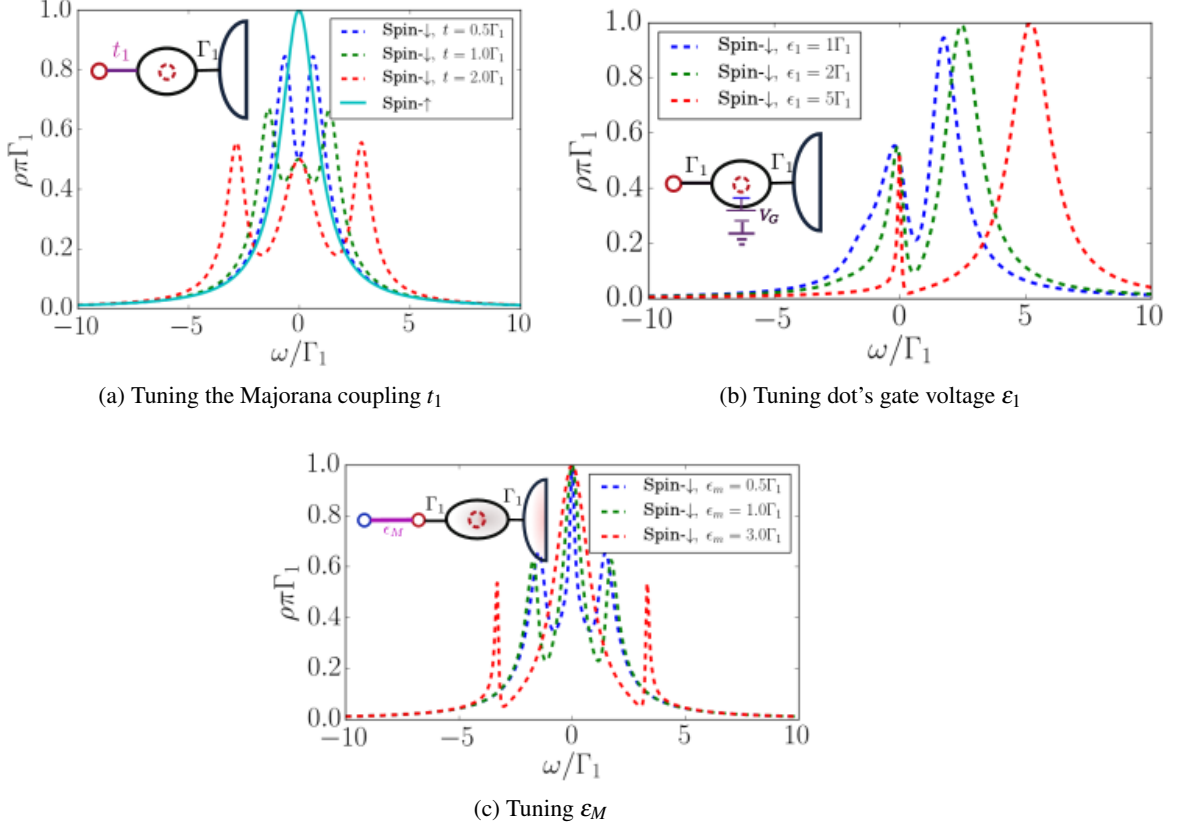


Figure 6.10: Density of states for a Majorana coupled to a QD under the tuning of different parameter. The tuning parameter is drawn in purple line in the inset model.

Source: *By the author*

strength of this parameter decays exponentially with the length of the Majorana chain so that it is often neglected . Here we observe the consequences of including this parameter in the model. The spin- \downarrow DOS emulates the spin- \uparrow DOS for energies $\omega < \epsilon_M$. This clearly destroys the Majorana zero mode.

6.3.3 Kondo-Majorana physics

In interacting quantum dots the Kondo effect is visible at low temperatures even when the QD is attached to a Majorana chain, which allows the study Kondo-Majorana physics. To observe this , we used the NRG code with a fixed Coulomb repulsion of $U = 17.6\Gamma_1$ just as in section subsection 5.2.7. Then, particle-hole equilibrium is achieved when $(\epsilon_1 + \frac{U_1}{2}) \hat{n}_1 \sigma$. Any tuning of the dots gate voltage must be understood as a displacement $\Delta\epsilon_1$ from this equilibrium point.

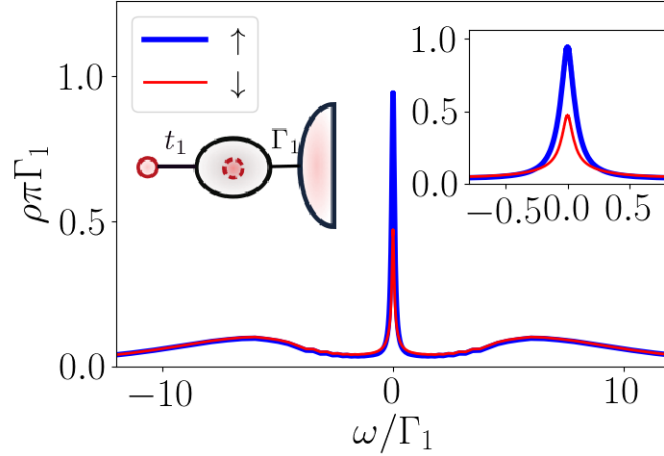


Figure 6.11: DOS at $t_1 = \Gamma_1$ at the PHS-point. Insets: Left: QD-Majorana model. Right: Low energy DOS.

Source: By the author.

Figure 6.11 shows the PHS case for a Majorana coupling $t_1 = \Gamma_1$. The two small wide peaks at the borders of the plot are the coulomb states. In the right inset of the figure, we observe the low-temperature regime inside the gap. There, two zero modes can be appreciated. While the spin- \uparrow DOS is the same Kondo peak from Figure 5.8a, the spin- \downarrow DOS reveals a Majorana zero mode of half the amplitude of the Kondo peak ($\frac{0.5}{\pi\Gamma_1}$). This Majorana signature resembles the one in Figure 6.10a.

It is possible to separate Kondo and Majorana physics by inducing a gate voltage in the dot. As observed in Figure 6.12(a), the gate voltage detunes the Kondo peak from the Fermi energy. Instead, the MZM in Figure 6.12(b) remains at the same position. At $\Delta\epsilon_1 = 5\Gamma_1$ we can already observe a decaying Kondo peak next to the robust Majorana signature of height $\frac{0.5}{\pi\Gamma_1}$ (Figure 6.12(c)). This is more clear in Figure 6.12(d) where the spin- \uparrow DOS decays with $\Delta\epsilon_1$ while the spin- \downarrow DOS is stable, even at $\Delta\epsilon_1 \sim \frac{U}{2} = 8.6$ where the dot is supposed to be empty.

This interesting result was already pointed out by Ruiz-Tijerina et al. who proved that increasing the gate voltage would produce a visible decay in the the zero bias conductance down to $\frac{0.5e^2}{h}$ (See Figure 6.13). Hence, allowing to measure the Majorana signature without the superposition with the Kondo peak. This result is clear from Figure 6.12. At $\Delta\epsilon = 0$ the DOS at the Fermi energy is $\frac{1}{\pi\Gamma_1}$ for spin- \uparrow and $\frac{0.5}{\pi\Gamma_1}$ for spin- \downarrow . Instead, at big $\Delta\epsilon_1$ the only $\frac{0.5}{\pi\Gamma_1}$ spin- \downarrow peak appear. Since the zero bias conductance at zero temperature is essentially the sum of both spectral densities (times unit correction), Figure 6.12 recovers the results in Figure 6.13.

Another possibility to distinguish Kondo and Majorana physics is quenching the Kondo effect with a strong magnetic field . Similar to what was observed in Figure 6.13, the Kondo

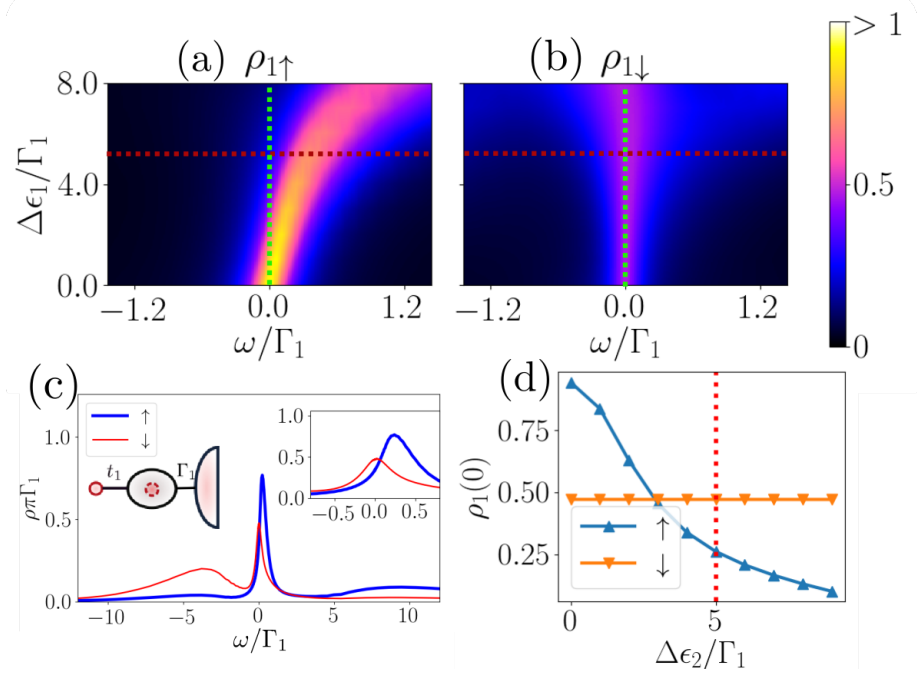


Figure 6.12: (a)&(b): Dependance of the DOS over the gate voltage $\Delta\epsilon_1$ at $t_1 = \Gamma_1$. (a) Spin- \uparrow (b) Spin- \downarrow . (c) DOS at the red-dashed horizontal cut in (a)&(b). Insets: Left: QD-Majorana model. Right: Low energy DOS. (d) DOS at the Green-dashed vertical cut in (a)&(b).

Source: By the author.

peak will be destroyed while the Majorana signature remains stable [8].

6.3.4 State-of-the-art and prospective applications

The possibility of using QD's in the pursuit of Majorana quasi-particles has attracted considerable attention in the last few years. The observation of Kondo signatures in QD-superconductor heterostructures [15] has motivated the study of Kondo-Majorana co-existence in QDs [8, 50] and non-fermi liquid behavior [51]. In addition, the precise experimental control over QDs has opened the possibility of implementing scalable braiding proposals Figure 6.14(a) and quantum architectures for topological quantum computation Figure 6.14(b).

These architectures perform adiabatic evolutions similar to the ones described in subsection 6.1.2 to braid Majorana fermions. This operation strongly relies on the possibility of manipulating the Majorana zero modes inside the dots. The mean idea of MZM manipulation is to tune the gate voltage of one dot to induce the Majoranas to "move" into the other dots. In a prospective braiding protocol, as the one described in [52] (Figure 6.14(a)), this manipulation process would have to be performed several times. However, till this moment MZM

6.3. Coupling Majorana Fermions to QDs

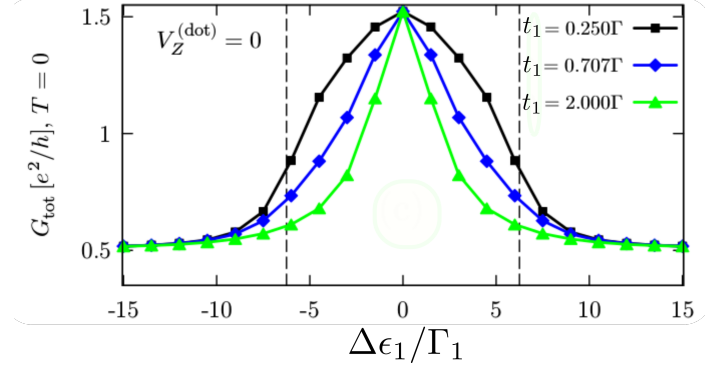


Figure 6.13: Dependence of the zero-bias conductance over tuning voltage

Source: Adapted from [8].

manipulation hasn't been achieved experimentally.

Notwithstanding, the future for this area is still very promising. Recent experiments have documented the observation of Majorana signatures in Majorana-QD devices [7] and Andreev molecules in topological superconductors attached to double quantum dots [53]. The next steps are clearly directed to achieve Majorana manipulation. The simplest device where this process is possible is in a double quantum dot (DQD). This fundamental case is the mean objective of this thesis and will be treated in the following chapter.

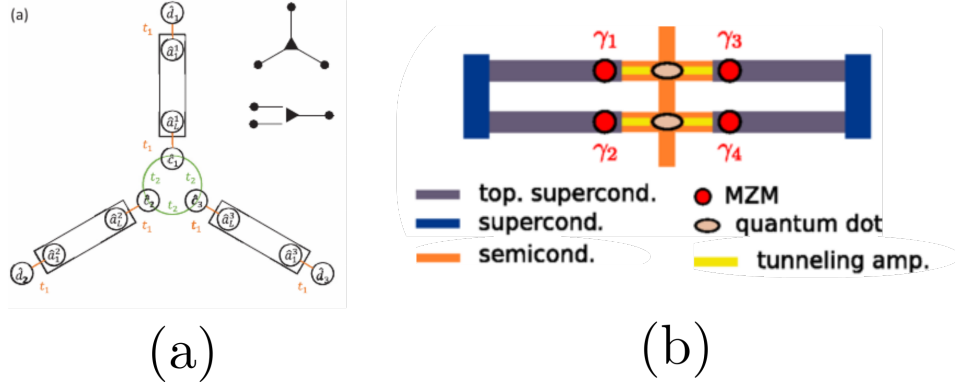


Figure 6.14: a) Braiding proposal b) Basic architecture with four Majorana Zero Modes in a scalable quantum computer.

Source: Adapted from (a) [52] (b) [45].

Chapter 7

Coupling the Majorana Zero Mode to a Double Quantum Dot

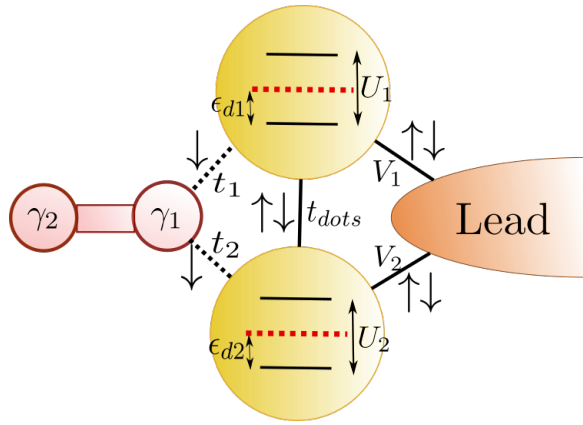


Figure 7.1: Model for the DQD-Majorana system. Solid lines: Hopping interactions (t_{dots} : inter-dot coupling , V_1, V_2 couplings of QD1 and QD2 with the lead). Dashed lines: Majorana spin- \downarrow effective couplings (t_1, t_2). The atomic energy levels appear inside each QD ϵ_1, ϵ_2 are tuned by the gate voltages. The coulomb interaction is represented by U_1, U_2 . The red dashed horizontal lines represent the Fermi level.

Source: *By the Author*

A DQD-Majorana device is the most fundamental structure where Majorana manipulation is possible. Tunneling Majorana modes in these basic structures have inspired theoretical studies [? 54] and experimental setups confirming the observations of Andreev molecules [53]. Even though quantum tunneling of a MZM into a double dot offers several possibilities for manipulation of MZMs, there is still no complete analysis of the transitions of the Majorana signatures between the QDs in this model.

In this chapter, we will explore the different possibilities for Majorana manipulation in a device consisting of a DQD coupled to a MZM and a metallic lead (See Fig. ??). The simplicity of this model allows us to explore analytically different geometries of QD's from linear couplings to T-junctions (Fig. Figure 7.3). As in the single dot device , we will consider both non-interacting and interacting regimes.

7.1. Applying our methods to the DQD-Majorana system

The model in Figure 7.1 can be described from the combination of the Hamiltonians of a QD-Majorana system (Equation 6.22) and a DQD (Equation 5.11). Integrating these models we obtain

$$H = \sum_{i=1}^2 \sum_{k,\sigma} \left(\varepsilon_i + \frac{U_i}{2} \right) d_{i\sigma}^\dagger d_{i\sigma} + \frac{U_i}{2} (d_{i\sigma}^\dagger d_{i\sigma} - 1)^2 + t_i (\gamma d_{i\downarrow} + d_{i\downarrow}^\dagger \gamma) + V_i d_{i\sigma}^\dagger c_{k\sigma} + V_i^* c_{k\sigma}^\dagger d_{i\sigma}. \quad (7.1)$$

Where V_1, V_2 is the coupling of dots 1,2 with the lead. t_1, t_2 define the Majorana couplings with each dot. t_{dots} is the interdot coupling. $\varepsilon_1, \varepsilon_2$ are the energy levels of the dot, which are tuned by the the voltage and U_1, U_2 are the coulomb repulsion parameters.

7.1 Applying our methods to the DQD-Majorana system

In order to understand the physical properties of this model, we probed a set of thought processes. The main variable in this analysis is the density of states. We will observe its evolution on both QDs under the tuning of the model parameters such as the majorana couplings (t_1, t_2), gate voltages ($\varepsilon_1, \varepsilon_2$) and the inter dot coupling (t_{dots}). With these processes intend to show whether it is possible to "manipulate" the majorana modes inside the dots by tuning the established parameters. The number of possible combinations of parameters is huge and not all of them lead to important results. So on, we used the ballistic transport to select which arrangements could bring novel results. The most interesting models were simulated with NRG in the interacting case ??.

7.1.1 Non-interacting Green function:

This new model is a combination the DQD graph (Figure 5.1) with the Majorana-QD graph Figure 6.9.b). We can use the trick in ?? to get rid of the of the Green function $G_{f_{1\downarrow}, d_{1\downarrow}^\dagger}(\omega)$ for the second Majorana operator. This allows us to obtain the following transport equations

$$\begin{bmatrix} \omega - \varepsilon_1 & -V_1^* & -t_{dots} & -T_1 & 0 & 0 & 0 \\ -V_1 & \omega - \varepsilon_k & -V_2 & 0 & 0 & 0 & 0 \\ -t_{dots}^* & -V_2^* & \omega - \varepsilon_2 & -T_2 & 0 & 0 & 0 \\ -T_1^* & 0 & -T_2^* & \omega - \varepsilon_M & -T_2^* & 0 & -T_1 \\ 0 & 0 & 0 & -T_2 & \omega + \varepsilon_2 & V_2^* & t_{dots}^* \\ 0 & 0 & 0 & 0 & V_2 & \omega + \varepsilon_k & V_1 \\ 0 & 0 & 0 & -T_1 & t_{dots} & V_1^* & \omega + \varepsilon_1 \end{bmatrix} \begin{bmatrix} G_{d_{1\downarrow}, d_{1\downarrow}^\dagger}(\omega) \\ G_{c_{k\downarrow}, d_{1\downarrow}^\dagger}(\omega) \\ G_{d_{2\downarrow}, d_{1\downarrow}^\dagger}(\omega) \\ G_{f_{1\downarrow}, d_{1\downarrow}^\dagger}(\omega) \\ G_{d_{2\downarrow}^\dagger, d_{1\downarrow}^\dagger}(\omega) \\ G_{c_{k\downarrow}^\dagger, d_{1\downarrow}^\dagger}(\omega) \\ G_{d_{1\downarrow}^\dagger, d_{1\downarrow}^\dagger}(\omega) \end{bmatrix} = \begin{bmatrix} 0 \\ 0 \\ 0 \\ 0 \\ 0 \\ 0 \\ 1 \end{bmatrix}, \quad (7.2)$$

where $T_i = \frac{t_i}{\sqrt{\omega + \varepsilon_M}}$.

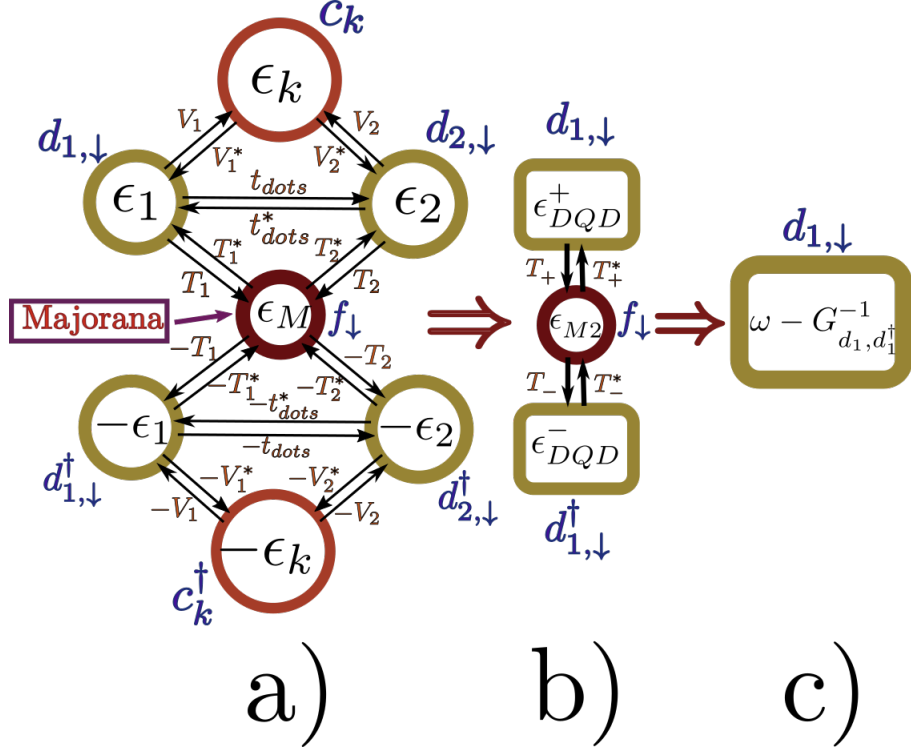


Figure 7.2: Graph method applied to a DQD coupled to a Majorana zero mode. a) Initial stage. b) Popped vertexes c_k^\dagger , c_k , $d_{2,\downarrow}$, $d_{2,\dagger\downarrow}$ in that order. c) Popped vertexes $d_{1,\downarrow}^\dagger$ and f_\downarrow , the final energy is $\omega - G_{d_1, d_1^\dagger}(\omega)$.

Source: By the Author

The graph representing this equation is Figure 7.2.a). Using the algorithm in subsection 5.1.2 we start to popping the vertexes c_k , c_k^\dagger , $d_{2,\downarrow}$ and $d_{2,\dagger\downarrow}$ in that order. The energies associated to $d_{1,\downarrow}$ and $d_{1,\dagger\downarrow}^\dagger$ will be similar to the energy of the DQD (Equation 5.18) giving

$$\epsilon_{DQD}^\pm = \pm \epsilon_1 + \sum_{\mathbf{k}} \frac{V_1 V_1^*}{\omega - \epsilon_{\mathbf{k}}} + \frac{\left| \pm t_{dots} + \sum_{\mathbf{k}} \frac{V_1 V_2^*}{\omega - \epsilon_{\mathbf{k}}} \right|^2}{\omega \pm \epsilon_2 - \sum_{\mathbf{k}} \frac{V_2 V_2^*}{\omega - \epsilon_{\mathbf{k}}}}. \quad (7.3)$$

There is also a correction in the couplings between the Majorana mode and $d_{1,\downarrow}$, $d_{1,\dagger\downarrow}^\dagger$ given by

$$T_\pm = \pm t_1 \pm t_2 \frac{\left(\pm t_{dots} + \sum_{\mathbf{k}} \frac{V_1 V_2^*}{\omega - \epsilon_{\mathbf{k}}} \right)}{\omega \pm \epsilon_2 \pm \sum_{\mathbf{k}} \frac{V_2 V_2^*}{\omega - \epsilon_{\mathbf{k}}}}. \quad (7.4)$$

7.1. Applying our methods to the DQD-Majorana system

In addition since the Majorana is in contact with dot 2, there is an extra-term appearing in the Majorana energy given by

$$\varepsilon_{M2} = \omega - \varepsilon_M - \frac{\frac{\omega}{\omega + \varepsilon_M} \|t_2\|^2}{\omega - \varepsilon_2 - \sum_{\mathbf{k}} \frac{V_2 V_2^*}{\omega - \varepsilon_{\mathbf{k}}}} - \frac{\frac{\omega}{\omega + \varepsilon_M} \|t_2\|^2}{\omega + \varepsilon_2 - \sum_{\mathbf{k}} \frac{V_2 V_2^*}{\omega + \varepsilon_{\mathbf{k}}}}. \quad (7.5)$$

It only remains to pop out vertexes d_1^\dagger and f_\downarrow in that order to obtain the green function

$$G_{d_{1\downarrow}, d_{1\downarrow}^\dagger}(\omega) = \frac{1}{\omega - \varepsilon_{DQD}^+ - \frac{\|T_+\|^2}{\omega - \varepsilon_{M2} - \frac{\|T_-\|^2}{\varepsilon_{DQD}^-}}}. \quad (7.6)$$

This simple formula summarizes the transport information through the first dot of the non-interacting Majorana-DQD system. To compute the DOS we just need to replace once again $\sum_{\mathbf{k}} \frac{V_1 V_1^*}{\omega - \varepsilon_{\mathbf{k}}} = -i\Gamma_1$ as performed in subsection 5.1.1. By plotting the final DOS in Mathematica we were able to observe the transitions of the Majorana mode while manipulating the model parameters.

7.1.2 NRG for the interacting system

The Numerical Renormalization Group (NRG) technique described in section 5.2 is the most successful methods to study interacting quantum impurity models. In this model, the impurity is described by the DQD attached to the MZM. In our code, we set a Coulomb repulsion factor of $U = 17.3\Gamma_1$ in both dots and a cut-off energy of $D = 2U = 34.6\Gamma_1$. The spacing with other energy levels is assumed to be higher than D , such that only the two coulomb states are relevant for the system dynamics. When $\varepsilon_i = \frac{U}{2}$ in both dots, the system is in the Particle-Hole-Symmetric region. At this point, each dot has an odd number of electrons, hence, at sufficiently low temperature the system will exhibit characteristic Kondo peaks at the Fermi energy Wilson [24]. The coexistence of Kondo and Majorana zero modes is still a point of contention in the area and one of the objectives of this part of the project.

To improve the efficiency of the code we used the symmetries of the system to maintain a block structure during NRG's iterative diagonalization process. This model preserves the spin- \uparrow particle number \hat{N}_\uparrow and the spin- \downarrow parity $\hat{P}_\downarrow = \pm (+\text{even}, -\text{odd})$. The spin- \downarrow particle number is not preserved due to superconducting-type Majorana coupling (??). The initial Hamiltonian is organized in blocks according to these symmetries. This block structure is preserved during the entire iteration process [33]. To compute the spectral functions, we use the density matrix renormalization group (DM-NRG) described in section subsection 5.2.5 in combination with the Z-trick method [37], which improves spectral resolution at high energies.

To initialize the model in Figure 5.7 we set H_{-1} equal to

$$H = \sum_{i=1}^2 \sum_{k,\sigma} \left(\varepsilon_i + \frac{U_i}{2} \right) d_{i\sigma}^\dagger d_{i\sigma} + \frac{U_i}{2} (d_{i\sigma}^\dagger d_{i\sigma} - 1)^2 + t_i (\gamma d_{i,\downarrow} + d_{i,\downarrow}^\dagger \gamma), \quad (7.7)$$

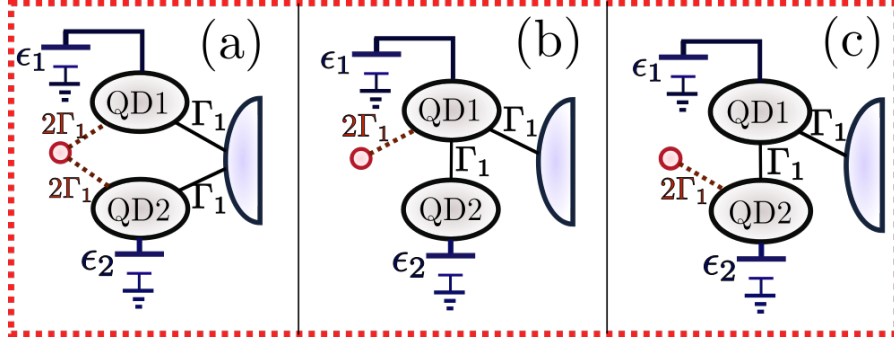


Figure 7.3: . Source: By the Author

and wrote the Hamiltonian in the symmetry-block diagonal representation (see section B.1). We also include manually the Hamiltonian H_0 into the code to guarantee that both quantum dots are coupled to the first site of the chain. After this, the code follows the standard NRG algorithm and prints the density matrices to initialize DM-NRG. The final result is the spectral density which contains sufficient physical information to study the MZM-DQD model. In the following section, we show how the density of states can be used to simulate the Manipulation process of an MZM inside the dQD.

7.2 Manipulation of Majorana zero modes

The density of states provides significant information about the presence of a Majorana zero modes in the dot. We characterize the Majorana signature by a robust zero-mode with two possible heights:

- **Type I:** The spin- \downarrow DOS is the half of the spin- \uparrow DOS at the Fermi energy ($\rho_{\downarrow}(0) = \rho_{\uparrow}(0)$).
- **Type II:** A spin- \downarrow zero mode of height $\rho_{\downarrow}(0) = \frac{0.5}{\pi\Gamma_1}$.

In our results we observe several times these two types of signatures. Type I often appears when there is a zero-mode in the spin- \uparrow DOS. Type II emerges in the remaining situations.

We call MZM manipulation to the "movements" attributed to the Majorana signature under the tuning of the dot gate voltages (ϵ_1, ϵ_2). This manipulation process is performed in three different set ups that are presented in Figure 7.3 with definite values of Γ_2, t_{dots}, t_1 and t_2 . In configuration (a), we couple the QD symmetrically to the lead and the Majorana mode. With this setup we expect to break the localization of the MZM which should split and tunnel into both dots. In setups (b) and (c) we couple the second dot indirectly through the first dot. Hence, quantum interference should split the zero mode in two states. Our objective is to observe what occurs with the Majorana signature in this situation. There are two options to connect the MZM

in this situation. Attached it directly through the first dot (b) or indirectly through the second dot (c). Both alternatives are geometrically distinct since (b) suggests a T-junction coupling while (c) reflects a connection in series of both QD's between the lead and the MZM.

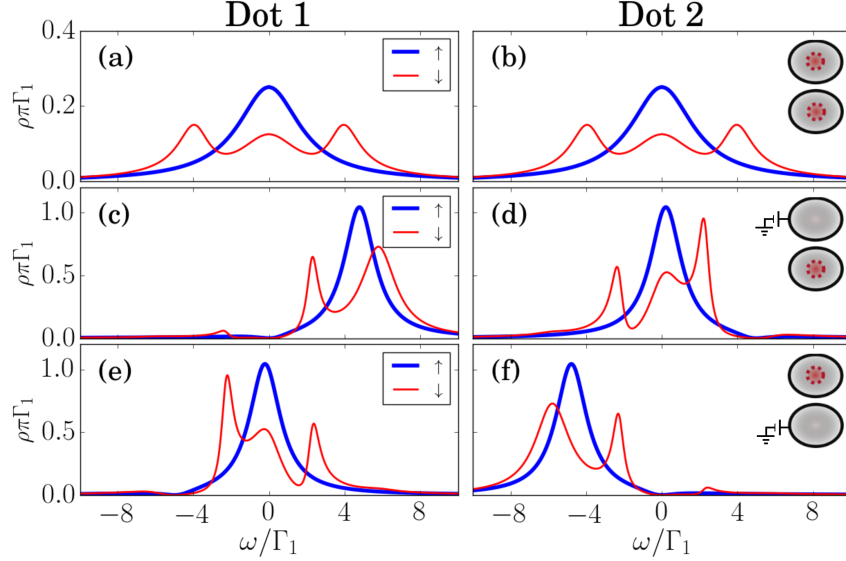


Figure 7.4: Non-interacting DOS in the symmetric coupling setup (Figure 7.3(a)) at each QD. First column: Dot 1. Second column: Dot 2. The gate voltages vary at each row. First row: Zero gate voltages $\varepsilon_1 = \varepsilon_2 = 0$. Second row: $\varepsilon_1 = 5\Gamma_1$, $\varepsilon_2 = 0$. Third row: $\varepsilon_1 = 0$, $\varepsilon_2 = -5\Gamma_1$. Bold blue lines: Spin- \uparrow DOS. Thin red lines: Spin- \downarrow DOS. The insets at the right show which dot carries a Majorana signature, represented by a red dashed circle. Upper: First dot. Lower: Second dot.

Source: By the Author

7.2.1 Non-interacting manipulation

The non-interacting results for setups (a),(b) and (c) of Figure 7.3 are shown at figures Figure 7.4, Figure 7.5 and Figure 7.6 respectively. Each figure depicts the DOS of dot 1(left) and dot 2(right). The gate voltage is initially 0 in both dots at the first row. In the second row, the gate voltage is turned on to $\varepsilon_1 = 5\Gamma_1$, while the second dot remains at $\varepsilon_2 = 0$. In the third row the first dot's voltage is off $\varepsilon_1 = 0$ and we switch on the second dot with a negative voltage of $\varepsilon_2 = -5\Gamma_1$. The inset figures at the right side of each row show which dots exhibit Majorana signatures, depicted by a red dashed circle inside the dot. These images will continuously change under the tuning of gate voltages which represents the manipulation of the Majorana signature.

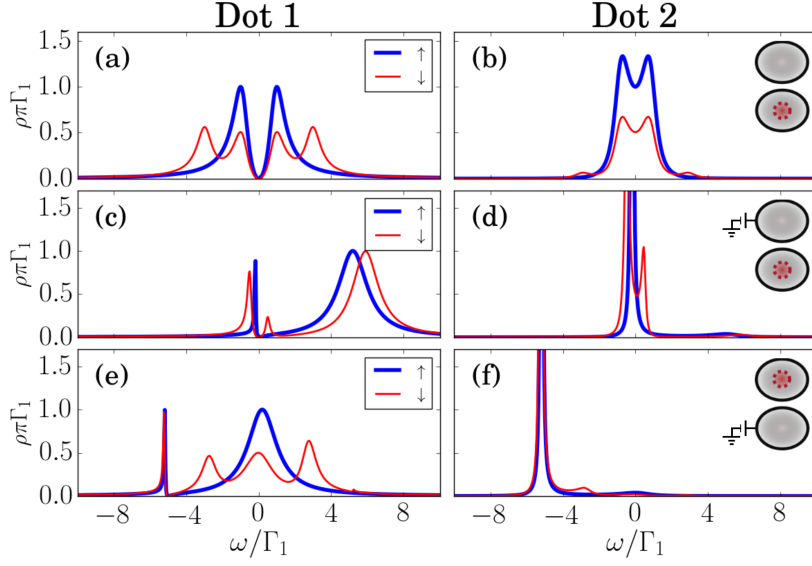


Figure 7.5: Non-interacting DOS of the setup in Figure 7.3(b). (b). First line (a),(b): $\epsilon_1 = \epsilon_2 = 0$. Second line (c),(d): $\epsilon_1 = 5\Gamma_1$, $\epsilon_2 = 0$. Third line (e),(f): $\epsilon_2 = -5\Gamma_1$, $\epsilon_1 = 0$. Blue bold lines: Spin- \uparrow DOS. Red thin lines: Spin- \downarrow DOS. The inset at the upper-right corner of each line indicates which dots exhibit Majorana signature, which is represented by a red dashed circle inside the dot.

Source: By the Author

In Figure 7.4 we observe the results for the symmetric coupling setup Figure 7.3(a). In the particle hole symmetric case (first row) the DOS is equal in both dots. Note that that the spin- \downarrow (Thin red line) DOS is the half of the spin- \uparrow (Bold blue line) DOS at the Fermi energy ($\rho_{\downarrow}(0) = \frac{1}{2}\rho_{\uparrow}(0)$). This type II Majorana signature is similar to the one observed when a single dot is coupled to a Majorana mode. [4] We may conclude that the Majorana in tunneling inside both dots breaking the localization of the MZM. If a positive or negative gate voltage is induced in one of the dots, as shown in the second and third row of Figure Figure 7.4(c)-(f), the Majorana zero mode vanishes from that dot. Meanwhile the density of states in the other dot increases while preserving the Majorana signature. This means that the MZM is actually being induced to "leave" this dots and leak into the other dot by the gate voltage activation. This first example of MZM manipulation.

Another example of MZM manipulation occurs when the second dot is not directly connected to the lead. In this case, the inter-dot tunneling generates quantum interference which finally destroys the central peak as observe in Figure 7.5(a) at the spin- \uparrow DOS . The spin- \downarrow channel at Figure 7.5(a), which is coupled to the MZM, does not exhibit the characteristic Fermi peak

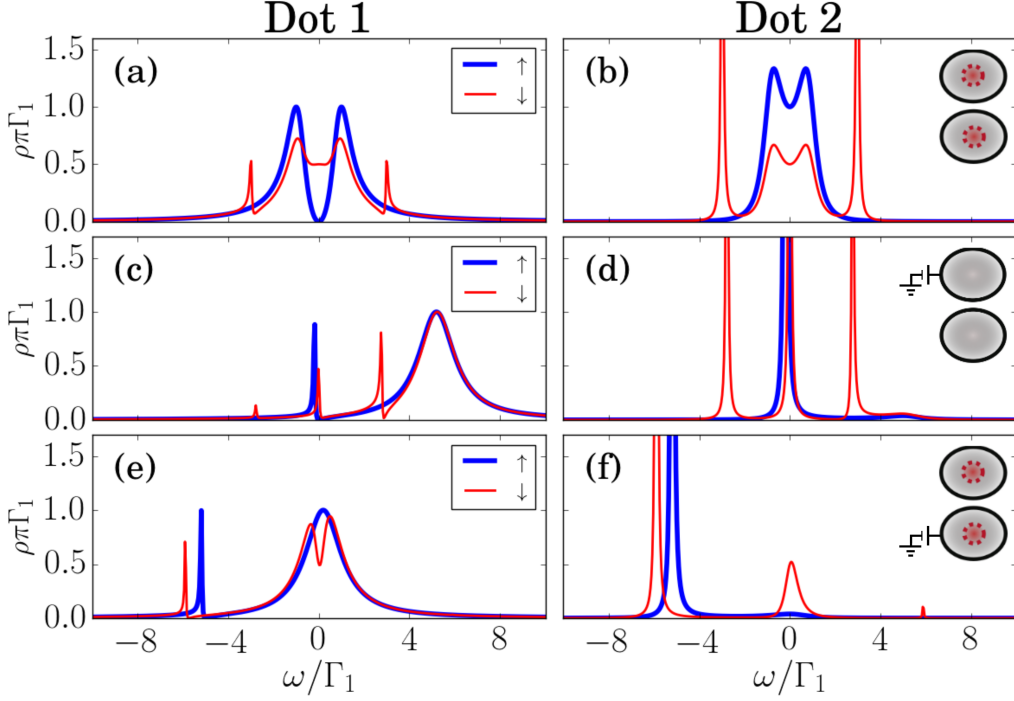


Figure 7.6: Non-interacting DOS of the set up in Figure 7.3(c). First line (a),(b): $\varepsilon_1 = \varepsilon_2 = 0$. Second line (c),(d): $\varepsilon_1 = 5\Gamma_1$, $\varepsilon_2 = 0$. Third line (e),(f): $\varepsilon_2 = -5\Gamma_1$, $\varepsilon_1 = 0$. Blue bold lines: Spin- \uparrow DOS. Red thin lines: Spin- \downarrow DOS. The inset at the upper-right corner of each line indicates which dots exhibit Majorana signature, which is represented by a red dashed circle inside the dot.

Source: By the Author

either. Instead, the one half Majorana signature at the Fermi energy ($\rho_\downarrow(0) = \frac{1}{2}\rho_\uparrow(0)$) appears clearly inside the second dot Figure 7.5(b). This situation prevails when the first dot's gate voltage is turned on Figure 7.5(c)&(d). While the first dot does not seem to exhibit any type of Majorana signature, the second dot's spin- \downarrow DOS exhibits a robust zero-mode of height $\frac{0.5}{\pi\Gamma}$. The results are more exciting when the second dot's gate voltage is turned on in Figure 7.5(e)&(f). These figures clearly show how the MZM, previously localized at the second dot, is induced to leave this dot and returned onto the first dot. Moreover, the DOS of spin- \uparrow and spin- \downarrow channels are very similar to the spectral densities observed at Figure 7.4(d)(e), which means that the previous interference pattern has disappeared due to the presence of this gate voltage.

The results of the third configuration Figure 7.3(c) appear in Figure 7.6. Contrary to what was observed in the previous case, this time the Majorana signature is not destroyed by the interference but instead, the $\frac{0.5}{\pi\Gamma}$ -height MZM emerges indirectly in the first dot. This is a perfect

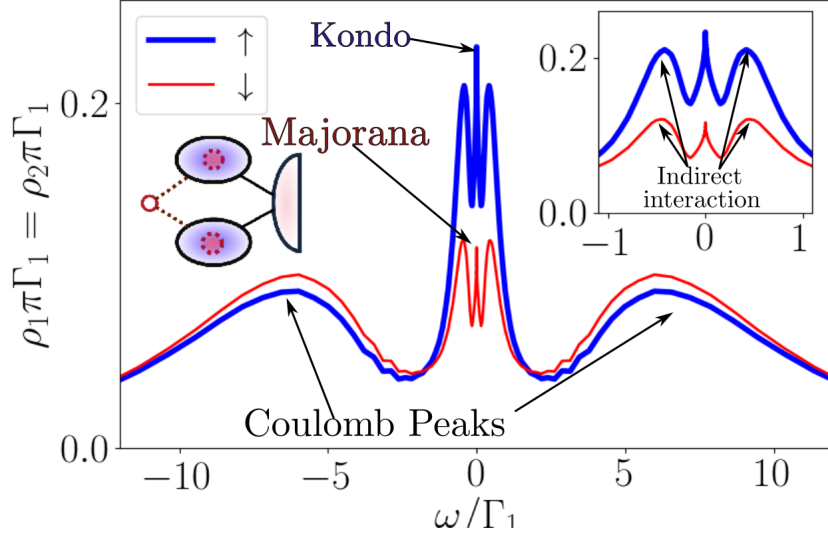


Figure 7.7: Density of states of both dots in the symmetric coupling without gate voltages between the Majorana and the interacting DQD. Bold blue lines: Spin- \uparrow DOS. Thin red lines: Spin- \downarrow DOS. Inset: Low-energy DOS.

Source: By the Author

way to separate the Majorana's spin- \downarrow DOS from the central spin- \uparrow zero-mode which is still destroyed by the interference. In addition, the second dot still exhibits a type I Majorana signature as observed in Figure 7.6(b). In the second row we observe that turning on the gate voltage in dot 1 destroys the Majorana signature in both dots Figure 7.6(c)(d). On the other hand, if the second dot's voltage is switched both dots will preserve their Majorana signature (QD1:type I, QD2: type II), while the spin- \uparrow quantum interference vanishes in the first dot.

7.2.2 Interacting manipulation

Now we consider a Coulomb repulsion energy of $U = 17\Gamma_1$ in both dots. The factor $\frac{U_i}{2}(\sum_{\sigma} \hat{n}_{i\sigma} - 1)^2$ in (??) favors states with an odd number of electrons (and holes). In addition, particle-hole equilibrium is now achieved when $\Delta\epsilon_i := (\epsilon_i + \frac{U_i}{2})\hat{n}_{i\sigma}$. Any induced gate voltage must be considered as a shifting $\Delta\epsilon_i$ from this equilibrium point. FIGFigure 7.7 shows the DOS of both QDs for the symmetric coupling configuration Figure 7.3. The two peaks appearing at around $8.6\Gamma_1 = \frac{U_i}{2}$ represent the two energy levels spaced by the Coulomb repulsion factor U . The central spin- \uparrow peak is a consequence of the Kondo effect, [18, 24] while the two satellite peaks observed in the inset are the result of the RKKY indirect interaction between both dots. [19, 20, 21] Moreover, the system presents a Majorana signature characterized by half spin- \downarrow

7.2. Manipulation of Majorana zero modes

DOS at the Fermi energy ($\rho_{\downarrow}(0) = \frac{1}{2}\rho_{\uparrow}(0)$) . Note, that in this case the Majorana signature coexists with the Kondo effect in the DQD as already predicted by Ruiz-Tijerina *et al.* for a single dot. [8]

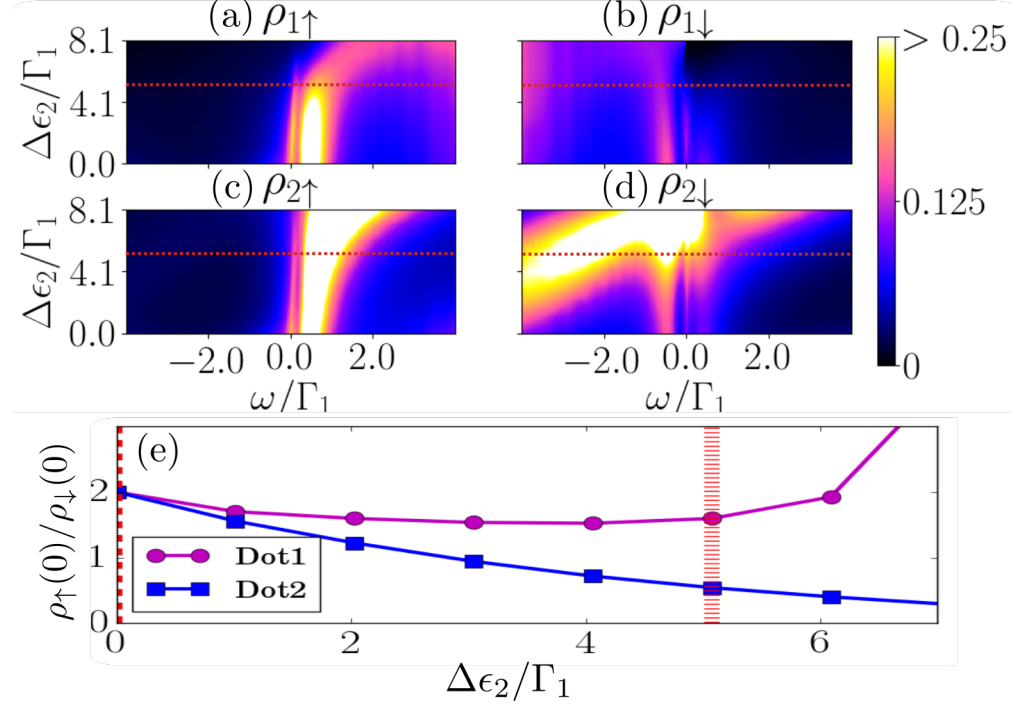


Figure 7.8: (a)-(d) Dependence of the density of states of setup in Figure 7.3(a) over ω and the gate voltage $\Delta\epsilon_2$. $\Delta\epsilon_1 = 0$ Up: Dot 1. Down: Dot 2. Left: Spin- \uparrow . Right: Spin- \downarrow . (e) Evolution of the relation $\frac{\rho_1(0)}{\rho_1(0)}$ for both QDs. While QD2 losses rapidly the Majorana signature, QD1 maintains it till $\Delta\epsilon_2 \sim 5$.

Source: By the Author

In this part project we are interested in the physics at low energy scales $\omega \sim \Gamma_1$ close to the Kondo and MZM temperature. At this scale we can observe similar Majorana signatures compared with the non-interacting case. For instance, the inset Figure 7.7 shows the NRG results for the symmetric setup in Figure 7.3(a). In agreement with the non-interacting results, both dots have type I Majorana signatures.

When the gate voltage is turned on, we observe the number of holes $\omega > 0$ increasing in the spin- \uparrow , while the particles $\omega < 0$ increase in the spin- \downarrow (See Figure 7.8(a)-(d)). At $\Delta\epsilon_2 \approx 6\Gamma_1$, the Coulomb peak overlaps with the Fermi energy in the spin- \downarrow channel, destroying the Majorana zero mode. This event is visible in Figure 7.8(e), where the type one Majorana signature is clearly destroyed in Dot 1 after $\Delta\epsilon_2 > 6\Gamma_1$. For $\Delta\epsilon_2 < 6\Gamma_1$ we observe an stable Majorana

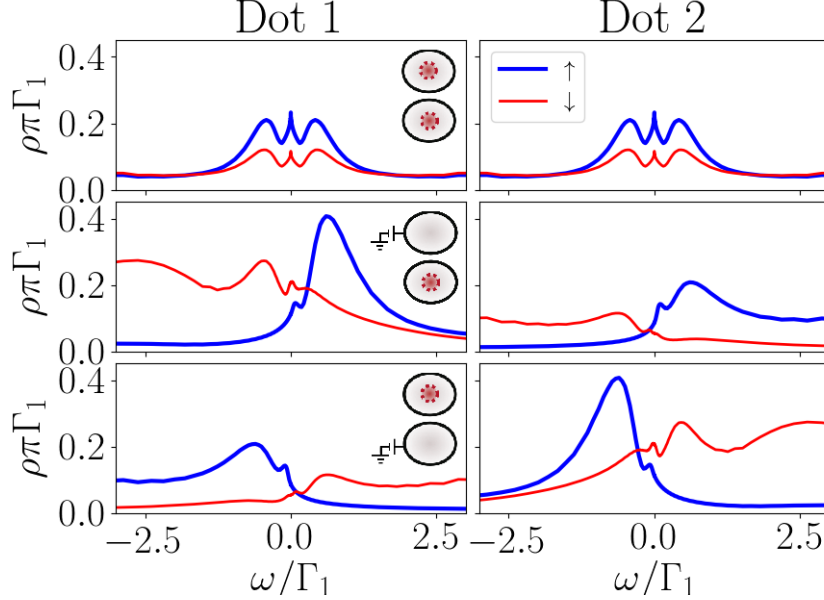


Figure 7.9: The same as in Figure 7.4 for the interacting DOS in the symmetric coupling setup (Figure 7.3).

Source: By the Author

signature in dot 1 with $\rho_{\downarrow}(0) \approx \frac{1}{2}\rho_{\uparrow}(0)$). In the second dot the zero modes are absorbed by the dot, which slowly destroys the Majorana signature.

The red cuts in Figure 7.8 are plotted in Figure 7.9 where we depict the results of Majorana manipulation. In agreement with the non-interacting case, the particle hole symmetric model receives both Majorana modes. Whenever a gate voltage is switched on, the Majorana is forced to tunnel into the other dot. We observe similar results for positive and negative gate voltages.

In the second setup Figure 7.3(b), the spin- \uparrow Kondo peak in Figure 7.10 is destroyed by interference just as in the non-interacting case. This phenomenon had already been predicted for a T-junction of a double quantum dot attached to metallic leads [22]. The insight of our model is that an attached MZM should also disappear due to the same interference. Furthermore, a type I Majorana signature can be observed at very low energies in the inset of Figure 7.10(b). However we have to recognize that both zero-modes decay significantly in the second dot. When the first voltage is turned on, the Majorana mode jumps onto the first dot which presents a type I Majorana signature. This is a clear difference with the non-interacting results where the Majorana signature stayed in the second dot. If the second dot is switched on, a type II Majorana signature appears at very low energies in dot 1, which is coherent with the idea that the Majorana interference should disappear in this case. In Figure 7.10(e) we identify emergence

7.2. Manipulation of Majorana zero modes

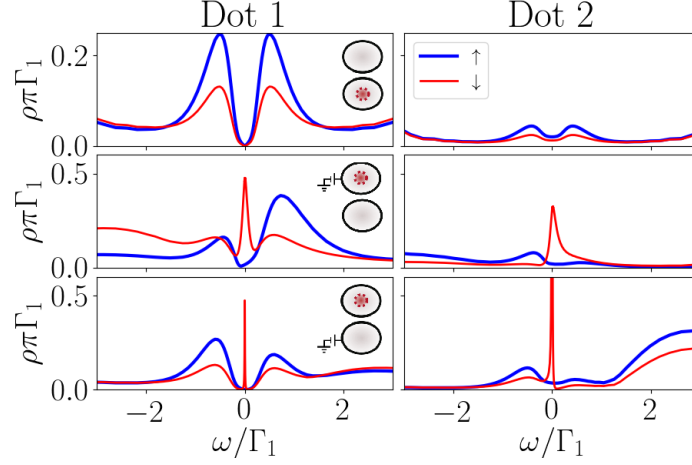


Figure 7.10: The same as in Figure 7.4 for the interacting DOS of the setup in Figure 7.3(b). Inset in b): Low-energy DOS.

Source: By the Author

of a Fano resonance at the Fermi energy causing the sharp-asymmetric peak at $\omega = 0$. Fano resonances have already been documented in similar models in [55]. We are going to talk more about this resonance in following sections.

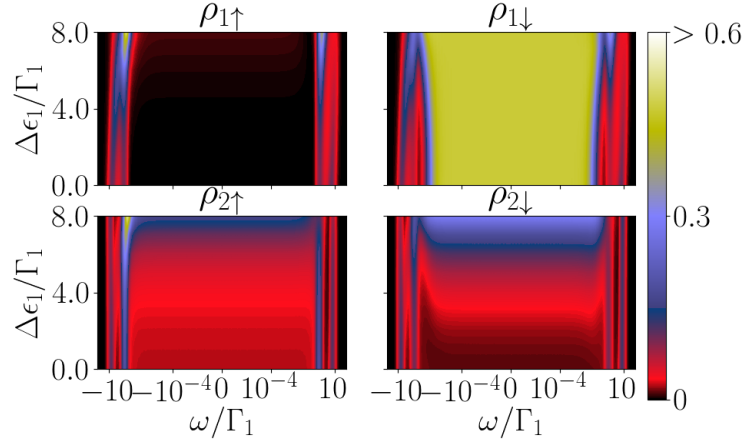


Figure 7.11: Logarithmic dependence of the density of states in setup Figure 7.3(c) over ω and the gate voltage $\Delta\epsilon_1$. $\Delta\epsilon_2 = 0$. The dependence over $\Delta\epsilon_2$ produces similar results.

Source: By the Author

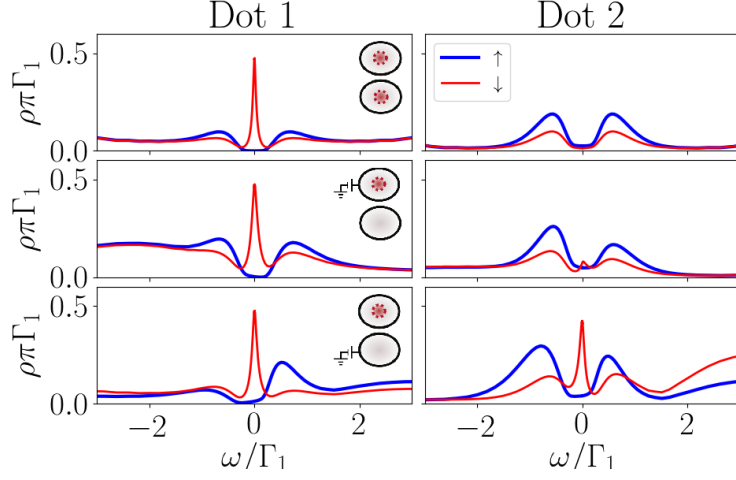


Figure 7.12: The same as in Figure 7.4 for the interacting DOS of the setup in Figure 7.3(b). Inset in b): Low-energy DOS.

Source: By the Author

Finally, Figure 7.12 shows the NRG results for the last configuration in Figure 7.3(c). Notably, the indirectly-attached MZM exhibits a robust type II Majorana signature in the first dot over a destroyed Kondo peak. This is observed clearly in Figure 7.11 where $\rho_{1\downarrow}$ exhibits a constant $\frac{0.5}{\pi\Gamma_1}$ -height Majorana peak . This signature is stable under the gate voltage tuning in dot 1 and similar results are obtained in dot 2 . In addition, only in the particle hole symmetric case the second dot presents a type II Majorana signature (Inset Figure 7.12(b)).

We could understand this effect by thinking that the dots in model (c) are attached in series. Therefore both QDs can be thought as extensions of the Kitaev chain, were the first dot is the last place in the wire. Hence the Majorana should be localized at this dot despite the application of gate voltages. This case is similar to the case of a single dot attached to a Majorana chain, where it is known that the MZM appears in the dot even when this is supposed to be empty [6]. It still remains the doubt about why this effect is not observed in the non-interacting case . On the other hand, there is a fano resonance at the Fermi energy in the spin- \downarrow DOS Figure 7.12(d)(e) . This zero mode was not identified as a potential Majorana signature since it varies with the values of $\Delta\varepsilon_1$ (Figure 7.11) and $\Delta\varepsilon_2$.

We are now writing a paper summarizing these results. As we observed, we were able to characterize the transitions of the Majorana signature in different geometric arrangements of the dots. In the following section we will present some ideas that are still in development. We hope they could lead us to future publications

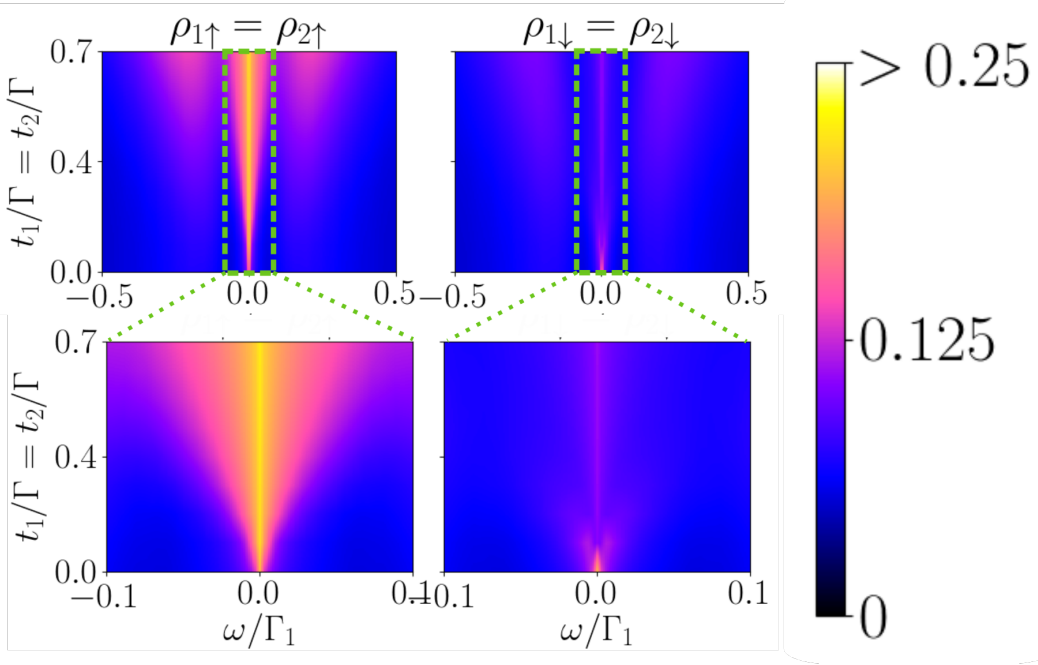


Figure 7.13: Dependence of the DOS in the symmetric model Figure 7.3(a) over $t_1 = t_2$ and ω . Up: High energy . Down: Zoom to low energy states.

Source: By the Author

7.3 Additional results

This section contains additional results that we are considering to study in future publications.

7.3.1 Indirect exchange through the Majorana mode

In Figure 7.7 we observed the emergence of satellite peaks at low energies product of anti-ferromagnetic exchange interactions. This exchange interaction can occur through the lead and through the Majorana mode. The reason why we are observing just two satellites is because the Majorana $t_1 = t_2$ coupling and the broadening parameters $\Gamma_1 = \Gamma_2$ are about the same order. Hence the peaks are a superposition of both exchange interactions.

We can separate both exchange interactions by observing the dependence of the DOS at different orders of $t_1 = t_2$ in Figure 7.14. We can distinguish two regimes:

1. Low Majorana coupling $t_1 = t_2 < 0.5$: Two additional satellite peaks appear in the spin- \downarrow DOS (See inset in ?? for better appreciation). These peaks are similar to the Kondo satellites that appear at high energies. However, since they appear only at low-energies,

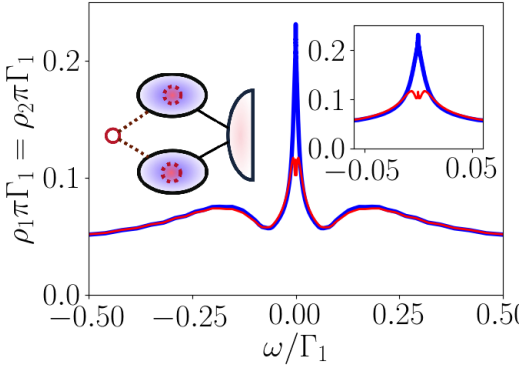


Figure 7.14: Dependence of the DOS in the symmetric model Figure 7.3(a) over $t_1 = t_2$ and ω . Up: High energy . Down: Zoom to low energy states.

Source: By the Author

it is clear that they are produced by the MZM. We conclude that these two satellites are produced by the indirect exchange through the attached Majorana quasi-particle. These

- High Majorana coupling $t_1 = t_2 > 0.5$: When the Majorana coupling is high enough, the indirect exchange through the MZM occurs in the same energy scale as the Kondo satellites. Notably, the spin- \downarrow satellite peaks in the high energy regime are not affected by this effect. Instead, a visible inflation of the satellites in the spin- \uparrow DOS is observed. Therefore the MZM is actually correlated with the spin- \uparrow DOS through the satellite peaks. This is unexpected since the Majorana is only coupled to the spin- \downarrow channel. The only explanation for this is that these satellites are formed by a strongly correlated state between the MZM, the dot states and the lead.

7.3.2 Indirect Majorana coupling through the lead

Imagine a model where we connect both dots symmetrically to the leads but we only connect the MZM to the first dot. In addition, we do not allow inter-dot tunneling. Then the only connection between the MZM and the second would be passing through the first dot and the lead. We didn't expect to see any Majorana signature in the second dot in these conditions. However, Figure 7.15 shows a clear type I Majorana signature in the second dot.

Note also that the density of states in the second dot is very small in comparison with the first dot. This is intriguing since this dot is directly connected with the lead and it is still at the Kondo regime. This ambiguity means that the zero-bias DOS is favored by a direct coupling to an MZM.

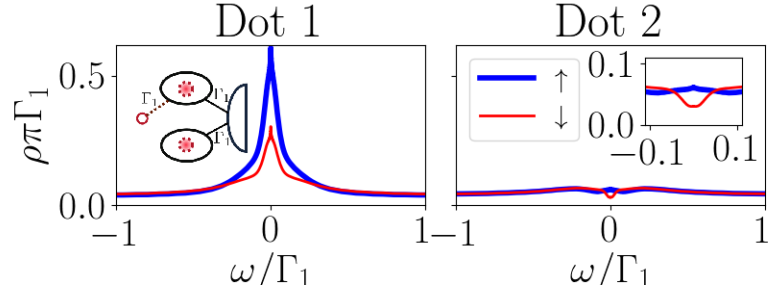


Figure 7.15: DOS at both dots for the model in the left inset. The right inset zooms the low-energy DOS in the second dot.

Source: By the Author

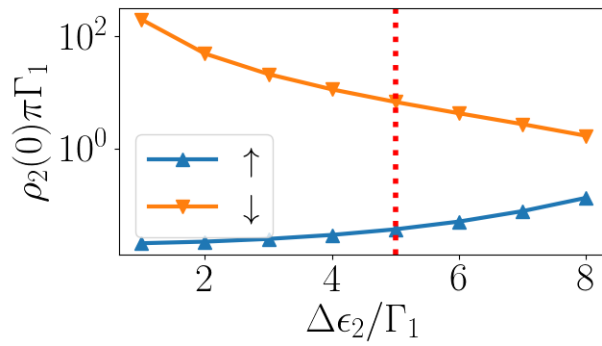


Figure 7.16: Logarithmic dependence of the DOS in the second dot for setup in Figure 7.3(b) over the second gate voltage. Cut at $5\Gamma_1$ corresponds to Figure 7.10(f).

Source: By the Author

7.3.3 Critical behavior in zero-bias DOS

In Figure 7.10(f) we observe a sharp peak at DOS. This peak is actually a big problem for our results since they are mainly supported on the spectral densities at the Fermi energy. In Figure 7.16 we observe a critical behaviour in the zero-bias DOS close to $\Delta\epsilon_2 = 0$. This is quite intriguing .

Chapter 8

Conclusions

Comparing the exact analytical solution in the non-interacting system and the NRG results for interacting quantum dots, we were able to characterize the displacements of the MZM inside the double quantum dot for the three setups in FIG.Figure 7.3. All these manipulations are summarized in Figure 8.1 . We observe a considerable agreement on the location of the Majorana signature between the interacting and non-interacting results:

FIG.Figure 7.3(a): In the symmetric coupling the MZM leaks inside both dots. For interacting dots, the Majorana signature will be distinguishable near the Kondo temperature. At this regime the system presents combined Kondo-Majorana physics . If the gate voltage of one dot is turned on the MZM is induced to tunnel only into the other dot.

FIG.Figure 7.3(b): In this system the spin- \uparrow zero mode at QD1 (The Kondo peak if the system is interacting) is destroyed by quantum interference with the second dot. This interference will also destroy the MZM in the first dot but a type I Majorana signature will still appear in the second dot. The Majorana mode can be induced to tunnel back into the first dot if a gate voltage is applied on the second dot. This signature is visible at very low energies (bellow $0.1\Gamma_1$) in interacting case.

FIG.Figure 7.3(c): An indirect type II Majorana signature is observed in the first dot. This signature is robust, specially in the interacting case, where it is present in all configurations.

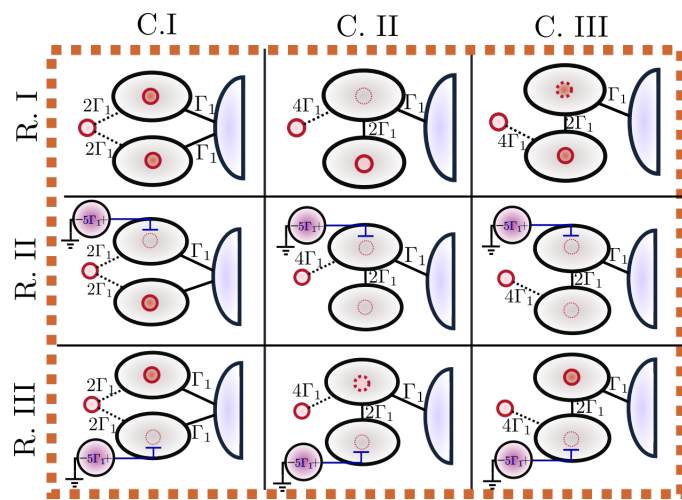


Figure 8.1: Table of Majorana signatures in the studied cases .

Bibliography

- [1] A. Yu Kitaev. Unpaired Majorana fermions in quantum wires. *Phys.-Usp.*, 44(10S):131, 2001. ISSN 1063-7869. doi: 10.1070/1063-7869/44/10S/S29. URL <http://stacks.iop.org/1063-7869/44/i=10S/a=S29>. 1, 3, 6
- [2] Jason Alicea. Majorana fermions in a tunable semiconductor device. *Phys. Rev. B*, 81(12):125318, March 2010. doi: 10.1103/PhysRevB.81.125318. URL <https://link.aps.org/doi/10.1103/PhysRevB.81.125318>. 1, 6
- [3] Jason Alicea. New directions in the pursuit of Majorana fermions in solid state systems. *Rep. Prog. Phys.*, 75(7):076501, 2012. ISSN 0034-4885. doi: 10.1088/0034-4885/75/7/076501. URL <http://stacks.iop.org/0034-4885/75/i=7/a=076501>. 1, 3, 6, 6.1.1, 6.6, 6.2, 6.2, 6.2
- [4] Dong E. Liu and Harold U. Baranger. Detecting a majorana-fermion zero mode using a quantum dot. 84(20). ISSN 1098-0121, 1550-235X. doi: 10.1103/PhysRevB.84.201308. URL <http://arxiv.org/abs/1107.4338>. 1, 3, 6, 6.3, 6.3.1, 6.3.2, 7.2.1
- [5] Minchul Lee, Jong Soo Lim, and Rosa Lopez. Kondo effect in a quantum dot side-coupled to a topological superconductor. 87(24):241402. doi: 10.1103/PhysRevB.87.241402. URL <https://link.aps.org/doi/10.1103/PhysRevB.87.241402>. 1, 2
- [6] E. Vernek, P. H. Penteado, A. C. Seridonio, and J. C. Egues. Subtle leakage of a majorana mode into a quantum dot. 89(16):165314. doi: 10.1103/PhysRevB.89.165314. URL <https://link.aps.org/doi/10.1103/PhysRevB.89.165314>. 1, 3, 6.3, 6.3.1, 7.2.2
- [7] M. T. Deng, S. Vaitiekėnas, E. B. Hansen, J. Danon, M. Leijnse, K. Flensberg, J. Nygård, P. Krogstrup, and C. M. Marcus. Majorana bound state in a coupled quantum-dot hybrid-nanowire system. 354(6319):1557–1562. ISSN 0036-8075, 1095-9203. doi: 10.1126/science.aaf3961. URL <http://science.sciencemag.org/content/354/6319/1557>. 1, 6, 6.2, 6.3.4
- [8] David A. Ruiz-Tijerina, E. Vernek, Luis G. G. V. Dias da Silva, and J. C. Egues. Interaction effects on a majorana zero mode leaking into a quantum dot. 91(11):115435. doi: 10.1103/PhysRevB.91.115435. URL <https://link.aps.org/doi/10.1103/PhysRevB.91.115435>. 1, 3, 3.1, 2, 6.3.1, 6, 6.3.3, 6.3.4, 6.13, 7.2.2

Bibliography

- [9] A. Yu Kitaev. Fault-tolerant quantum computation by anyons. *Annals of Physics*, 303(1):2–30, January 2003. ISSN 00034916. doi: 10.1016/S0003-4916(02)00018-0. URL <http://arxiv.org/abs/quant-ph/9707021>. arXiv: quant-ph/9707021. 3, 6
- [10] Frank Wilczek. Majorana returns, September 2009. URL <https://www.nature.com/articles/nphys1380>. 3
- [11] Liang Fu and C. L. Kane. Superconducting Proximity Effect and Majorana Fermions at the Surface of a Topological Insulator. *Phys. Rev. Lett.*, 100(9):096407, March 2008. doi: 10.1103/PhysRevLett.100.096407. URL <https://link.aps.org/doi/10.1103/PhysRevLett.100.096407>. 3
- [12] Masatoshi Sato, Yoshiro Takahashi, and Satoshi Fujimoto. Non-Abelian Topological Order in \$s\$-\$s\$-Wave Superfluids of Ultracold Fermionic Atoms. *Phys. Rev. Lett.*, 103(2):020401, July 2009. doi: 10.1103/PhysRevLett.103.020401. URL <https://link.aps.org/doi/10.1103/PhysRevLett.103.020401>. 3
- [13] V. Mourik, K. Zuo, S. M. Frolov, S. R. Plissard, E. P. a. M. Bakkers, and L. P. Kouwenhoven. Signatures of Majorana Fermions in Hybrid Superconductor-Semiconductor Nanowire Devices. *Science*, 336(6084):1003–1007, May 2012. ISSN 0036-8075, 1095-9203. doi: 10.1126/science.1222360. URL <http://science-sciencemag.org.ez67.periodicos.capes.gov.br/content/336/6084/1003>. 3, 6, 6.2
- [14] Anindya Das, Yuval Ronen, Yonatan Most, Yuval Oreg, Moty Heiblum, and Hadas Shtrikman. Zero-bias peaks and splitting in an Al-InAs nanowire topological superconductor as a signature of Majorana fermions. *Nature Physics*, 8(12):887, December 2012. ISSN 1745-2481. doi: 10.1038/nphys2479. URL <https://www.nature.com/articles/nphys2479>. 3, 6, 6.2
- [15] M. T. Deng, C. L. Yu, G. Y. Huang, M. Larsson, P. Caroff, and H. Q. Xu. Anomalous Zero-Bias Conductance Peak in a Nb-InSb Nanowire-Nb Hybrid Device. *Nano Letters*, 12(12):6414–6419, December 2012. ISSN 1530-6984. doi: 10.1021/nl303758w. URL <http://dx.doi.org/10.1021/nl303758w>. 3, 6, 6.2, 6.3.4
- [16] Yuval Oreg, Gil Refael, and Felix von Oppen. Helical Liquids and Majorana Bound States in Quantum Wires. *Physical Review Letters*, 105(17):177002, October 2010. doi: 10.1103/PhysRevLett.105.177002. URL <https://link.aps.org/doi/10.1103/PhysRevLett.105.177002>. 3
- [17] Roman M. Lutchyn, Jay D. Sau, and S. Das Sarma. Majorana Fermions and a Topological Phase Transition in Semiconductor-Superconductor Heterostructures. *Physical Review Letters*, 105(7):077001, August 2010. doi: 10.1103/PhysRevLett.105.077001. URL <https://link.aps.org/doi/10.1103/PhysRevLett.105.077001>. 3, 6.2

Bibliography

- [18] Alexander Cyril Hewson. *The Kondo Problem to Heavy Fermions*. Cambridge University Press, April 1997. ISBN 978-0-521-59947-4. Google-Books-ID: fPzgHneNFDAC. 3, 4.3, 7.2.2
- [19] M. A. Ruderman and C. Kittel. Indirect Exchange Coupling of Nuclear Magnetic Moments by Conduction Electrons. *Physical Review*, 96(1):99–102, October 1954. doi: 10.1103/PhysRev.96.99. URL <https://link.aps.org/doi/10.1103/PhysRev.96.99>. 3, 7.2.2, B
- [20] Tadao Kasuya. A Theory of Metallic Ferro- and Antiferromagnetism on Zener’s Model. *Progress of Theoretical Physics*, 16(1):45–57, July 1956. ISSN 0033-068X. doi: 10.1143/PTP.16.45. URL <https://academic.oup.com/ptp/article/16/1/45/1861363>. 3, 7.2.2
- [21] Kei Yosida. Magnetic Properties of Cu-Mn Alloys. *Physical Review*, 106(5):893–898, June 1957. doi: 10.1103/PhysRev.106.893. URL <https://link.aps.org/doi/10.1103/PhysRev.106.893>. 3, 7.2.2, B
- [22] Luis G. G. V. Dias da Silva, Nancy Sandler, Kevin Ingersent, and Sergio E. Ulloa. Transmission in double quantum dots in the Kondo regime: Quantum-critical transitions and interference effects. *Physica E: Low-dimensional Systems and Nanostructures*, 40(5):1002–1005, March 2008. ISSN 1386-9477. doi: 10.1016/j.physe.2007.08.098. URL <http://www.sciencedirect.com/science/article/pii/S1386947707003074>. 3, 5.2.7, 7.2.2
- [23] D. N. Zubarev. DOUBLE-TIME GREEN FUNCTIONS IN STATISTICAL PHYSICS. *Soviet Physics Uspekhi*, 3(3):320, 1960. ISSN 0038-5670. doi: 10.1070/PU1960v003n03ABEH003275. URL <http://iopscience.iop.org/article/10.1070/PU1960v003n03ABEH003275/meta>. 3.1
- [24] Kenneth G. Wilson. The renormalization group: Critical phenomena and the Kondo problem. *Reviews of Modern Physics*, 47(4):773–840, October 1975. doi: 10.1103/RevModPhys.47.773. URL <https://link.aps.org/doi/10.1103/RevModPhys.47.773>. 3.1, 5.2.1, 5.4, 7.1.2, 7.2.2
- [25] Alexander W. Holleitner, Robert H. Blick, Andreas K. HäUttel, Karl Eberl, and JÄ¶rg P. Kotthaus. Probing and Controlling the Bonds of an Artificial Molecule. *Science*, 297(5578):70–72, July 2002. ISSN 0036-8075, 1095-9203. doi: 10.1126/science.1071215. URL <http://science.sciencemag.org/content/297/5578/70>. 4.1
- [26] Dieter Bimberg, Marius Grundmann, and Nikolai N. Ledentsov. *Quantum Dot Heterostructures*. Wiley, Chichester, Eng.; New York, 1 edition, March 1999. ISBN 978-0-471-97388-1. 4.1, 4.1

Bibliography

- [27] Michael Sindel. *Numerical Renormalization Group studies of Quantum Impurity Models in the Strong Coupling Limit.* Text.PhDThesis, Ludwig-Maximilians-Universitat Munchen, January 2005. URL <https://edoc.ub.uni-muenchen.de/3115/>. 4.1, 4.3, 4.2, A.1
- [28] P. W. Anderson. Localized Magnetic States in Metals. *Physical Review*, 124(1):41–53, October 1961. doi: 10.1103/PhysRev.124.41. URL <https://link.aps.org/doi/10.1103/PhysRev.124.41>. 4.2
- [29] W.J. de Haas, J. de Boer, and G.J. van de Berg. The electrical resistance of gold, copper and lead at low temperatures. *Physica*, 1(7):1115 – 1124, 1934. ISSN 0031-8914. doi: [https://doi.org/10.1016/S0031-8914\(34\)80310-2](https://doi.org/10.1016/S0031-8914(34)80310-2). URL <http://www.sciencedirect.com/science/article/pii/S0031891434803102>. 4.4, 4.3
- [30] W. G. van der Wiel, S. De Franceschi, T. Fujisawa, J. M. Elzerman, S. Tarucha, and L. P. Kouwenhoven. The Kondo Effect in the Unitary Limit. *Science*, 289(5487):2105–2108, September 2000. ISSN 0036-8075, 1095-9203. doi: 10.1126/science.289.5487.2105. URL <http://science-scienmag-org.ez67.periodicos.capes.gov.br/content/289/5487/2105>. 4.5
- [31] D. Goldhaber-Gordon, Hadas Shtrikman, D. Mahalu, David Abusch-Magder, U. Meirav, and M. A. Kastner. Kondo effect in a single-electron transistor. *Nature*, 391(6663):156–159, January 1998. ISSN 1476-4687. doi: 10.1038/34373. URL <https://www.nature.com/articles/34373>. 4.3.1
- [32] Daniel A Spielman. Algorithms, graph theory, and linear equations in laplacian matrices. In *Proceedings of the International Congress of Mathematicians*, volume 4, pages 2698–2722, 2010. URL <http://www.mathunion.org/ICM/ICM2010.4/Main/icm2010.4.2698.2722.pdf>. 5.1.1, 5.1.1
- [33] Ralf Bulla, Theo A. Costi, and Thomas Pruschke. Numerical renormalization group method for quantum impurity systems. *Reviews of Modern Physics*, 80(2):395–450, April 2008. doi: 10.1103/RevModPhys.80.395. URL <https://link.aps.org/doi/10.1103/RevModPhys.80.395>. 5.2.1, 5.2.1, 7.1.2, A.1
- [34] H. R. Krishna-murthy, J. W. Wilkins, and K. G. Wilson. Renormalization-group approach to the Anderson model of dilute magnetic alloys. 1. Static properties for the symmetric case. *Phys.Rev.*, B21:1003–1043, 1980. doi: 10.1103/PhysRevB.21.1003. 5.2.1, 5.2.1, A.1, A.1
- [35] T. A. Costi, A. C. Hewson, and V. Zlatic. Transport coefficients of the Anderson model via the numerical renormalization group. *Journal of Physics: Condensed Matter*, 6(13):2519, 1994. ISSN 0953-8984. doi: 10.1088/0953-8984/6/13/013. URL <http://stacks.iop.org/0953-8984/6/i=13/a=013>. 5.2.5

Bibliography

- [36] Walter Hofstetter. Generalized Numerical Renormalization Group for Dynamical Quantities. *Physical Review Letters*, 85(7):1508–1511, August 2000. doi: 10.1103/PhysRevLett.85.1508. URL <https://link.aps.org/doi/10.1103/PhysRevLett.85.1508>. 5.2.5
- [37] Wanda C. Oliveira and Luiz N. Oliveira. Generalized numerical renormalization-group method to calculate the thermodynamical properties of impurities in metals. *Physical Review B*, 49(17):11986–11994, May 1994. doi: 10.1103/PhysRevB.49.11986. URL <https://link.aps.org/doi/10.1103/PhysRevB.49.11986>. 5.2.6, 7.1.2
- [38] Jiannis K. Pachos. *Introduction to Topological Quantum Computation*. Cambridge University Press, Cambridge ; New York, 1 edition edition, May 2012. ISBN 978-1-107-00504-4. 6, 6.1.2
- [39] C.w.j. Beenakker. Search for Majorana Fermions in Superconductors. *Annual Review of Condensed Matter Physics*, 4(1):113–136, March 2013. ISSN 1947-5454. doi: 10.1146/annurev-conmatphys-030212-184337. URL <https://www.annualreviews.org/doi/10.1146/annurev-conmatphys-030212-184337>. 6
- [40] Sankar Das Sarma, Michael Freedman, and Chetan Nayak. Majorana zero modes and topological quantum computation. *npj Quantum Information*, 1:15001, October 2015. ISSN 2056-6387. doi: 10.1038/npjqi.2015.1. URL <https://www.nature.com/articles/npjqi20151>. 6, 6.2
- [41] David Aasen, Michael Hell, Ryan V. Mishmash, Andrew Higginbotham, Jeroen Danon, Martin Leijnse, Thomas S. Jespersen, Joshua A. Folk, Charles M. Marcus, Karsten Flensberg, and Jason Alicea. Milestones Toward Majorana-Based Quantum Computing. *Physical Review X*, 6(3):031016, August 2016. doi: 10.1103/PhysRevX.6.031016. URL <https://link.aps.org/doi/10.1103/PhysRevX.6.031016>. 6, 6.2
- [42] Stevan Nadj-Perge, Ilya K. Drozdov, Jian Li, Hua Chen, Sangjun Jeon, Jungpil Seo, Allan H. MacDonald, B. Andrei Bernevig, and Ali Yazdani. Observation of Majorana fermions in ferromagnetic atomic chains on a superconductor. *Science*, 346(6209):602–607, October 2014. ISSN 0036-8075, 1095-9203. doi: 10.1126/science.1259327. URL <http://science.scienmag.org/content/346/6209/602>. 6, 6.2
- [43] Hao Zhang, Chun-Xiao Liu, Sasa Gazibegovic, Di Xu, John A. Logan, Guanzhong Wang, Nick van Loo, Jouri D. S. Bommer, Michiel W. A. de Moor, Diana Car, Roy L. M. Op het Veld, Petrus J. van Veldhoven, Sebastian Koelling, Marcel A. Verheijen, Mihir Pendharkar, Daniel J. Pennachio, Borzoyeh Shojaei, Joon Sue Lee, Chris J. Palmström, Erik P. A. M. Bakkers, S. Das Sarma, and Leo P. Kouwenhoven. Quantized Majorana conductance. *Nature*, 556:74, March 2018. URL <http://dx.doi.org/10.1038/nature26142>. 6, 6.7, 6.2

Bibliography

- [44] Maissam Barkeshli and Jay D. Sau. Physical Architecture for a Universal Topological Quantum Computer based on a Network of Majorana Nanowires. *arXiv:1509.07135 [cond-mat, physics:quant-ph]*, September 2015. URL <http://arxiv.org/abs/1509.07135>. arXiv: 1509.07135. 6, 3
- [45] Torsten Karzig, Christina Knapp, Roman M. Lutchyn, Parsa Bonderson, Matthew B. Hastings, Chetan Nayak, Jason Alicea, Karsten Flensberg, Stephan Plugge, Yuval Oreg, Charles M. Marcus, and Michael H. Freedman. Scalable designs for quasiparticle-poisoning-protected topological quantum computation with Majorana zero modes. *Physical Review B*, 95(23):235305, June 2017. doi: 10.1103/PhysRevB.95.235305. URL <https://link.aps.org/doi/10.1103/PhysRevB.95.235305>. 6, 3, 6.14
- [46] Vladimir G. Turaev. *Quantum Invariants of Knots and 3-Manifolds*. De Gruyter, Berlin, Boston, 3rd corr. ed. edition, 2016. ISBN 978-3-11-043522-1. URL <https://www.degruyter.com/view/product/461906>. 6.1.2
- [47] Chetan Nayak, Steven H. Simon, Ady Stern, Michael Freedman, and Sankar Das Sarma. Non-Abelian anyons and topological quantum computation. *Reviews of Modern Physics*, 80(3):1083–1159, September 2008. doi: 10.1103/RevModPhys.80.1083. URL <https://link.aps.org/doi/10.1103/RevModPhys.80.1083>. 6.1.2
- [48] A. Manchon, H. C. Koo, J. Nitta, S. M. Frolov, and R. A. Duine. New perspectives for Rashba spin-orbit coupling. *Nature Materials*, 14(9):871–882, September 2015. ISSN 1476-4660. doi: 10.1038/nmat4360. URL <https://www.nature.com/articles/nmat4360>. 6.2
- [49] Eduardo J. H. Lee, Xiaocheng Jiang, Ramón Aguado, Georgios Katsaros, Charles M. Lieber, and Silvano De Franceschi. Zero-Bias Anomaly in a Nanowire Quantum Dot Coupled to Superconductors. *Physical Review Letters*, 109(18):186802, October 2012. doi: 10.1103/PhysRevLett.109.186802. URL <https://link.aps.org/doi/10.1103/PhysRevLett.109.186802>. 6.2
- [50] G. Górski, J. Barański, I. Weymann, and T. Domański. Interplay between correlations and Majorana mode in proximitized quantum dot. *Scientific Reports*, 8(1):15717, October 2018. ISSN 2045-2322. doi: 10.1038/s41598-018-33529-1. URL <https://www.nature.com/articles/s41598-018-33529-1>. 2, 6.3.4
- [51] Rok Åœitko and Pascal Simon. Quantum impurity coupled to Majorana edge fermions. *Physical Review B*, 84(19):195310, November 2011. doi: 10.1103/PhysRevB.84.195310. URL <https://link.aps.org/doi/10.1103/PhysRevB.84.195310>. 6.3.4
- [52] Corneliu Malciu, Leonardo Mazza, and Christophe Mora. Braiding Majorana zero modes using quantum dots. *Physical Review B*, 98(16):165426, October 2018. doi: 10.1103/

PhysRevB.98.165426. URL <https://link.aps.org/doi/10.1103/PhysRevB.98.165426>. 6.3.4, 6.14

- [53] Zhaoen Su, Alexandre B. Tacla, Moira Hocevar, Diana Car, Sébastien R. Plissard, Erik P. A. M. Bakkers, Andrew J. Daley, David Pekker, and Sergey M. Frolov. Andreev molecules in semiconductor nanowire double quantum dots. *Nature Communications*, 8(1):585, September 2017. ISSN 2041-1723. doi: 10.1038/s41467-017-00665-7. URL <https://www.nature.com/articles/s41467-017-00665-7>. 6.3.4, 7
- [54] T. I. Ivanov. Coherent tunneling through a double quantum dot coupled to Majorana bound states. *Physical Review B*, 96(3):035417, July 2017. doi: 10.1103/PhysRevB.96.035417. URL <https://link.aps.org/doi/10.1103/PhysRevB.96.035417>. 7
- [55] Alexander Schuray, Luzie Weithofer, and Patrik Recher. Fano resonances in Majorana bound states–quantum dot hybrid systems. *Physical Review B*, 96(8):085417, August 2017. doi: 10.1103/PhysRevB.96.085417. URL <https://link.aps.org/doi/10.1103/PhysRevB.96.085417>. 7.2.2

Appendix A

Appendix

A.1 From the logarithmic discretization to the Wilson's chain.

Logarithmic Discretization:

We start with an Anderson model Hamiltonian such as the one in (Equation 4.5) without magnetic field

$$H = \frac{U}{2} + \sum_{\sigma} \left[\left(\varepsilon_d + \frac{U}{2} \right) d_{\sigma}^{\dagger} d_{\sigma} + \frac{U}{2} (d_{\sigma}^{\dagger} d_{\sigma} - 1)^2 + \sum_{\mathbf{k}} \varepsilon_{\mathbf{k}} c_{\mathbf{k}\sigma}^{\dagger} c_{\mathbf{k}\sigma} + V_{\mathbf{k}} d_{\sigma}^{\dagger} c_{\mathbf{k}\sigma} + V_{\mathbf{k}}^* c_{\mathbf{k}\sigma}^{\dagger} d_{\sigma} \right]. \quad (\text{A.1})$$

At low-energies we can assume that QD couples only to s-wave states in the leads[34]. This implies that the Fermi surface is contained in a single, isotropic conduction band extending inside some fixed cutoffs $-D$ and D . Thus, $\varepsilon_{\mathbf{k}}$ only depends on $|\mathbf{k}|$. This makes possible to transform the sum over \mathbf{k} in equation Equation A.1 into an integral over ε between the energy cutoffs

$$\begin{aligned} H = \sum_{\sigma} & \left[\left(\varepsilon_d + \frac{U}{2} \right) d_{\sigma}^{\dagger} d_{\sigma} + \frac{U}{2} (d_{\sigma}^{\dagger} d_{\sigma} - 1)^2 + \int_{-D}^D d\varepsilon \varepsilon c_{\varepsilon\sigma}^{\dagger} c_{\varepsilon\sigma} \right. \\ & \left. + \int_{-D}^D \sqrt{\rho_{\sigma}(\varepsilon)} d\varepsilon V_{\varepsilon} d_{\sigma}^{\dagger} c_{\varepsilon\sigma} + V_{\varepsilon}^* c_{\varepsilon\sigma}^{\dagger} d_{\sigma} \right]. \end{aligned} \quad (\text{A.2})$$

Here $c_{\varepsilon\sigma}^{\dagger}$ creates an electron with energy ε and $\rho_{\sigma}(\varepsilon)$ is the density of states of the system per spin, which appears in the integral due to the change of variable from \mathbf{k} to $\varepsilon \propto |\mathbf{k}|^2$. Finally, we ignore the energy dependence of ρ and V_d and we replace them by their values in the Fermi energy (This approximation has no great relevance which is justified in [34]) and we renormalize the energy band doing the replacements $k = \frac{\varepsilon}{D}$ and $c_{k\sigma} := \sqrt{D}c_{\varepsilon\sigma}$ so that (Equation A.2) becomes

$$H = D \sum_{\sigma} \left[\frac{1}{D} \left(\varepsilon_d + \frac{U}{2} \right) d_{\sigma}^{\dagger} d_{\sigma} + \frac{U}{2D} (d_{\sigma}^{\dagger} d_{\sigma} - 1)^2 + \int_{-1}^1 dk k c_{k\sigma}^{\dagger} c_{k\sigma} \right. \\ \left. + \sqrt{\frac{\Gamma}{\pi D}} \int_{-1}^1 dk d_{\sigma}^{\dagger} c_{k\sigma} + c_{k\sigma}^{\dagger} d_{\sigma} \right] \quad (\text{A.3})$$

$$= H_d + D \sum_{\sigma} \left[\int_{-1}^1 dk k c_{k\sigma}^{\dagger} c_{k\sigma} + \sqrt{\frac{\Gamma}{\pi D}} \int_{-1}^1 dk d_{\sigma}^{\dagger} c_{k\sigma} + c_{k\sigma}^{\dagger} d_{\sigma} \right], \quad (\text{A.4})$$

where $\Gamma = \pi \rho V^2$ is associated to the lever-width [27, (3.5)]. At this point we have our model dependent of three unit-less constants $\frac{\varepsilon_d}{D}$, $\frac{U}{2D}$ and $\frac{\Gamma}{\pi D}$. The logarithmic discretization starts by defining an scaling parameter $\Lambda \geq 1$ in diving the energy domain $[-1, 1]$ into an array of intervals of the form $\{[\pm \Lambda^{-(n+1)}, \pm \Lambda^n]\}_{n \in \mathbb{N}}$, as we can observe in ???. Note that the width of these intervals is decreasing exponentially by

$$d_n = \Lambda^{-n} (1 - \Lambda^{-1}).$$

Then inside of these energy intervals we can define a set of orthonormal Fourier series of the form

$$\phi_{np}^{\pm}(\varepsilon) = \begin{cases} \frac{1}{\sqrt{d_n}} e^{\pm i \omega_n p \varepsilon} & \varepsilon \in [\pm \Lambda^{-(n+1)}, \pm \Lambda^n] \\ 0 & \text{a.o.c.} \end{cases} \quad (\text{A.5})$$

with $\omega_n := \frac{2\pi}{d_n}$ so that $\phi_{np}^{\pm}(\pm \Lambda^{-(n+1)}) = \phi_{np}^{\pm}(\pm \Lambda^{-n})$. Then we can decompose the creation operators c_k^{\dagger} into their interval-Fourier contributions as

$$c_k^{\dagger} = \sum_{np} \phi_{np}^{+}(k) c_{np\sigma}^{+\dagger} + \phi_{np}^{-}(k) c_{np\sigma}^{-\dagger} \quad (\text{A.6})$$

with the new creation operators defined as

$$c_{np\sigma}^{\pm\dagger} := (c_{np\sigma}^{\pm})^{\dagger} = \int_{-1}^1 d\varepsilon [\phi_{np}^{+}(\varepsilon)]^* c_{\varepsilon\sigma}^{\dagger}.$$

This decomposition (Equation A.6) is a simple consequence of the orthonormality of the functions defined in (Equation A.5). In addition we can readily proof that $c_{np\sigma}^{\pm\dagger}$ -operators satisfy the anti-commutation relations, so that they are rightful fermionic creation operators.

We can now use (Equation A.6) to replace the k -dependent terms in hamiltonian (Equation A.3). Then we obtain

$$\begin{aligned}
\int_{-1}^1 dk c_{k\sigma}^\dagger d_\sigma &= \int_{-1}^1 dk \left(\sum_{np} \phi_{np}^+(k) c_{np\sigma}^{+\dagger} + \phi_{np}^-(k) c_{np\sigma}^{-\dagger} \right) d_\sigma \\
&= \left(\sum_{np} \left(\int_{-1}^1 dk \phi_{np}^+(k) \right) c_{np\sigma}^{+\dagger} + \left(\int_{-1}^1 dk \phi_{np}^-(k) \right) c_{np\sigma}^{-\dagger} \right) d_\sigma \\
&= \left(\sum_{np} \left(\int_{\Lambda^{-(n+1)}}^{\Lambda^{-n}} dk \frac{e^{i\omega_n p k}}{\sqrt{d_n}} \right) c_{np\sigma}^{+\dagger} + \left(\int_{-\Lambda^{-n}}^{-\Lambda^{-(n+1)}} dk \frac{e^{-i\omega_n p k}}{\sqrt{d_n}} \right) c_{np\sigma}^{-\dagger} \right) d_\sigma \\
&= \left(\sum_{np} \sqrt{d_n} \delta_p c_{np\sigma}^{+\dagger} + \sqrt{d_n} \delta_p c_{np\sigma}^{-\dagger} \right) d_\sigma \\
&= \sqrt{1 - \Lambda^{-1}} \sum_n \Lambda^{-\frac{n}{2}} (c_{np\sigma}^{+\dagger} + c_{np\sigma}^{-\dagger}) d_\sigma. \tag{A.7}
\end{aligned}$$

And

$$\begin{aligned}
\int_{-1}^1 dk k c_{k\sigma}^\dagger c_{k\sigma} &= \sum_{n,n',p,p'} \sum_{s,s'=\pm} \left(\int_{-1}^1 k dk \phi_{np}^s(k) (\phi_{np}^{s'}(k))^* \right) c_{np\sigma}^{s\dagger} c_{n'p'\sigma}^{s'} \\
&= \sum_{n,n',p,p'} \sum_{s,s'=\pm} \left(\frac{\delta_{nn'} \delta_{ss'}}{d_n} \int_{\Lambda^{-(n+1)}}^{\Lambda^{-n}} k dk e^{is\omega_n k(p-p')} \right) c_{np\sigma}^{s\dagger} c_{n'p'\sigma}^s \\
&= \sum_{npp'} \sum_{s=\pm} \left(\frac{s}{2} \Lambda^{-2n} (1 - \Lambda^{-2}) \delta_{pp'} + \frac{1 - \delta_{pp'}}{is\omega_n(p-p')} [ke^{is\omega_n k(p-p')}]_{\Lambda^{-(n+1)}}^{\Lambda^{-n}} \right) \frac{c_{np\sigma}^{s\dagger} c_{n'p'\sigma}^{s'}}{d_n} \\
&= \frac{1}{2} (1 + \Lambda^{-1}) \sum_{np} \Lambda^{-n} (c_{np\sigma}^{+\dagger} c_{np\sigma}^+ - c_{np\sigma}^{-\dagger} c_{np\sigma}^-) \\
&\quad + \sum_n \sum_{p \neq p'} \frac{1 - \Lambda^{-1}}{2i\pi(p' - p)} (c_{np\sigma}^{+\dagger} c_{np'\sigma}^+ - c_{np'\sigma}^{-\dagger} c_{np\sigma}^-) e^{\frac{2i\pi(p-p')}{1-\Lambda^{-1}}}. \tag{A.8}
\end{aligned}$$

Thus, if we replace (Equation A.7) and (Equation A.8) into (Equation A.3) we will obtain a logarithmic discretization of the hamiltonian. The next part will we to map this discretization to an iterative process that is worth for a numerical computations.

Mapping the Anderson model to a Chain-Hamiltonian

We are looking for a model just like the one we have in the right part of Figure 5.3. This is because a Chain-Hamiltonian will give an iterative approximation of the Anderson model with an increasing (but still controllable) number of degrees of freedom. This will provide the rightful structure for a numerical diagonalization of the hamiltonian.

A.1. From the logarithmic discretization to the Wilson's chain.

To do this, observe from equations (Equation A.7),(Equation A.8) that the QD (d_σ) couples directly only to the operators with $p = 0$ ($c_{n0\sigma}^{\pm\dagger}$). The $p \neq 0$ terms will appear in the hamiltonian only because they are coupled to $c_{np\sigma}^{+\dagger}$ in Equation (Equation A.8). Thus, as a first approximation we can neglect all terms in (Equation A.8) with $p \neq 0$. This leaves only the first part of (Equation A.8), so that we can define $c_{n\sigma}^{\pm\dagger} := c_{np\sigma}^{\pm\dagger}$. Let

$$f_{0\sigma}^\dagger = \sqrt{\frac{1-\Lambda^{-1}}{2}} \sum_n \Lambda^{-\frac{n}{2}} (c_{n\sigma}^{+\dagger} + c_{n\sigma}^{-\dagger}), \text{ so that } \sqrt{2} f_{0\sigma}^\dagger d_\sigma = \int_{-1}^1 dk c_{k\sigma}^\dagger d_\sigma. \quad (\text{A.9})$$

Note $\{f_{0\sigma}^\dagger, f_{0\sigma}\} = \frac{1-\Lambda^{-1}}{2} \sum_n 2\Lambda^{-n} = 1$. Replacing this in (Equation A.3)we get

$$H = H_d + D \sum_\sigma \left[\sqrt{\frac{2\Gamma}{\pi D}} (d_\sigma^\dagger f_{0\sigma} + f_{0\sigma}^\dagger d_\sigma) + \frac{1}{2} (1 + \Lambda^{-1}) \sum_n \Lambda^{-n} (c_{n\sigma}^{+\dagger} c_{n\sigma}^+ - c_{n\sigma}^{-\dagger} c_{n\sigma}^-) \right].$$

f_0^\dagger will represent the first site of the chain-hamiltonian in ?? since no other term is coupled to the dot hamiltonian. We also have the coupling term $\xi_0 = \sqrt{\frac{2\Gamma}{\pi D}}$. It is possible to obtain the following f_m^\dagger -operators by supposing a solution of the form

$$f_{m\sigma}^\dagger = \sum_n a_{mn}^+ c_{n\sigma}^{+\dagger} + a_{mn}^- c_{n\sigma}^{-\dagger} = \sum_n \sum_{s=\pm} a_{mn}^s c_{n\sigma}^{s\dagger}, \quad (\text{A.10})$$

such that they satisfy the anti-commutation relations

$$\{f_{m\sigma}^\dagger, f_{m'\sigma'}\} = \delta_{mm'} \delta_{\sigma\sigma'}, \quad \{f_{m\sigma}^\dagger, f_{m\sigma}^\dagger\} = \{f_{m\sigma}^\dagger, f_{m\sigma}^\dagger\} = 0$$

and

$$\frac{1}{2} (1 + \Lambda^{-1}) \sum_n \Lambda^{-n} (c_{n\sigma}^{+\dagger} c_{n\sigma}^+ - c_{n\sigma}^{-\dagger} c_{n\sigma}^-) = \sum_{m=0}^{\infty} \Lambda^{-\frac{m}{2}} \xi_m (f_{m\sigma}^\dagger f_{m+1,\sigma} + f_{m+1,\sigma}^\dagger f_{m\sigma}). \quad (\text{A.11})$$

It is possible to find a solution for this system using the formula of the right part of equation Equation A.11. Since the relation is only given between consecutive terms $m, m+1$ and we already have the coefficients for $m = 0$ ($a_{0n}^s = \sqrt{\frac{1-\Lambda^{-1}}{2}} \Lambda^{-\frac{n}{2}}$). Then it is possible to determine the upper coefficients in a recursive way starting from $m = 0$. Supposing we can obtain the m^{th} -coefficients (a_{mn}^s) and then finding iteratively the coefficients of $m+1$ ($a_{m+1,n}^s$) using the relation given by equation (Equation A.11). This provides a numerical way for obtaining the $f_{m\sigma}^\dagger$ operators. In fact in our case, where we actually did important assumptions, the problem can be solved analytically obtaining that the final Hamiltonian is given by

$$H = H_d + D \sum_\sigma \left[\sqrt{\frac{2\Gamma}{\pi D}} (d_\sigma^\dagger f_{0\sigma} + f_{0\sigma}^\dagger d_\sigma) + \frac{1}{2} (1 + \Lambda^{-1}) \sum_{n=0}^{\infty} \Lambda^{-\frac{n}{2}} \xi_n (f_{n\sigma}^\dagger f_{n+1,\sigma} + f_{n+1,\sigma}^\dagger f_{n\sigma}) \right]. \quad (\text{A.12})$$

A.1. From the logarithmic discretization to the Wilson's chain.

with

$$\xi_n = \frac{1 - \Lambda^{-n-1}}{(1 - \Lambda^{-2n-1})^{\frac{1}{2}} (1 - \Lambda^{-2n-3})^{\frac{1}{2}}}.$$

The formal recursive-solution of this problem can be found in [33]. Note that equation (Equation A.12) describes the chain hamiltonian model that we where looking for in ???. Note that in the limit when $n \rightarrow \infty$

$$\Lambda^{\frac{-n}{2}} \xi_n \rightarrow \frac{\Lambda^{\frac{-n}{2}} (1 - \Lambda^{-n})}{1 - \Lambda^{-2n}} \sim \frac{\Lambda^{\frac{-n}{2}}}{1 + \Lambda^{-n}},$$

which implies an exponential decaying of the hopping term in the chain.

Appendix B

Three peak appearance in the Double Quantum Dot model.

The DQD model is characterized by the formation of a new state that entangles the two Quantum dots through the leads. This produces an anti-ferromagnetic interaction between the QDs, commonly known as Ruderman-Kittel-Kasuya-Yosida (RKKY) interaction [19, 21]. As consequence, two satellite peaks will emerge in the Density of States.

To explain this phenomenon we will take a symmetric version of Hamiltonian (Equation 7.1) with $2e_i = U_i = U$, $t_i = t$ and $t_{dots} = 0$ for $i \in \{1, 2\}$.

$$H = \sum_{i,k,\sigma} \frac{U_i}{2} (d_{i\sigma}^\dagger d_{i\sigma} - 1)^2 + t(d_{+, \downarrow} + d_{+, \uparrow}^\dagger) \gamma_1 + \Gamma_i (d_{i\sigma}^\dagger c_{k\sigma} + c_{k\sigma}^\dagger d_{i\sigma}). \quad (\text{B.1})$$

The symmetry of the previous Hamiltonian is suitable to apply a base change of the form

$$d_{+,\sigma} = \frac{1}{\sqrt{2}}(d_{1\sigma} + d_{2\sigma}), \quad d_{-,\sigma} = \frac{1}{\sqrt{2}}(d_{1\sigma} - d_{2\sigma}).$$

These new operators satisfy the fermionic anti-commutation relations

$$\{d_{\pm,\sigma}, d_{\pm,\sigma}^\dagger\} = 1, \{d_{\pm,\sigma}, d_{\mp,\sigma}^\dagger\} = 0,$$

so that they may be considered as fermion operators. All lineal terms in (Equation B.1) are trivially adapted to the new base. The repulsion potential

$$\sum_i \left(\sum_\sigma d_{i\sigma}^\dagger d_{i\sigma} - 1 \right)^2 = \left(\sum_\sigma d_{1\sigma}^\dagger d_{1\sigma} - 1 \right)^2 + \left(\sum_\sigma d_{2\sigma}^\dagger d_{2\sigma} - 1 \right)^2.$$

gives rise to a non-trivial interaction between the new states. To find this interaction we define the particle number operator

$$\hat{n}_{i,\sigma} := d_{i,\sigma}^\dagger d_{i,\sigma}.$$

So that

$$\hat{n}_{1,\sigma} = \frac{1}{2} \left(\hat{n}_{+,\sigma} + \hat{n}_{-,\sigma} + d_{+,\sigma}^\dagger d_{-,\sigma} + d_{-,\sigma}^\dagger d_{+,\sigma} \right) = \frac{1}{2} (\hat{N}_\sigma + \hat{E}_\sigma),$$

with $\hat{N} = \hat{n}_{+,\sigma} + \hat{n}_{-,\sigma}$ and $\hat{E}_\sigma = d_{+,\sigma}^\dagger d_{-,\sigma} + d_{-,\sigma}^\dagger d_{+,\sigma}$. Similarly

$$\hat{n}_{2,\sigma} = \frac{1}{2} (\hat{N}_\sigma - \hat{E}_\sigma).$$

Hence

$$\sum_i (\sum_\sigma d_{i\sigma}^\dagger d_{i\sigma} - 1)^2 = \left(\frac{\hat{N} + \hat{E}}{2} - 1 \right)^2 + \left(\frac{\hat{N} - \hat{E}}{2} - 1 \right)^2 = \frac{(\hat{N} - 2)^2 - \hat{E}^2}{2},$$

with $\hat{N} = \sum_\sigma \hat{N}_\sigma$, $\hat{E} = \sum_\sigma \hat{E}_\sigma$. Note that opeator \hat{N} represents the total occupation number inside both dots. If this occupation is different than 2 there is an imbalance between particles and dots that is punished by this term. The term E^2 is much more interesting since this one is the responsible for the emergence of satellite peaks in the DOS. To understand what it makes it is simple to observe its results when applied to a based ordered by $|+, -\rangle$.

$$\hat{E}^2 |\uparrow, 0\rangle = \hat{E} |0, \uparrow\rangle = |\uparrow, 0\rangle$$

$$\hat{E}^2 |\uparrow, \downarrow\rangle = \hat{E} (|0, \uparrow\downarrow\rangle + |\uparrow\downarrow, 0\rangle) = 2|\uparrow, \downarrow\rangle - 2|\downarrow, \uparrow\rangle$$

The new Hamiltonian

$$H = \sum_\sigma \frac{U}{4} \left((\hat{N} - 2)^2 - \hat{E}^2 \right) + \frac{t}{\sqrt{2}} (d_{+, \downarrow} + d_{+, \downarrow}^\dagger) \gamma_1 + \frac{\Gamma}{\sqrt{2}} \sum_k (d_{+, \sigma}^\dagger c_{k\sigma} + c_{k\sigma}^\dagger d_{+, \sigma}) \quad (\text{B.2})$$

is represented in ??

We can explain this three-peak as the result of a new strong coupling interaction characterized by the spin exchange between both dots.

In addition, the spin-up DOS at the Fermi energy grows faster than the spin-down DOS, breaking the initial spin-symmetry when $t_1 = t_2 = 0$. At $t_1 = t_2 = 0.02D$ the spin-up DOS at the fermi energy doubles the spin-down DOS which implies that the Majorana signature is present in both dots. Indeed ?? shows that the relation $\frac{\rho_{\uparrow}(0)}{\rho_{\uparrow}(0)}$ increases continuously from 1 to 2. Note that the Majorana is completely attached when the coupling t_1 reaches the order of $0.01D$.

B.1 Initial DQD-Majorana Hamiltonian.

$H_{N_\uparrow=0, P_\downarrow=-1}$:

$$\begin{aligned} |\downarrow, \downarrow, \downarrow\rangle &\rightarrow \left[\begin{array}{cccc} \varepsilon_d^+ + \frac{U^+}{2} - 2h + \varepsilon_m & 0 & -\tilde{t}_{+1} & \tilde{t}_{+2} \\ 0 & \frac{U^+}{2} + \varepsilon_m & \tilde{t}_{-2}^* & \tilde{t}_{-1}^* \\ 0, \downarrow, 0\rangle & \rightarrow \left[\begin{array}{cccc} -\tilde{t}_{+1}^* & \tilde{t}_{-2} & \varepsilon_{d_2} + \frac{U^+}{2} - h - \varepsilon_m & t \\ \tilde{t}_{+2}^* & \tilde{t}_{-1} & t^* & \varepsilon_{d_1} + \frac{U^+}{2} - h - \varepsilon_m \end{array} \right] \\ |\downarrow, 0, 0\rangle &\rightarrow \end{array} \right] \end{aligned}$$

B.1. Initial DQD-Majorana Hamiltonian.

$$H_{N_\uparrow=0, P_\downarrow=1} :$$

$$\begin{aligned} |0,0,0\rangle &\rightarrow \left[\begin{array}{ccccc} \frac{U^+}{2} - \varepsilon_m & 0 & \tilde{t}_{+1} & \tilde{t}_{+2} \\ 0 & \varepsilon_d^+ + \frac{U^+}{2} - 2h - \varepsilon_m & \tilde{t}_{-2}^* & -\tilde{t}_{-1}^* \\ \tilde{t}_{+1}^* & \tilde{t}_{-2} & \varepsilon_{d_1} + \frac{U^+}{2} - h + \varepsilon_m & t \\ \tilde{t}_{+2}^* & -\tilde{t}_{-1} & t^* & \varepsilon_{d_2} + \frac{U^+}{2} - h + \varepsilon_m \end{array} \right] \\ |\downarrow,\downarrow,0\rangle &\rightarrow \\ |\downarrow,0,\downarrow\rangle &\rightarrow \\ |0,\downarrow,\downarrow\rangle &\rightarrow \end{aligned}$$

$H_{N_\uparrow=2, P_\downarrow=-1} :$

$$|\uparrow\downarrow, \uparrow\downarrow, \downarrow\rangle \rightarrow \begin{bmatrix} 2\varepsilon_d^+ + \frac{3U^+}{2} + \varepsilon_m & 0 & \tilde{t}_{+1} & \tilde{t}_{+2} \\ 0 & \varepsilon_d^+ + \frac{U^+}{2} + 2h + \varepsilon_m & \tilde{t}_{-2}^* & -\tilde{t}_{-1}^* \\ \tilde{t}_{+1}^* & \tilde{t}_{-2} & f(d_1, d_2) + h - \varepsilon_m & -t \\ \tilde{t}_{+2}^* & -\tilde{t}_{-1} & -t^* & f(d_2, d_1) + h - \varepsilon_m \end{bmatrix}$$

with $f(d_i, d_j) = \varepsilon_{d_i} + \frac{U_i}{2} + 2\varepsilon_{d_j} + \frac{3U_j}{2}$.

$$H_{N_\uparrow=2, P_\downarrow=1} :$$

$$|\uparrow, \uparrow, 0\rangle \rightarrow \begin{bmatrix} \varepsilon_d^+ + \frac{U^+}{2} + 2h - \varepsilon_m & 0 & -\tilde{t}_{+1} & \tilde{t}_{+2} \\ 0 & 2\varepsilon_d^+ + \frac{3U^+}{2} - \varepsilon_m & \tilde{t}_{-2}^* & \tilde{t}_{-1}^* \\ -\tilde{t}_{+1}^* & \tilde{t}_{-2} & f(d_2, d_1) + h + \varepsilon_m & -t \\ \tilde{t}_{+2}^* & \tilde{t}_{-1} & -t^* & f(d_1, d_2) + h + \varepsilon_m \end{bmatrix}$$